JOURNAL OF PETROLOGY | VOLUME 0 | NUMBER 0 | PAGES 1–40 | 2013 | doi:10.1093/petrology/egt050
Journal of Petrology Advance Access published September 24, 2013

Melt– and Fluid–Rock Interaction in Supra-Subduction Lithospheric Mantle: Evidence from Andesite-hosted Veined Peridotite Xenoliths

ANTOINE BÉNARD*† AND DMITRI A. IONOV‡

UNIVERSITÉ J. MONNET (MEMBER OF PRES-UNIVERSITÉ DE LYON), 42023 SAINT-ÉTIENNE & UMR6524-CNRS, FRANCE

RECEIVED APRIL 5, 2011; ACCEPTED AUGUST 19, 2013

We report petrographic, major and trace element data for xenoliths from the andesitic Avacha volcano (Kamchatka), which host orthopyroxene (opx)-rich veins of mantle origin formed either by rapid crystallization of intruded melts or by their interaction with the host harzburgite. Studies of such veins may give better insights into sub-arc mantle processes (in particular on a millimetre to centimetre scale) than those of (1) arc xenoliths that do not preserve solidified initial metasomatizing agents, (2) massif peridotites, probably modified during their emplacement, or (3) arc magmatic rocks, which provide indirect information. We seek to trace the evolution of these agents as they react with the host peridotite and to assess their impact on the wall-rocks. The veins cross-cut spinel harzburgite and consist mainly of opx with minor olivine, clinopyroxene (cpx) and/or amphibole. We identify 'rapidly crystallized' veins that cut wall-rock olivine without petrographic evidence of reaction, and 'reactive' veins subdivided into 'thick' (0·5–1 mm) and 'thin' (<0·5 mm). Minerals in the rapidly crystallized veins are depleted in rare earth elements (REE) and high field strength elements (HFSE) and enriched in fluid-mobile elements relative to REE. Minerals in the reactive veins have higher Ti, Al, Cr and alkalis than minerals in the rapidly crystallized veins, as well as highly variable trace element abundances, especially in reaction zones, thin veins and related metasomatic pockets in the host peridotite. They commonly show U-shaped REE patterns and positive Zr and Hf spikes in normalized trace element patterns. Our data, supported by recent reports, show that the rapidly crystallized veins formed between 1200°C and 900°C from a liquid derived by fluid-fluxed melting of a refractory (harzburgitic) mantle source depleted in heavy REE. The reactive veins formed via 'fractionation–reactive percolation' from fractionated hydrous derivatives of the melts that precipitated the rapidly crystallized veins. These liquids re-equilibrated with the host through diffusion and fluid-assisted dissolution–precipitation reactions, whose end-products are thin reactive veins and metasomatic pockets with distinctive U-shaped REE patterns and Zr–Hf spikes. Some Avacha xenoliths contain veins of Fe-rich amphibole deposited from the host magma that penetrated fractures in the peridotite fragments during their transport to the surface. These products of contamination were mistakenly attributed to mantle metasomatism in previous studies of other suites of Avacha mantle xenoliths. Trace element abundances in such veins are higher than for reactive veins of mantle origin, but both have similar trace element patterns (U-shaped REE patterns and Zr–Hf spikes) suggesting that 'fractionation–reactive percolation' also took place during their formation and is common during interaction of refractory peridotites with percolating melts and fluids. Metasomatic pockets of cpx and amphibole replacing coarse opx and spinel in the host peridotites commonly occur in the vicinity of fractures that lead to reactive opx-rich veins. The cpx and amphiboles in the pockets show progressive depletion in middle REE and HFSE at constant light REE and/or large ion lithophile elements away from the veins towards the host. This indicates that residual hydrous fluids expelled from the source veins enriched the wall-rock peridotites in incompatible elements but were progressively modified by reaction with the host with increasing percolation distance. This process produces disseminated pockets of metasomatic minerals with a broad range of compositions from a single initial liquid and strongly affects the trace element budgets of the harzburgite xenoliths from Avacha. We show that melts and fluids are likely to undergo profound transformation as they travel through and react with the refractory host mantle, even on a millimetre to centimetre scale. The composition of the initial metasomatizing agents can only be inferred from the composition of the metasomatic phases in mantle rocks combined with appropriate partition coefficients if

*Corresponding author. Telephone: +61 (0) 261251476.
E-mail: antoine.benard@anu.edu.au
†Present address: Research School of Earth Sciences, The Australian National University, Canberra, ACT 0200, Australia.
‡Present address: Géosciences Montpellier, Université Montpellier 2, 34095 Montpellier, France.

these phases come from well-equilibrated mineral assemblages located close to melt and/or fluid sources.

KEY WORDS: *melt–rock interaction; fluid–rock interaction; subduction zone; mantle xenolith; vein; Avacha*

INTRODUCTION

Large amounts of melts are produced in subduction zones as fluids expelled from the dehydrating slab trigger partial melting in the mantle wedge. An essential task of geochemical studies in subduction zones is to elucidate the compositions of the slab-derived components and of primary mantle wedge melts. These are commonly inferred from studies of arc-related rocks (e.g. Nakamura *et al.*, 1985; Defant & Drummond, 1990; Ishikawa & Nakamura, 1994) and melt inclusions (e.g. Schiano *et al.*, 2001). The initial compositions of both slab-derived components and primary arc melts, however, remain elusive because arc magmas are affected by fractional crystallization or contamination during ascent in the crust, as well as by melt–rock interaction in the mantle wedge above the melting zone (Kelemen *et al.*, 1990, 1993). The latter process may also profoundly affect the composition of the lithospheric mantle (Hawkesworth *et al.*, 1993). Thus, knowledge of the interaction processes of migrating melts and fluids with their host mantle may provide better insights into the origin and evolution of arc lithosphere and magmatism. This can be addressed by studies of direct samples of sub-arc mantle (i.e. xenoliths in volcanic rocks from active arcs) to (1) determine the composition of the initial melts or fluids that percolated through them and (2) explore the interaction of these melts or fluids with the host peridotite.

A relatively large amount of data has been reported on mantle rocks from presumed ancient arcs (Varfalvy *et al.*, 1996; Bédard, 1999; Santos *et al.*, 2002; Berly *et al.*, 2006; Bali *et al.*, 2007; Dhuime *et al.*, 2007; Garrido *et al.*, 2007; Ackerman *et al.*, 2008), as well as xenoliths from modern back-arc (Franz *et al.*, 2002; Arai *et al.*, 2006) and fore-arc (Parkinson & Pearce, 1998) settings. These samples, however, may have been affected by processes independent of the arc setting such as metamorphism, non-arc magmatism and alteration. Arc-related signatures in xenoliths from continental margins (e.g. Lee *et al.*, 2001; Peslier *et al.*, 2002; Mukasa *et al.*, 2007; Wang *et al.*, 2008; Chin *et al.*, 2012) may be hard to differentiate from those produced in intra-continental settings. Overall, mantle xenoliths from oceanic arcs are thought to give the most reliable insights into sub-arc processes, but these samples are rare.

The majority of mantle xenoliths from modern arcs reported in the literature are from the northern and western Pacific (e.g. Takahashi, 1980, 1986; Vidal *et al.*, 1989; Maury *et al.*, 1992; Kepezhinskas *et al.*, 1995; Arai *et al.*, 2004). These samples commonly show evidence for reaction with the host magma (e.g. Parkinson *et al.*, 2003; Ionov *et al.*, 2013), contamination by arc crust material (e.g. Fourcade *et al.*, 1994), recrystallization (Arai *et al.*, 2004; Bryant *et al.*, 2007) and surface alteration, which affect the signatures of earlier processes. Because of these overprinting processes, such samples may not be ideal to explore melt–rock interaction in the mantle.

Models of melt–rock reaction in the mantle are difficult to constrain because, in most cases, the initial compositions of the percolating melt and the wall-rock matrix are unknown (Nielson & Wilshire, 1993). Pyroxenitic veins in peridotite xenoliths may be very useful in constraining the compositions of migrating melts and fluids and their evolution in the mantle. Specifically, pyroxene-rich veins in sub-arc xenoliths have been interpreted as resulting from the crystallization of Mg- and Si-rich primary magmas (Halama *et al.*, 2009), slab melts (Kepezhinskas *et al.*, 1996; Ishimaru *et al.*, 2007; Ishimaru & Arai, 2008) or from interaction of mantle rocks with water-rich fluids (Grégoire *et al.*, 2001; McInnes *et al.*, 2001).

Veined sub-arc mantle xenoliths have previously been reported from the Kamchatka peninsula, Russia (e.g. Kepezhinskas *et al.*, 1995; Kepezhinskas & Defant, 1996; Bryant *et al.*, 2007), but most of these samples come from the currently inactive subduction of the Komandorsky plate in northern Kamchatka. Recently published data on xenoliths from the active andesitic Avacha volcano in southern Kamchatka suggest that veining may play an important role in the evolution of arc mantle lithosphere. Halama *et al.* (2009) reported coarse-grained websteritic veins re-equilibrated with host peridotites, whereas Ishimaru *et al.* (2007) and Ishimaru & Arai (2008) studied metasomatized peridotites containing fine-grained orthopyroxene-rich materials.

More recently Ionov (2010) characterized the petrology and geochemistry of the lithospheric mantle beneath Avacha based on a suite of large, fresh and mainly coarse-grained harzburgite xenoliths. Further work on the same suite explored microstructures, crystal preferred orientations and water contents in the peridotites (Soustelle *et al.*, 2010), studied the micro-textures of their sulfide inclusions (Bénard *et al.*, 2011*b*), defined their noble gas compositions and showed that they contained slab-derived components (Hopp & Ionov, 2011), described glass-bearing inclusions in spinel, which provide a record of melting and metasomatism in the mantle and reaction with the host magma (Ionov *et al.*, 2011), and reported metasomatic products produced by low-Ca boninitic melts (Bénard & Ionov, 2012).

This study presents detailed petrographic, and major and trace element data for 11 veined peridotite xenoliths from Avacha collected together with those described by Ionov (2010). In particular, these xenoliths contain two

major types of veins formed by the crystallization of fluid-rich and silicic melts, which intruded and reacted with the peridotites. Using this new dataset, our major objectives are to (1) establish the initial compositions and origins of the melts that formed the veins, (2) document the evolution of the melt during its percolation in the host harzburgitic mantle on a millimetre to centimetre scale, based on comparisons of the two major vein types, (3) explore the impact of veining and melt–rock interaction on the composition of refractory mantle peridotite xenoliths and (4) discuss the results of previous studies of the Avacha mantle xenoliths. Overall, we identify processes that profoundly transform the initial signatures of both percolating melts and fluids and the host peridotite in the shallow mantle lithosphere above subduction zones.

GEOLOGICAL SETTING AND SAMPLES

The Kamchatka peninsula has three sub-parallel volcanic chains located respectively at 200, 320 and 400 km NE of the Kuril–Kamchatka trench (Fig. 1) (Tatsumi *et al.*, 1994). In the southern part of the Kamchatka arc, the Pacific plate (~80 Ma) is subducting almost orthogonally at a rate of 7–9 cm a^{-1} and dipping at 55°.

The Avacha strato-volcano (53°15'N, 158°51'E; summit elevation 2741 m) is located near the east coast of the southern Kamchatka peninsula, in the centre of the Eastern Volcanic Belt (EVB, Fig. 1). Avacha is one of Kamchatka's most active volcanoes; it formed in late Pleistocene times and most recently erupted in 1991 and 2001. Its Holocene eruptions produced ash-falls and pyroclastic flows with reported compositions ranging from picritic to dacitic, mainly from low-K andesite (7250–3500 ^{14}C years BP) to basaltic andesite (Braitseva *et al.*, 1998). Seismic data indicate a crustal thickness of ~37 km (Levin *et al.*, 2002) and show low P-wave velocity domains beneath the Moho consistent with the presence of melt (Gorbatov *et al.*, 1999). The depth to the slab's upper surface is ~120 km and the slab thickness is ~70 km (Gorbatov *et al.*, 1997, 1999; Jiang *et al.*, 2009).

The xenoliths from this study [seven veined samples 10–15 cm in size (Av18, Av19, Av27, Av49, Av52, Av53 and Av54)] were collected from volcanic ash and scoria together with those reported by Ionov (2010). We also report new data on veined samples Av9 and Av12 from Ionov (2010) and Av20 and Av21 from Bénard & Ionov (2012). All the samples contain orthopyroxene (opx)-rich and amphibole (amph)-opx veins (Fig. 2).

ANALYTICAL METHODS

Major elements in minerals were determined in polished thin sections by wavelength-dispersive (WD) electron probe micro-analysis (EPMA) on CAMECA SX100 instruments at 'Service Microsonde Sud', Université Montpellier II and at the Laboratoire Magmas et Volcans (Clermont-Ferrand). Analyses in Montpellier were performed at an accelerating voltage of 15 kV and a sample current of 10 nA. Counting times were 15–20 s on background and 30 s (Cr and Ni) and 20 s for all other elements on peaks. The computer correction program of Merlet (1994) was applied for data reduction. Analyses in Clermont-Ferrand were performed at 20 kV and 15 nA. Glass analyses were carried out with a defocused beam (5–10 μm) and at a reduced sample current of 2 nA to avoid Na loss and/or migration. Counting times were 5–10 s on background and 20 s (Ni), 15 s (Ca and Ti) and 10 s for all other elements on peaks. Matrix effects were corrected using Phi (r) z modelling available on Peak Sight© software from CAMECA™. Typical standard deviations (3σ) on signal peaks for those setups are 0·3% for Si and Mg, 0·2% for Fe, 0·1–0·3% for Ca, 0·05–0·1% for Na, Al and Cr, and 0·05% for K, Ni, Ti and Mn. Standards were reanalysed either daily or after each analytical session to estimate analytical drift, which was negligible. There are no significant differences between the data from the two laboratories.

Trace element concentrations in minerals were determined in 120 μm thick sections by laser ablation inductively coupled plasma mass spectrometry (LA-ICP-MS) at Université Montpellier II with a THERMO-Finnigan™ Element2 ICP-MS system coupled to a Microlas (Geolas Q+) platform using an UV (193 nm) Excimer CompEx 102 laser operating under helium flux. Laser power was at 8 Hz and 12 J cm^{-2}, and the laser beam was 51 and 77 μm in diameter for amphibole or clinopyroxene (cpx), and 51, 102 and 122 μm for opx. For each laser ablation run, count time was 90–120 s on the carrier gas (background) followed by 60 s for signal and 30 s for fallout to drop to background level. NIST 612 glass standards were used for calibration. Standards and sample surfaces were cleaned up with 6–7 laser pulses of a 122 μm beam before analysis. Ca and Si were used as internal standards. Typical standard deviations (1σ) are derived from repeated BCR-2g reference material analyses during runs and are given in Supplementary Data (SD) Table 1 (available for downloading at http://www.petrology.oxfordjournals.org).

For each analysis, especially for opx grains with chemical zoning indicated in back-scattered electron (BSE) images, we used the smallest suitable spot size (e.g. 51 μm for the opx); the presence of inclusions and cracks was checked optically and the signal was filtered during processing to eliminate inclusion-related spikes. Elements strongly enriched in fluid or melt inclusions relative to the host mineral (e.g. Rb and Pb for opx) are not included in plots and subsequent discussion. As a further proof of the reliability of our data set, we provide raw (unfiltered) signal records (SD Fig. 1) for trace element zoning in vein opx.

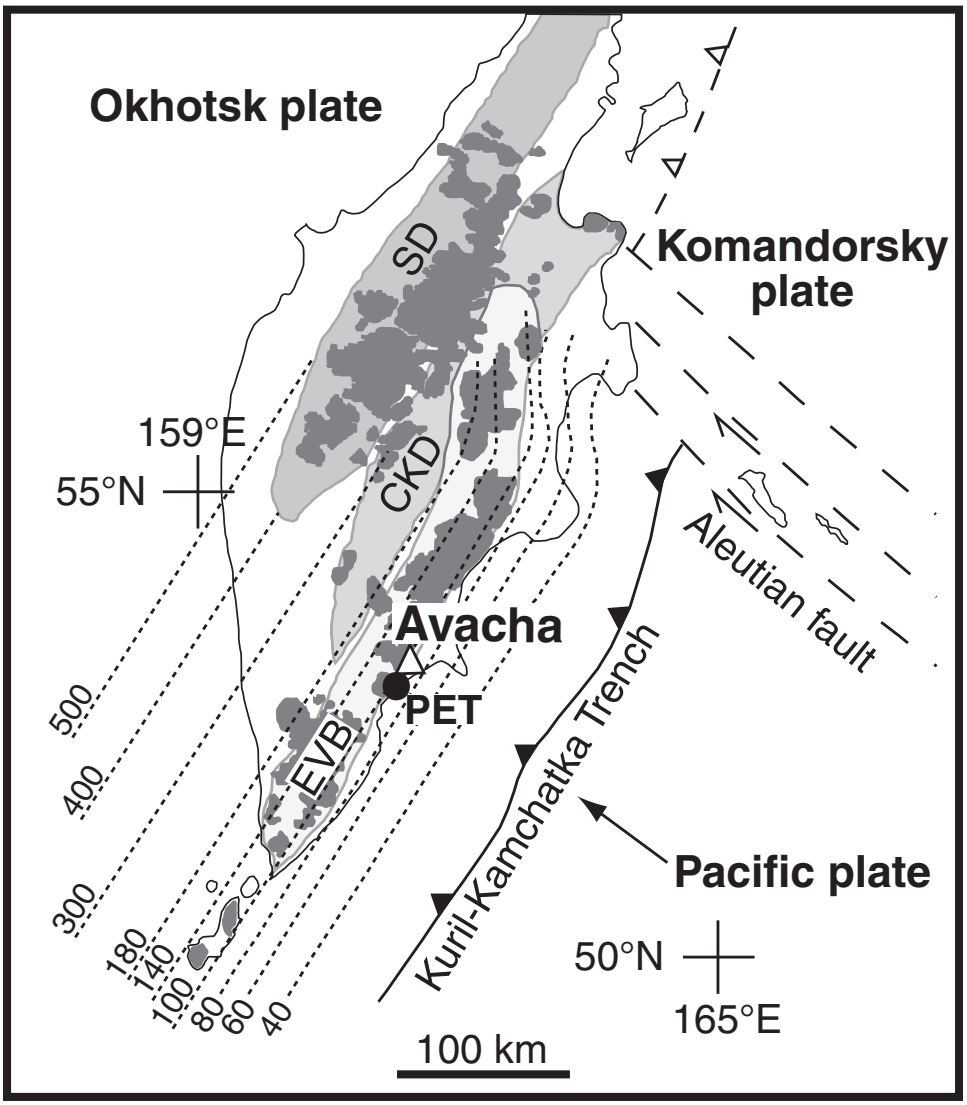

Fig. 1. Location map of the Avacha volcano in the Kamchatka peninsula, NE Russia [modified after Portnyagin *et al.* (2007)]. Major tectono-volcanic zones are shown by the light grey fill (SD, Sredinny Range; CKD, Central Kamchatka Depression; EVB, Eastern Volcanic Belt), and Quaternary volcanic rocks by the dark grey fill. The Avacha volcano is located near the city of Petropavlosk-Kamchatsky (PET). Dashed lines show the depth to the Wadati–Benioff zone after Gorbatov *et al.* (1997).

PETROGRAPHY

Host peridotites

Petrological data for representative xenoliths from our sample suite are summarized in Table 1. All the veined xenoliths are spinel (sp) harzburgites. At the contacts with the host magma they are coated with thin (≤5 mm) dark selvages of euhedral amphibole (≤1 mm) with glass, minor euhedral cpx and oxides and rounded olivine (Fig. 3). Under the microscope, the veined Avacha peridotites resemble the samples described by Ionov (2010). They are fine- to coarse-grained, with a protogranular microstructure and kink-banded olivine and opx (Fig. 4a and b and SD Fig. 2). The coarse opx commonly have cpx and spinel exsolution lamellae in the cores and are rimmed with fine-grained opx (see also Ionov, 2010); the latter is referred to here as 'opx II'. Fine-grained opx pockets interpreted as resulting from late-stage recrystallization by Ionov (2010), or by replacement of olivine by Ishimaru *et al.* (2007), are not common (SD Fig. 3). Rare coarse cpx and amphibole, referred to here as 'I', may occur next to coarse spinel (e.g. cpx I; Fig. 4a). Spinel occurs as coarse (up to 1 mm) anhedral ('sp I'; Fig. 4a) or as fine-grained (~10 μm) euhedral grains ('sp II'; Fig. 4c and SD Fig. 2).

The veined harzburgites are cut by networks of sealed, sub-parallel micro-fractures (Fig. 3b). The fractures may contain discontinuous trails of metasomatic minerals (cpx II + amphibole II ± opx II ± sulfides) as well as tiny

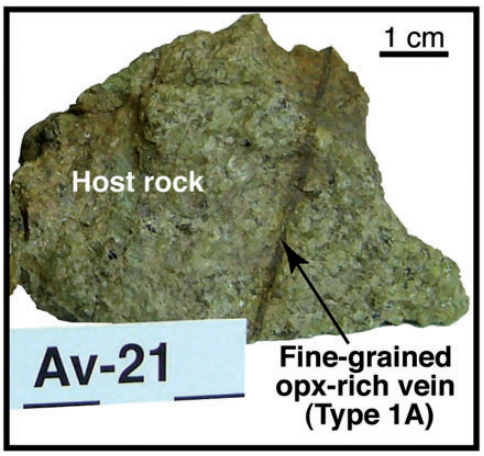

Fig. 2. A hand specimen photograph of harzburgite xenolith Av21 cross-cut by an orthopyroxene-rich magmatic vein (Type 1A). opx, orthopyroxene. A noteworthy feature is the straight and clear-cut margins of the vein, which in this case, can also be referred to as a 'dyke' according to Harte *et al.* (1993).

(~1 μm) grains of euhedral spinel (sp II), together with small (≤10 μm) fluid inclusions and empty vesicles (Fig. 4c and SD Fig. 2). When veins cut them, such fractures are referred to below as 'veins filling fractures' (vff; Fig. 4b and c).

The harzburgites contain disseminated fine-grained pockets, which we group into two types. (1) 'Type F' (F stands for fluid) pockets are exclusively located near coarse opx I or spinel I and along veins filling fractures (Fig. 4c); they contain fine-grained (~10 μm) anhedral cpx (cpx II) and amphibole (amph II) overgrowing opx I (or spinel I) and opx II, which replace host olivine (Fig. 4c and SD Fig. 2). Sulfides and euhedral spinel (sp II) may also be present (Fig. 4c). (2) 'Type L' (L for liquid) pockets are exclusively located between olivine and may contain glass films. They consist of subhedral to prismatic cpx II and amph II (≤100 μm), abundant empty vesicles and anhedral opx II overgrowing host olivine (Fig. 4d).

Vein types and vein–rock relations

The xenoliths in this study contain two major vein types, both 0·1–2 mm in thickness. The opx-rich Type 1 veins are of mantle origin (Figs 5 and 6). The amphibole-rich Type 2 veins are connected to dark materials on the surface of the xenoliths and formed from the host magma (Fig. 7 and SD Fig. 3). The Type 1 (opx-rich) veins are divided into two sub-groups based on their relations with the host peridotite and mineralogy. (1) Type 1A (or 'rapidly crystallized') veins have straight, crosscutting contacts with the host olivine; they are >500 μm thick, low in olivine and rich in sulfides (Fig. 3a). (2) Type 1B (or 'reactive') veins have irregular contacts and usually contain olivine; they may be 'thick' (≥500 μm; Fig. 3b) or 'thin' (≤500 μm; Fig. 3b).

'Rapidly crystallized' opx-rich veins (Type 1A)

Type 1A veins have well-defined, straight or slightly curved margins at the scale of tens of microns and contain no or very little interstitial glass. The central parts of Type 1A veins mainly consist of prismatic opx (≤500 μm) oriented obliquely to the vein axis, with abundant empty vesicles, small amounts (<5%) of anhedral to subhedral cpx and amphibole, rare (<1%) and small (~10 μm) olivine and spinel and sulfides (5–40 μm) (Fig. 6a). The vein margins are made up of fine-grained (~10 μm), elongated to acicular opx branching towards the vein center (Fig. 5a) and contain abundant tiny sulfide globules (5–10 μm) (Fig. 6a). BSE images show strong zoning in all vein minerals but none in the adjacent host-rock olivines (Fig. 6a).

When a Type 1A vein cuts a host opx I, it may be connected by filled fractures to Type F pockets and/or may contain subhedral amphibole and cpx (≤100 μm), and trails of opx II and anhedral cpx II ± amph II (up to 100 μm) follow fractures in the host opx I (Figs 5b and 6b).

'Reactive' opx-rich veins (Type 1B)

Type 1B thick veins (≥500 μm) have more irregular margins when cutting host olivine (Figs 5c and 6c) and usually contain more olivine, cpx and amphibole (5–10%) than Type 1A veins. They contain prismatic opx (≤300 μm; Fig. 6c), subhedral cpx and amphibole (50–100 μm) and sulfide globules (5–10 μm) near vein margins (Fig. 5c and 6c). BSE images show strong zoning in all vein minerals and only minor zoning in the adjacent host olivine (Fig. 6c).

Margins of Type 1B thick veins commonly show reaction zones (~1 mm), with relict (≤10 μm) host olivine and spinel and more abundant cpx and amphibole (usually replacing host spinel) than in the central parts of the veins (Fig. 6c). The contacts of Type 1B thick veins with the host opx are similar in form and mineralogy to those of Type 1A veins; abundant filled fractures connect Type 1B thick veins to Type F pockets in the host-rock (Figs 3b and 6d).

Type 1B thin veins (≤500 μm; Fig. 5d) have irregular margins and commonly form discontinuous trails of minerals accompanied by abundant empty vesicles and melt inclusions in the host olivine; they are made up of anhedral opx, rare cpx or amphibole and sulfide globules (Fig. 6e). Type 1B thin veins may be linked to Type L pockets.

Selvage-related amphibole-rich veins (Type 2)

Type 2 veins originate from selvages at xenolith rims and follow straight fractures in the host harzburgite (Fig. 7a and SD Fig. 3). They are dominantly (60–70%) made up of euhedral amphibole (≤250 μm) with minor opx in their central parts and fine-grained (~10 μm), anhedral to

Table 1: Summary of petrological data for representative Avacha xenoliths in this study

Sample no.	Specimen shape, appearance and texture	Mg# in host-rock coarse olivine	T (°C)*			fO_2*		Vein types
			cpx–opx (BK)	Ca–opx (BK)	ol–sp	BBG	Wood	
Av9	Angular, solid, coarse-grained	0·910		923	964	–0·27	0·09	Type 1B thin vein
Av12	Angular, solid to medium, coarse- to fine-grained	0·911		917	978	–0·11	0·36	Type 1B vein with branching veins filling fractures
Av18	Angular with amph selvage, solid, coarse-grained	0·901	969	1044	930	0·42	0·71	Type 1B vein with branching veins filling fractures
Av19	Angular with amph selvage, solid, coarse-grained	0·907	940	963	919	0·67	0·91	Type 1B thick and thin veins with branching veins filling fractures
Av20	Angular, medium, coarse-grained	0·905	937		908	0·05	0·43	Type 1A vein with branching veins filling fractures
Av21	Angular, medium, coarse- to fine-grained	0·902	947		920			Type 1A vein with branching veins filling fractures
Av27	Angular with amph selvage, medium, coarse-grained	0·905			824	–1·05	–0·61	Type 2 vein with branching Type 2 veinlets

*Calculated in host-rock minerals.
$Mg\# = Mg/(Mg + Fe)_{at}$ (averages for host-rock coarse olivine). ol, olivine; opx, orthopyroxene; cpx, clinopyroxene. Temperature estimates after cpx–opx equilibrium of Brey & Köhler (1990) (BK) are based on average of cores for cpx–opx pairs. Temperature estimates after the Ca–opx method of Brey & Köhler (1990) are based on average CaO in cores of coarse opx grains. Also reported are temperature approximations after the ol–sp method of Ballhaus *et al*. (1991) using average of cores for ol–sp pairs. In all temperature estimates, $P = 1{\cdot}5$ GPa. fO_2 [oxygen fugacity relative to fayalite–magnetite–quartz (FMQ) buffer] values are estimated after Ballhaus *et al*. (1991) (BBG) and Wood (1991) using average of cores for host-rock coarse grains, stoichiometry to estimate Fe^{3+} and Fe^{2+} in spinel (AB_2O_4 stoichiometry), and temperature values estimated from the ol–sp method of Ballhaus *et al*. (1991) at $P = 1{\cdot}5$ GPa.

acicular opx oriented at right angles to the host olivine at vein margins (Fig. 7b and SD Fig. 3). Type 2 veins contain abundant vesicles and rare sulfide globules (10–20 μm). BSE images reveal strong zoning in the vein amphibole and opx, as well as in the host olivine at vein contacts. Textures and relations with the host of Type 2 veins are very similar to those of Type 1A veins.

Veinlets with irregular contacts may originate from Type 2 veins (Fig. 7a and SD Fig. 3). The veinlets consist of anhedral opx and subhedral amphibole with size and abundances similar to those in Type 2 veins (Fig. 7c). Coarse opx I is overgrown with opx II and cpx whereas coarse spinel I is overgrown with amphibole when these minerals are cut by Type 2 veinlets (Fig. 7c). Textures and relations with the host for Type 2 veinlets are very similar to those of Type 1B thick and thin veins.

CHEMICAL COMPOSITIONS

Major elements

Representative major element analyses of minerals are given in Tables 2 and 3 and illustrated in Figs 8–12. Olivine in Type 1B veins has lower Mg# (0·89–0·90) and NiO (down to 0·21 wt %) than in the host-rocks (Fig. 8a). Compositional profiles in olivine cut by Type 1A veins show no Mg# variation, whereas those hosting Type 1B veins show an Mg# decrease towards the vein margins (Fig. 8b).

The cores of opx in Type 1A, thick Type 1B veins and host harzburgites have similar CaO contents, but the rims of opx in the veins contain more CaO than the cores (Fig. 9a and SD Fig. 1). Orthopyroxene in Type 1B veins shows greater Mg# variations (e.g. Av18) than in Type 1A veins and host-rocks (Fig. 9a). Orthopyroxene in Type 1A veins has much lower Cr_2O_3 (<0·06 wt %) than in Type 1B veins; the latter plot along the trend for host-rock opx (Fig. 9b). Orthopyroxene in Type 1B thin veins has a broad Mg# range and intermediate Cr_2O_3 contents (Fig. 9c and d).

Spinel in the central parts of Type 1A and 1B veins (i.e. not in reaction zones) commonly has lower Mg# and higher TiO_2 than spinel in the host-rocks (Fig. 10a and b). The Mg#–Cr# variation range of spinel (Fig. 10a) in Type 1B veins filling fractures and related Type F pockets (sp II) is similar to that of fine-grained spinel from Ionov (2010), whereas TiO_2 contents are lower than in Type 1B veins (Fig. 10b). Sulfide globules in the central parts of Type 1A veins are pentlandite, whereas those at the vein

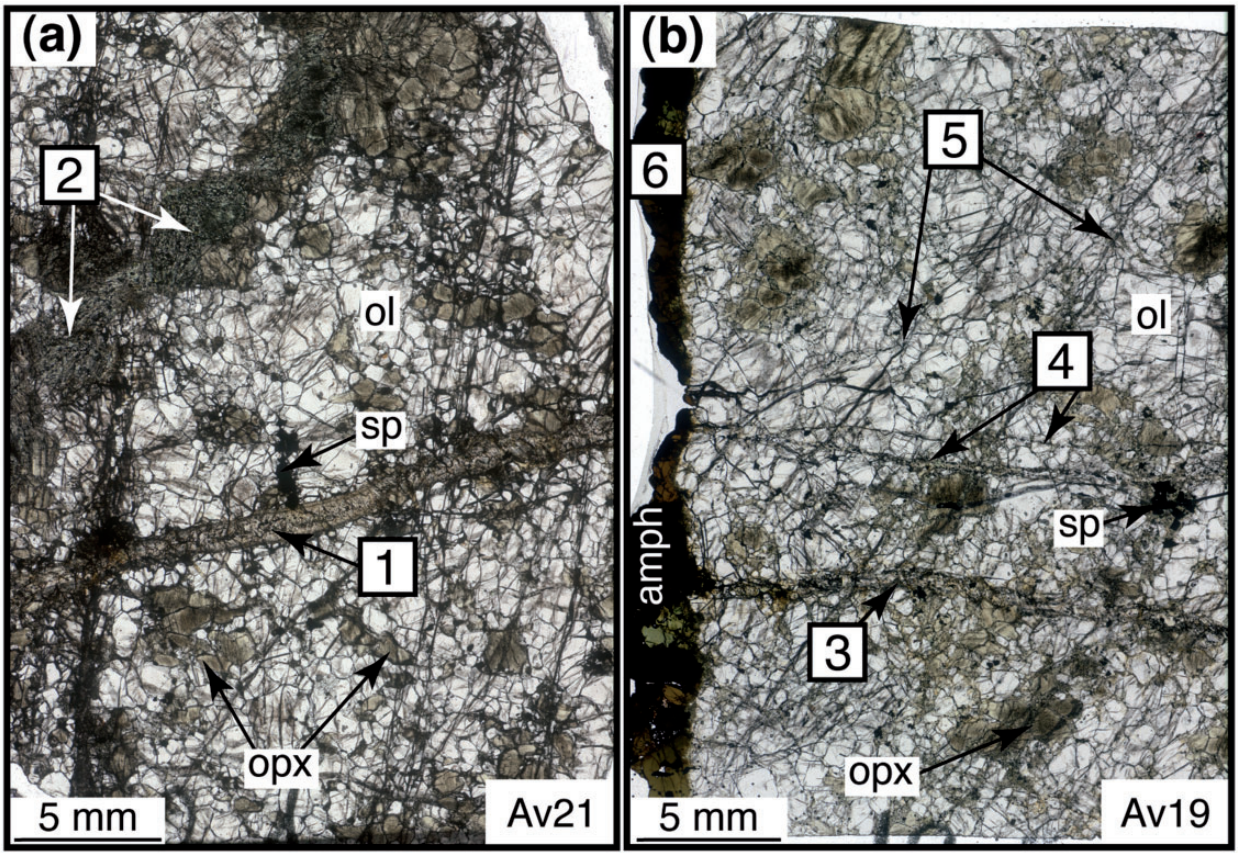

Fig. 3. Photomicrographs in transmitted light of 120 μm thick sections of harzburgite xenoliths from Avacha cut by opx-rich veins of mantle origin (Type 1). Ol, olivine; opx, orthopyroxene; amph, amphibole; sp, spinel. (a) Sample Av21 contains: (1) a thick (≥0·5 mm) opx-rich vein (or dyke, Harte *et al.*, 1993) with straight and fine-grained margins ('fringe') (Type 1A, 'rapidly crystallized') and (2) a coarse, irregular websterite vein. (b) Sample Av19 is cut by (3) a thick (≥0·5 mm) opx-rich vein with irregular margins (Type 1B, 'reactive'), (4) thin (<0·5 mm) Type 1B veins, (5) fractures partly filled with vein material ('veins filling fractures', vff) and has (6) an amphibole-rich selvage at the contact with the host magma. Photomicrographs of other veined xenoliths from this study are shown in Supplementary Data (SD) Fig. 1.

margins are pyrrhotite (Bénard & Ionov, 2010; Bénard *et al.*, 2011*b*). Additional data for cpx (diopside) in Type 1 veins and host-rocks are given in SD Fig. 4; in particular, cpx in Type 1B vein in sample Av18 has relatively low Mg# in line with opx compositions (Fig. 9a).

The amphiboles in the veined harzburgites are typically Mg-hornblendes. Ion microprobe measurements yield 2·1–2·5 wt % of H_2O in amphiboles in all Type 1 veins (Bénard *et al.*, 2011*a*), in line with their low total oxide contents (≤97 wt %, Table 2). Amphibole from Type 1A veins has higher Mg# (0·92–0·93) and lower Na_2O and Al_2O_3 (6·4–8·4 wt %) than in Type 1B veins (Fig. 11a–c). Amphibole in Type 1B veins shows a relatively wide range of Cr_2O_3 (0–2·5 wt %) and TiO_2 (0–0·35 wt %) at high and almost constant Na_2O (>2 wt %) and Al_2O_3 (>10 wt %) (Fig. 11b and c). Amphibole II in Type 1A veins filling fractures and related Type F pockets has lower TiO_2 than in Type 1A veins (Fig. 11b). Amphibole II in Type 1B veins filling fractures and related Type F pockets shows some fine chemical variations resembling those of amphibole and pyroxenes in related Type 1B veins (e.g. distinctively lower Mg# and higher TiO_2 in sample Av18, Fig. 11a, b and d). Importantly, all the distinct compositional fields for amph II in Type F and L pockets match those of the chemical end-members identified by Ionov (2010) in unveined Avacha harzburgites (Fig. 11a–d).

Representative major element analyses of minerals and glass in selvages and related Type 2 veins are given in Table 3 and shown in Fig. 12. All minerals in the selvages have much lower Mg# (0·08–0·10 for spinel, ~0·82 for cpx and 0·69–0·73 for amphibole, which is tschermakite containing 2–2·5 wt % H_2O; Bénard *et al.*, 2011*a*) than those in the xenoliths. The glass in selvages is similar in composition to the typical Avacha andesite (e.g. Ishimaru *et al.*, 2007). Orthopyroxene cores in the central parts of Type 2 veins have lower Mg# (0·88–0·91) and higher Al_2O_3 (1·5–4 wt %) than in the xenoliths, but show CaO zoning and low Cr_2O_3 contents, which mirror those of opx in Type 1A veins (Fig. 12a and b and SD Fig. 1). Amphiboles in Type 2 veins and veinlets have intermediate

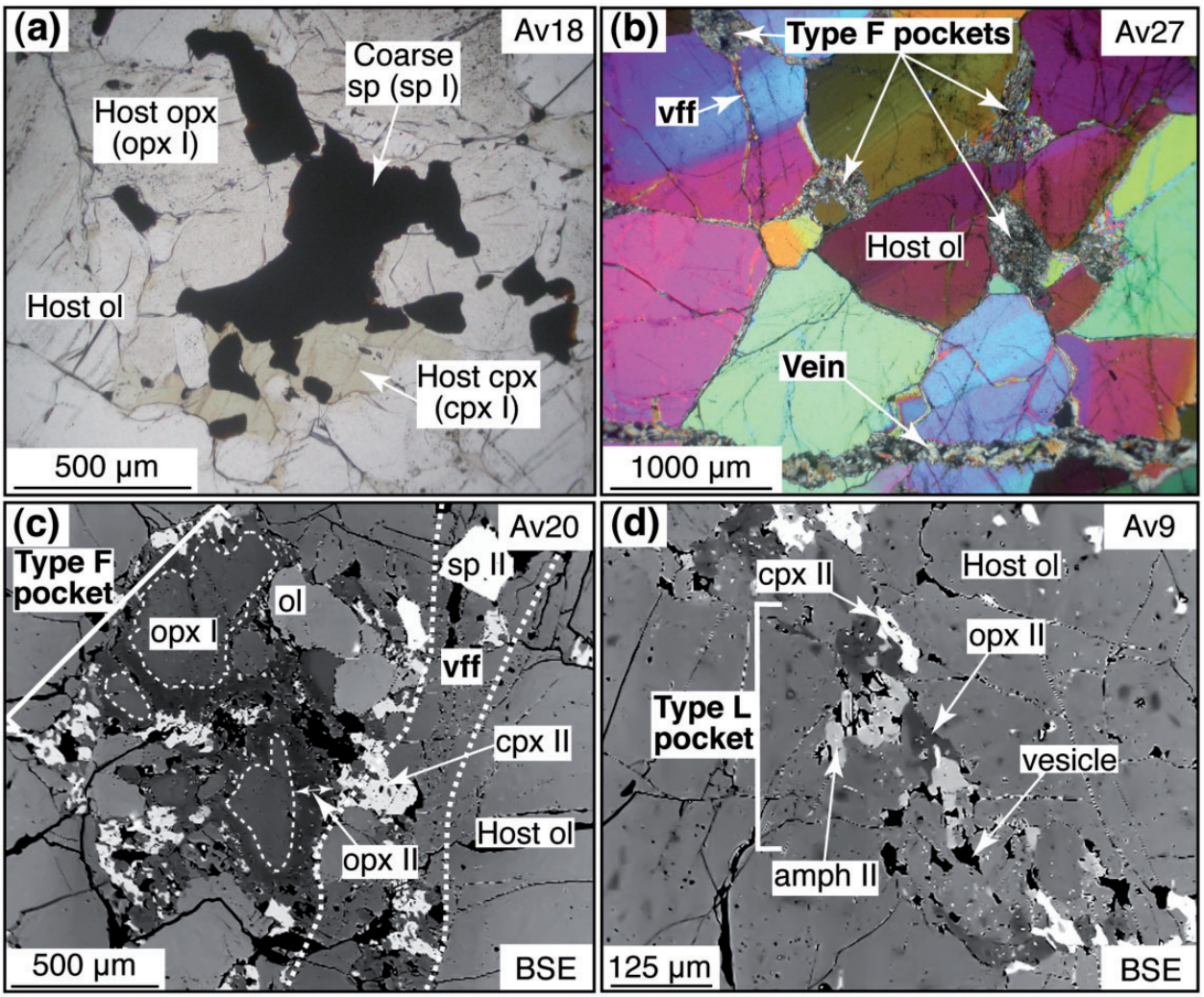

Fig. 4. Photomicrographs in plane-polarized (PPTL) and cross-polarized transmitted light (CPTL) and back-scattered electron (BSE) images of 120 μm thick sections of harzburgites from Avacha showing some key petrographical features of xenoliths hosting veins. cpx, clinopyroxene; other symbols are as in Figs 2 and 3. (a) Coarse cpx ('cpx I') adjacent to a coarse spinel ('sp I') (PPTL). (b) A vein cutting a harzburgite with abundant disseminated metasomatic pockets (Type F), some of them are connected by veins filling fractures (CPTL). (c) A BSE image of a Type F pocket crosscut by veins filling a fracture containing fine-grained euhedral spinel ('sp II'). The pocket is made up of host opx I that have darker rims ('opx II') than their cores and of anhedral and fine-grained second-generation clinopyroxene ('cpx II') overgrowing locally host opx I. (d) A BSE image of a Type L melt pocket made up of subhedral to euhedral second-generation amphibole ('amph II'), surrounded by abundant vesicles and anhedral opx II and cpx II overgrowing host-rock olivine.

Mg#, TiO_2, Al_2O_3 and Cr_2O_3 contents between those in the selvages and in the xenoliths (Fig. 12c–f).

Trace elements

Host peridotites and opx-rich veins (Type 1)

Representative LA-ICP-MS analyses of opx in Type 1 veins and host harzburgites (as well as typical errors and detection limits) are given in Table 4 and illustrated using averaged analyses in Fig. 13. REE abundances in opx I cut by Type 1 veins and veins filling fractures are typically higher than in coarse opx from the host-rocks or from unveined harzburgites reported by Ionov (2010) (Fig. 13a and b). A remarkable feature of opx in Type 1A veins is that it has higher REE in the rims than in the cores, in particular for light and middle REE (LREE and MREE) (Fig. 13c). Orthopyroxene in Type 1A veins also shows enrichment in Th and U with $[U/Th]_N > 1$ [subscript N indicates element abundances normalized to primitive mantle (PM) after McDonough & Sun (1995)] (Fig. 13d and SD Fig. 1). Importantly, opx in Type 1B thick veins has trace element patterns very similar to those of opx cores in Type 1A veins (Fig. 13e and f). By contrast, opx in Type 1B thin veins has lower MREE and positive Zr–Hf anomalies (Fig. 13e and f).

Representative trace element analyses of cpx and amphibole in Type 1 veins and host harzburgites are given in

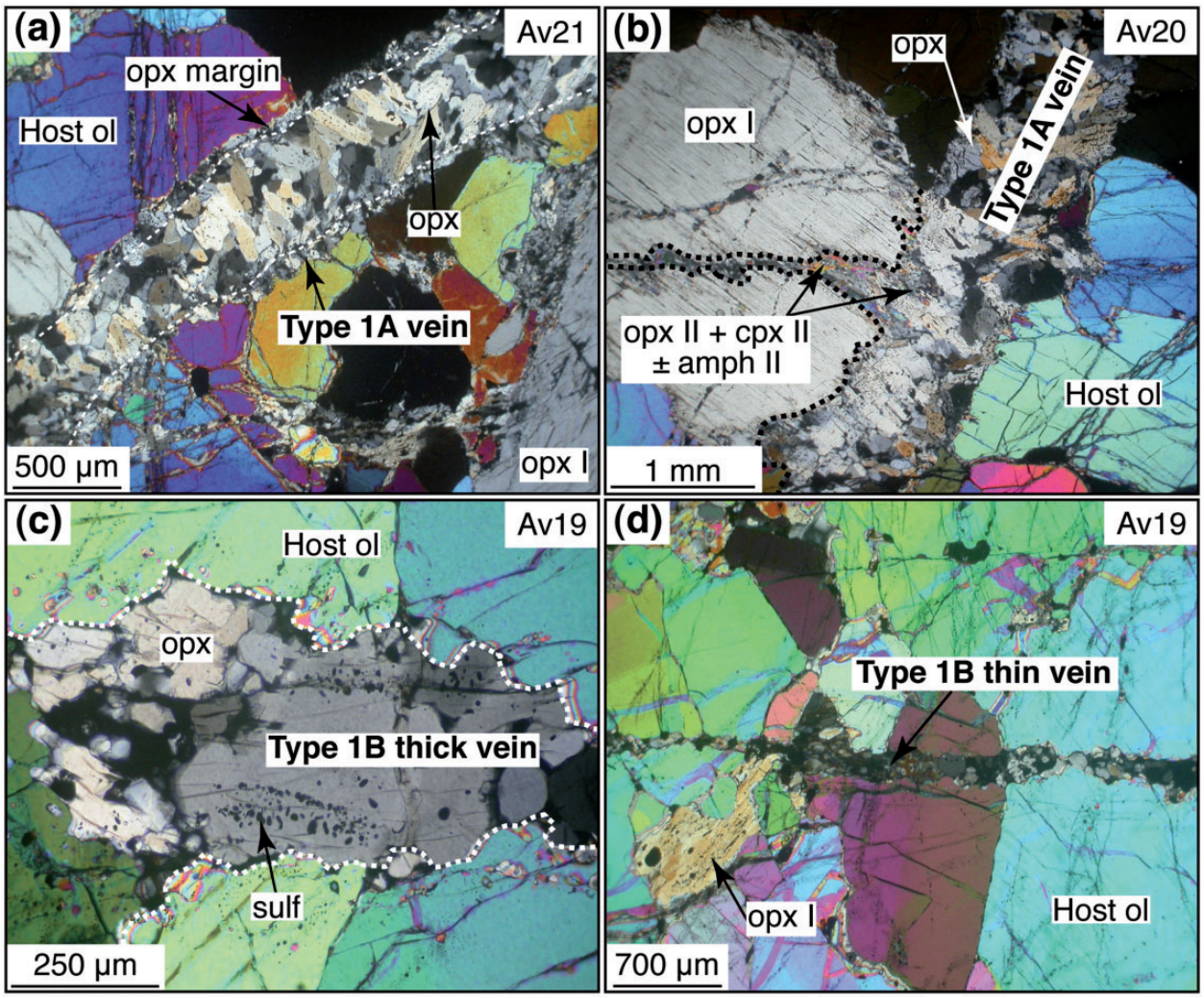

Fig. 5. Photomicrographs in CPTL of Type 1A and 1B veins, showing their relations with the host, textures and mineral associations. sulf, sulfide; other symbols are as in Figs 2–4. (a) A thick (≥0·5 mm) rapidly crystallized (Type 1A) vein with clear-cut, reaction-free contacts with the host olivine; the vein has fine-grained opx ('skeletal' grains) at its margins (fringe) and much larger sub-prismatic opx oriented obliquely to the vein axis in the centre. (b) Type 1A vein material embays a fracture in coarse opx to produce a metasomatic opx II + cpx II ± amph II assemblage. (c) A thick (≥0·5 mm) reactive opx-rich vein (Type 1B) showing irregular contacts with the host olivine. The vein is made up of subhedral opx with sulfides. (d) A reactive (Type 1B) opx-rich thin (<0·5 mm) vein has relations with host, texture and mineralogy similar to those of Type 1B thick (≥0·5 mm) veins.

Tables 5 and 6 and illustrated using averaged analyses in Figs 14 and 15 respectively. Clinopyroxene in Type 1A veins shows a gradual decrease from heavy REE (HREE) to LREE (Table 4) and thus may be out of equilibrium with vein opx, in contrast to cpx in Type 1B thick veins, which has nearly flat REE patterns and slight negative Zr–Hf anomalies (Fig. 14a and b). Clinopyroxene in Type 1B thick vein reaction zones has slightly U-shaped REE patterns ($[Tb/Lu]_N$ ~0·3), and slight Eu ($[Eu/Eu^*]_N = 1·4$) and positive Zr–Hf anomalies ($[Zr/Sm]_N$ ~2·3) (Fig. 14a and b). A crucial observation is that the trace element patterns of cpx in Type 1B thin veins and Type L pockets share common features (U-shaped REE with positive Zr–Hf spikes) with those of cpx in Type 1B thick vein reaction zones, although these are strongly accentuated in Type 1B thin veins and Type L pockets, where $[Tb/Lu]_N$ ~0·10, $[Eu/Eu^*]_N = 1·3–1·6$ and $[Zr/Sm]_N$ ~4 (Fig. 14a and b). Clinopyroxene I in the host harzburgites differs from all Type 1 vein cpx in that it has pronounced negative Zr–Hf anomalies ($[Zr/Sm]_N = 0·26–0·45$), but the gradual decrease from HREE to MREE mimics those of Type 1B thin veins and Type L pockets.

Amphiboles in Type 1A and thick 1B veins both have mildly sinusoidal REE patterns, but the former has lower REE and high field strength element (HFSE) abundances ($[Zr/Sm]_N = 0·12–0·15$, $[Ta/La]_N = 0·12–0·21$; Fig. 14c and d). Importantly, amphiboles in Type 1B thin veins and Type L pockets have strongly U-shaped REE patterns

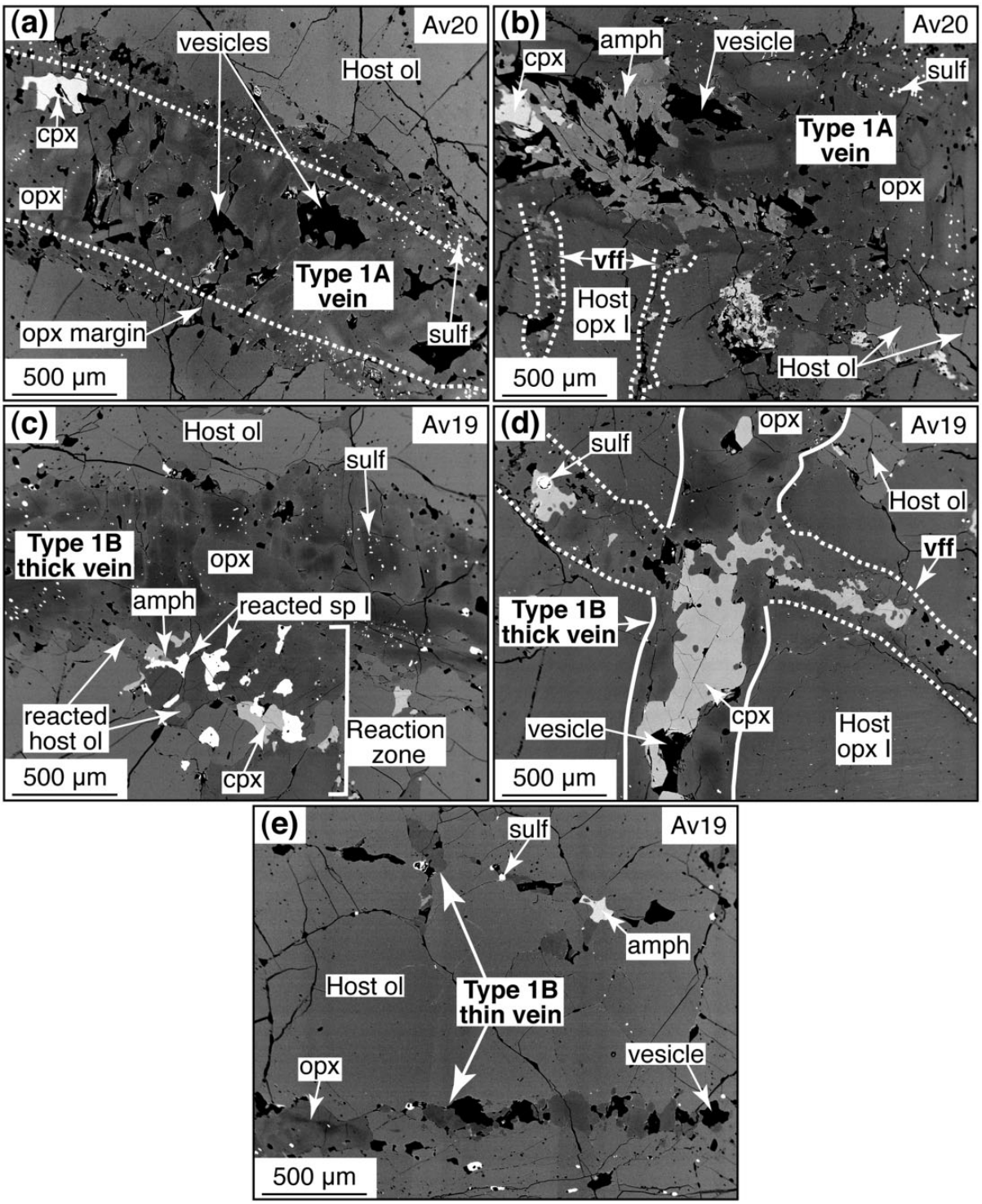

Fig. 6. BSE images of Type 1 veins (sub-types A and B) of mantle origin, showing their relations with the host, textures and mineral associations. Symbols are as in Figs 2–5. (a) A Type 1A vein with abundant sulfides at its margins (fringe); the absence of reaction with the host olivine owing to the presence of these insulating and rapidly crystallized margins should be noted. (b) A section of a Type 1A vein containing empty vesicles as well as cpx and amphibole precipitated from late-stage volatile-rich melts. The absence of sulfide in the zones with abundant cpx and amphibole in veins as well as the metasomatic assemblages (cpx II + amph II) in fractures in adjoining host opx I and pockets should be noted. (c) A sulfide-bearing, Type 1B vein with a sulfide-free reaction zone made up of opx and abundant anhedral cpx and amphibole neoblasts growing upon the host olivine (reacted host ol) and spinel relics (reacted sp I). (d) A sulfide-free reaction zone of a reactive (Type 1B) thick vein with host opx I and a branching fracture filled with cpx II and sulfide (veins filling a fracture). (e) A network of sub-parallel reactive, opx-rich thin veins (Type 1B) with sulfide globules and vesicles.

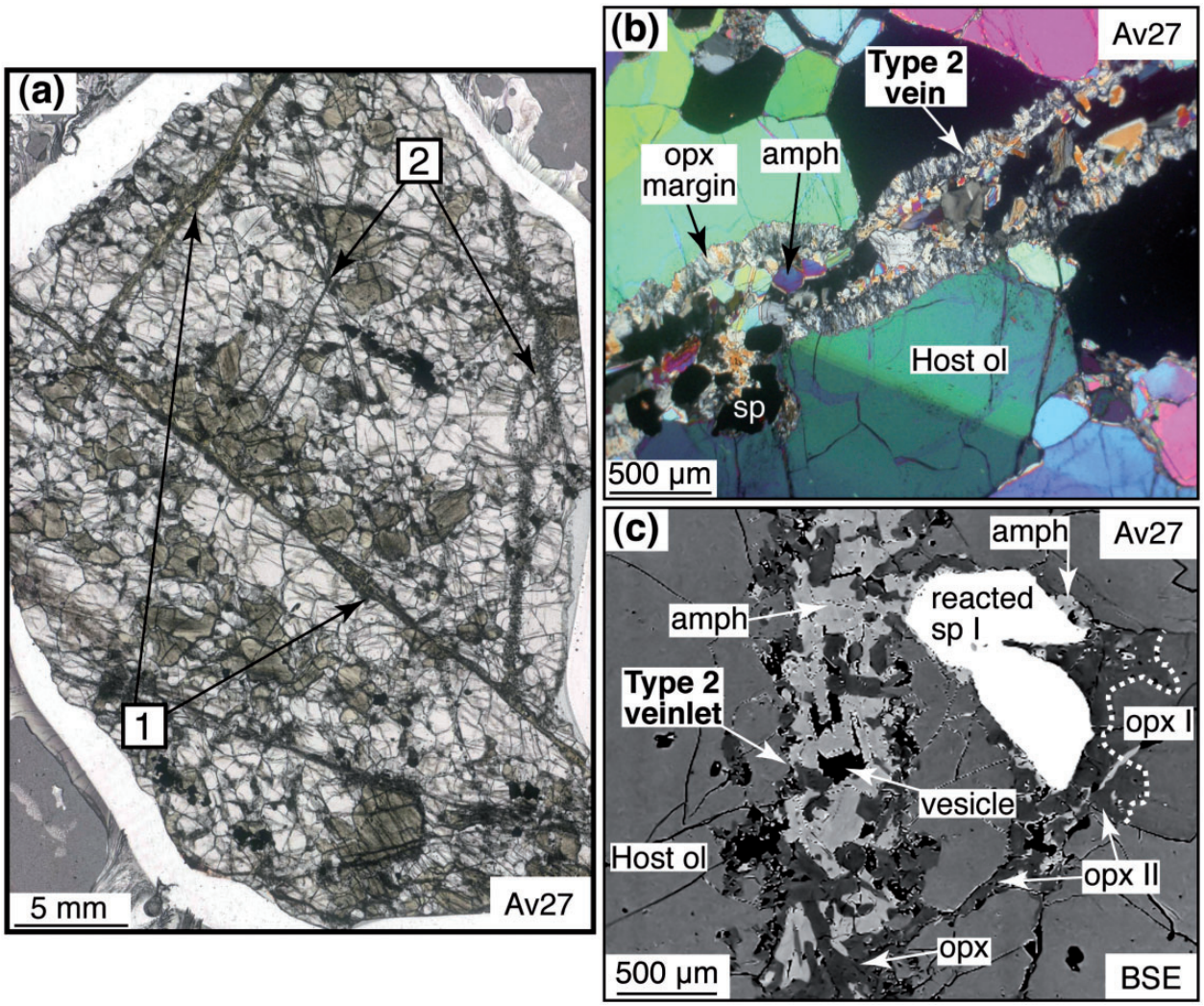

Fig. 7. Amphibole-rich veins related to selvages on xenolith rims (Type 2). Symbols are as in Figs 2–6. (a) A photomicrograph in transmitted light of sample Av27 cut by selvage-connected (1), amphibole-rich, rapidly crystallized veins with straight margins and (2) associated veinlets with irregular margins. (b) A rapidly crystallized Type 2 vein made up of fine-grained acicular opx (skeletal grains) at the margins (fringe) and euhedral and prismatic opx + amphibole in the centre (CPTL). It should be noted that this mineralogical zoning and texture are very similar to those of Type 1A veins. (c) BSE image of a Type 2 veinlet made of subhedral opx + amphibole originating from a Type 2 rapidly crystallized vein and irregularly cutting the host olivine along reactive margins (similar to those of Type 1B veins). The Type 2 veinlet reacts with host spinel I (reacted sp I) to form opx II and amphibole at spinel I rims.

and positive Zr–Hf spikes; that is, the same signatures as coexisting pyroxenes (Fig. 14c and d).

A trace element profile in minerals in Type F pockets located along a Type 1B vein filling a fracture (Fig. 15a) is illustrated using averaged analyses in Fig. 15b–h. Clinopyroxenes along the profile are characterized by a progressive depletion in LREE, MREE and Nb–Zr–Hf towards the host-rock (i.e. from cpx in Type 1B thick vein to cpx II in Type F pockets, Fig. 15b and c). Depletions in MREE and Zr–Hf are also observed in amph II along the profile (Fig. 15d and e) with $[La/Tb]_N$ increasing from 0·78 to 4·08 (Fig. 15f), $[Zr/La]_N$ decreasing from 0·96 to 0·64 (Fig. 15g) and $[Zr/Hf]_N$ becoming >1 (Fig. 15h) towards the host-rock. LREE and large ion lithophile element (LILE) abundances are roughly constant in amph II along the profile (Fig. 15d and e).

Selvages and selvage-related amphibole-rich veins (Type 2)

Representative trace element analyses of minerals and glass in selvages and related Type 2 veins are given in Table 7 and illustrated using averaged analyses in Figs 16–18. The opx in Type 2 veins are strongly zoned in LREE and MREE, as in Type 1A veins (Fig. 16a and b). Figure 17 illustrates the trace element evolution of amphiboles from selvages to Type 2 veinlets, using averaged analyses. Amphibole in selvages has slightly convex upward REE

Table 2: Representative major element compositions of minerals in host-rocks and Type 1 veins determined by EPMA

	Olivine																		
	Host-rocks														Type 1 veins				
Sample:	Av9	Av18	Av19	Av19	Av20	Av20	Av21	Av21	Av27	Av27	Av18	Av19	Av27	Av27	Av18	Av18	Av19	Av19	
Position:	core	core	core	rim	core	rim	core	rim	core	rim	rim	rim	core	rim	core	rim	core	rim	
	coarse	coarse	coarse	coarse	coarse	coarse	coarse	coarse	coarse	coarse	/1B	/1B	/2	/2	1B	1B	1B	1B	
SiO_2	41·34	41·10	41·30	41·47	41·20	41·11	41·15	40·82	40·92	40·80	40·97	41·43	41·21	40·67	40·92	40·69	40·82	41·22	
Al_2O_3	0·01	0·00	b.d.	0·04	0·00	0·02	0·01	0·01	b.d.	b.d.	0·05	0·02	0·02	0·00	0·02	0·01	0·03	b.d.	
Cr_2O_3	0·02	b.d.	0·07	0·03	b.d.	b.d.	0·00	b.d.	b.d.	0·03	b.d.	0·01	0·00	0·02	0·00	0·03	0·02	0·02	
FeO	8·77	9·74	8·83	8·95	8·49	8·57	9·80	9·60	8·87	9·29	10·18	9·94	9·05	11·23	10·40	10·72	10·09	10·36	
MnO	0·13	0·10	0·15	0·09	0·09	0·11	0·15	0·12	0·15	0·22	0·13	0·13	0·16	0·27	0·16	0·15	0·13	0·16	
MgO	49·91	48·86	49·29	49·44	49·75	49·28	48·84	48·96	48·91	48·86	48·53	48·27	48·90	47·37	48·01	47·93	48·43	48·80	
CaO	0·07	0·05	0·03	0·08	0·00	0·03	0·02	0·04	0·02	0·02	0·04	0·07	0·00	0·02	0·08	0·09	0·07	0·08	
NiO	0·41	0·34	0·34	0·28	0·31	0·28	0·42	0·41	0·30	0·32	0·29	0·23	0·36	0·45	0·28	0·27	0·21	0·22	
Total	100·69	100·22	100·07	100·39	99·90	99·41	100·46	100·01	99·17	99·56	100·20	100·11	99·72	100·07	99·87	99·88	99·80	100·89	
Mg#	0·910	0·899	0·909	0·908	0·913	0·911	0·899	0·901	0·908	0·904	0·895	0·896	0·906	0·883	0·892	0·889	0·895	0·894	

	Orthopyroxene																		
	Host-rocks									Type 1 veins									
Sample:	Av18	Av18	Av20	Av20	Av19	Av19	Av18	Av18	Av9	Av20	Av20	Av18	Av19	Av19	Av19	Av19	Av9	Av9	
Position:	core	rim	core	core	core	core	core	rim	core	core	rim	core	core	rim	core	rim	core	rim	
	I	I	I	1A-vff	1B-vff	1B-vff	1B-vff	1B-vff	L	1A	1A	1B	1B	1B	t-1B	t-1B	t-1B	t-1B	
SiO_2	56·79	57·18	56·86	58·03	57·63	57·26	57·06	56·94	58·13	58·17	57·17	57·18	58·85	57·59	59·04	57·20	58·70	56·65	
TiO_2	b.d.	0·03	0·01	0·01	b.d.	0·03	0·04	0·01	0·03	0·03	0·01	0·06	b.d.	b.d.	0·04	0·01	b.d.	b.d.	
Al_2O_3	1·87	1·61	1·60	1·02	1·37	1·82	1·37	1·51	1·00	1·31	1·11	1·77	0·46	1·27	0·58	1·78	0·85	3·08	
Cr_2O_3	0·54	0·47	0·56	0·28	0·31	0·44	0·36	0·35	0·31	0·02	0·10	0·23	b.d.	0·06	0·08	0·29	0·02	0·10	
FeO	6·15	6·09	6·05	5·39	5·83	5·82	6·16	6·10	5·65	5·76	6·83	6·64	4·09	6·02	4·59	5·92	5·25	5·84	
MnO	0·17	0·23	0·11	0·14	0·09	0·15	0·17	0·13	0·17	0·08	0·14	0·14	0·22	0·16	0·16	0·18	0·11	0·10	
MgO	33·32	33·71	33·93	35·33	34·20	34·00	34·24	34·14	34·83	34·59	34·36	33·02	36·68	34·35	36·47	34·34	35·41	34·30	
CaO	1·10	0·61	0·50	0·15	0·56	0·74	0·60	0·64	0·45	0·65	0·78	0·93	0·03	0·89	0·07	0·84	0·39	0·31	
Na_2O	b.d.	0·03	b.d.	0·00	b.d.	0·01	0·00	0·03	0·02	0·02	0·05	0·00	0·01	0·01	0·02	b.d.	0·01	b.d.	
NiO	0·09	0·05	0·02	0·03	0·11	0·08	0·09	0·10	0·10	0·13	0·04	0·06	0·02	0·05	0·03	0·05	0·04	0·05	
Total	100·03	100·01	99·64	100·37	100·10	100·34	100·10	99·94	100·69	100·78	100·59	100·03	100·35	100·40	101·06	100·61	100·79	100·44	
Mg#	0·906	0·908	0·909	0·921	0·913	0·912	0·908	0·909	0·917	0·915	0·900	0·899	0·941	0·910	0·934	0·912	0·923	0·913	

	Clinopyroxene										Spinel								
	Host-rocks						Type 1 veins				Host-rocks				Type 1 veins				
Sample:	Av18	Av20	Av20	Av18	Av19	Av9	Av20	Av20	Av18	Av9	Av27	Av27	Av19	Av19	Av21	Av21	Av18	Av18	
Position:	core	core	core	core	core	core	core	rim	core	core	core	rim	core	rim	core	rim	core	rim	
	I	1A-vff	1A-vff	1B-vff	1B-vff	L	1A	1A	1B	t-1B	I	I	1B-vff	1B-vff	1A	1A	1B	1B	
SiO_2	54·14	54·73	53·77	54·74	54·56	54·15	53·63	53·21	53·94	54·48	0·00	0·00	0·03	0·01	0·01	0·01	0·03	0·06	
TiO_2	0·03	0·00	b.d.	0·03	0·03	0·00	0·02	0·01	0·01	0·08	0·07	0·06	0·03	0·10	0·10	0·02	0·17	0·12	
Al_2O_3	1·49	0·82	1·59	1·27	1·17	1·29	1·15	2·15	1·46	1·32	22·41	20·31	23·91	21·93	19·91	19·44	20·98	16·11	
Cr_2O_3	0·72	0·33	0·55	0·45	0·41	0·66	0·87	1·07	0·75	0·52	46·82	47·16	41·08	43·26	48·00	47·09	43·04	49·08	
FeO	2·69	2·30	2·37	2·43	2·09	1·98	2·26	2·26	2·73	2·33	16·74	18·76	19·63	19·95	17·39	18·47	21·47	21·53	

(continued)

Table 2: Continued

	Clinopyroxene										Spinel							
	Host-rocks						Type 1 veins				Host-rocks				Type 1 veins			
Sample:	Av18	Av20	Av20	Av18	Av19	Av9	Av20	Av20	Av18	Av9	Av27	Av27	Av19	Av19	Av21	Av21	Av18	Av18
Position:	core	core	core	core	core	core	core	rim	core	core	core	rim	core	rim	core	rim	core	rim
	I	1A-vff	1A-vff	1B-vff	1B-vff	L	1A	1A	1B	t-1B	I	I	1B-vff	1B-vff	1A	1A	1B	1B
MnO	0·09	0·06	0·11	0·12	0·08	0·07	0·04	0·09	0·11	0·11	0·24	0·38	0·24	0·25	0·27	0·22	0·19	0·27
MgO	17·84	17·89	17·57	17·61	17·96	17·84	18·52	17·10	17·76	17·72	13·53	11·98	13·90	13·88	12·81	12·74	12·62	11·74
CaO	22·85	24·13	23·85	23·89	24·31	23·71	23·14	23·88	22·83	23·35	0·00	n.d.	n.d.	n.d.	n.d.	n.d.	n.d.	n.d.
Na_2O	0·24	0·08	0·09	0·12	0·14	0·09	0·26	0·12	0·19	0·15	0·00	n.d.	n.d.	n.d.	n.d.	n.d.	n.d.	n.d.
NiO	0·04	0·06	0·08	0·04	0·00	0·08	0·07	0·04	0·04	0·05	0·12	0·10	0·12	0·10	0·05	0·05	0·14	0·09
Total	100·13	100·40	99·98	100·70	100·75	99·88	99·99	99·94	99·83	100·10	99·92	98·81	98·96	99·49	98·54	98·08	98·67	99·03
Mg#	0·922	0·933	0·930	0·928	0·939	0·941	0·936	0·931	0·921	0·931	0·590	0·532	0·558	0·554	0·568	0·551	0·512	0·493
Cr#	0·245	0·214	0·190	0·194	0·189	0·255	0·337	0·251	0·257	0·208	0·584	0·609	0·535	0·570	0·618	0·619	0·579	0·671

	Amphibole																	
	Host-rocks										Type 1 veins							
Sample:	Av18	Av18	Av20	Av20	Av18	Av18	Av19	Av19	Av9	Av9	Av20	Av20	Av20	Av20	Av18	Av18	Av9	Av9
Position:	core	rim	core	core	core	rim	core	rim	core	rim	core	rim	core	rim	core	rim	core	rim
	I	I	1A-vff	1A-vff	1B-vff	1B-vff	1B-vff	1B-vff	L	L	1A	1A	1A-rz	1A-rz	1B	1B	t-1B	t-1B
SiO_2	46·80	47·50	52·44	49·70	46·60	46·10	47·24	46·78	47·58	47·06	51·81	50·08	54·76	48·39	47·51	46·09	46·25	46·15
TiO_2	0·00	0·10	0·17	0·00	0·18	0·21	0·12	0·09	0·04	0·08	0·11	0·20	0·06	0·18	0·05	0·24	0·06	0·07
Al_2O_3	11·48	11·25	5·87	8·13	11·42	11·79	11·44	11·14	9·96	10·28	6·63	8·00	3·71	8·74	10·86	11·65	11·16	10·81
Cr_2O_3	0·67	0·71	0·75	1·28	1·40	1·66	0·69	1·44	1·95	1·79	0·47	0·47	0·65	0·69	0·38	0·80	2·30	2·30
FeO	4·14	4·29	2·78	3·21	4·35	4·25	3·78	3·87	3·67	3·46	2·95	3·06	2·59	3·27	4·43	4·59	3·70	3·63
MnO	0·09	0·02	0·02	0·06	0·04	0·07	0·04	0·10	0·06	0·06	0·00	0·01	0·05	0·04	0·03	0·04	0·09	0·04
MgO	19·18	19·41	21·44	20·20	18·92	18·73	19·30	19·43	19·30	19·13	21·12	20·71	22·63	20·65	19·59	18·96	18·89	18·55
CaO	11·95	11·73	12·32	12·43	11·79	11·71	12·13	11·99	11·78	11·79	12·47	12·44	12·01	12·43	11·55	11·75	11·86	11·67
Na_2O	2·15	2·17	1·06	1·27	2·19	2·22	2·22	2·25	2·04	2·00	1·11	1·37	0·87	1·52	2·15	2·13	2·36	2·31
K_2O	n.d.	n.d.	n.d.	n.d.	n.d.	n.d.	n.d.	n.d.	0·25	0·30	n.d.	n.d.	0·22	0·93	n.d.	n.d.	0·31	0·28
NiO	0·09	0·09	0·13	0·07	0·07	0·08	0·10	0·05	0·11	0·09	0·05	0·11	0·13	0·10	0·07	0·09	0·11	0·15
Total	96·55	97·27	96·99	96·36	96·95	96·83	97·05	97·14	96·73	96·04	96·72	96·44	97·69	96·93	96·62	96·34	97·10	95·96
Mg#	0·892	0·890	0·932	0·918	0·886	0·887	0·901	0·900	0·904	0·908	0·927	0·924	0·940	0·918	0·888	0·880	0·901	0·901
Cr#	0·038	0·040	0·079	0·096	0·076	0·086	0·039	0·080	0·116	0·105	0·045	0·038	0·105	0·050	0·023	0·044	0·122	0·125

b.d., below detection limit; n.d., no data; coarse, coarse mineral in host-rock; /1B, coarse host mineral against Type 1B vein; /2, coarse host mineral against Type 2 vein; 1B, mineral in thick Type 1B vein. I, coarse first generation ('I') host mineral; 1A-vff, second generation ('II') host mineral in Type F pocket along Type 1A veins filling fractures; 1B-vff, second generation ('II') host mineral in Type F pocket along Type 1B veins filling fractures; L, second generation ('II') host mineral in Type L pocket; 1A, mineral in Type 1A vein central part; t-1B, mineral in thin Type 1B vein. $Cr\# = Cr/(Cr + Al)_{at}$. 1A-rz, mineral in Type 1A vein reaction zone in host opx.

patterns ($[La/Tb]_N = 0·02–0·08$) at much higher MREE abundances than in Type 1 veins (~5 × PM abundance for Tb), strong Zr–Hf negative anomalies ($[Zr/Sm]_N = 0·19–0·24$), high $[Ba/Rb]_N$ (~7) and positive Sr anomalies (Fig. 17a–d). Amphibole in Type 2 veins has trace element patterns similar to those in the selvages but at 3–4 times higher REE and HFSE levels (Fig. 17c and d). Amphibole in Type 2 veinlets has higher LREE, lower MREE and HREE ($[Pr/Tb]_N = 2·61–5·68$, Fig. 17c), and higher Nb, Ta, Zr, Th and U than in Type 2 veins (Fig. 17d). Importantly, amphibole in Type 2 veinlets has U-shaped REE patterns with positive Zr–Hf spikes, similar to amphibole and cpx in Type 1B thin veins and Type L pockets. As for minerals in Type 1B thick vein reaction zones, Type 1B thin veins and

Table 3: Representative major element compositions of minerals and glass in selvages and Type 2 veins determined by EPMA

Sample:	Av18	Av19	Av19	Av19	Av19	Av18	Av19	Av19	Av18	Av18	Av19	Av19	Av27	Av28	Av27	Av27	Av27	Av27	Av27
Phase:	olivine	spinel	spinel	spinel	spinel	cpx	amph	amph	glass	glass	glass	glass	opx	opx	opx	amph	amph	amph	amph
Position:	core	core	rim	core	rim	core	core	rim	core	core	core	core	core	rim	core	core	rim	core	rim
	selv	selv	selv	selv	selv	selv	selv	selv	selv	selv	selv	selv	2	2	2′	2	2	2′	2′
SiO_2	38·81	0·07	0·08	0·06	0·07	51·11	41·50	41·25	57·60	57·43	58·42	57·37	56·16	55·24	55·84	47·05	46·15	47·93	45·14
TiO_2	n.d.	6·39	6·46	7·29	7·27	0·44	1·91	2·02	0·52	0·49	0·51	0·54	0·07	0·26	0·26	0·95	0·73	0·11	0·21
Al_2O_3	b.d.	7·80	7·82	8·36	8·38	3·17	14·01	13·95	19·68	19·53	19·62	19·45	3·34	4·02	3·60	10·47	11·56	11·03	13·86
Cr_2O_3	b.d.	0·08	0·11	0·18	0·13	0·12	0·19	0·06	0·00	0·08	0·00	0·07	0·03	0·02	b.d.	0·30	0·00	0·00	0·53
FeO	20·32	75·17	75·65	74·18	73·70	5·86	9·49	11·14	5·77	5·93	5·98	5·97	7·19	7·26	6·31	5·35	5·93	4·15	4·50
MnO	0·27	0·27	0·16	0·26	0·30	0·14	0·09	0·11	0·17	0·09	0·05	0·17	0·30	0·27	0·11	0·17	0·21	0·10	0·05
MgO	40·34	3·96	3·89	4·72	4·60	15·24	15·11	14·00	3·14	3·03	3·02	2·63	33·13	32·28	33·05	19·00	18·65	19·97	18·62
CaO	0·09	n.d.	n.d.	n.d.	n.d.	22·84	12·11	12·17	7·73	8·12	7·27	7·76	0·31	1·03	0·95	10·97	11·20	11·61	11·69
Na_2O	n.d.	n.d.	n.d.	n.d.	n.d.	0·28	2·56	2·48	3·93	4·14	3·95	4·00	0·03	0·01	0·02	2·13	2·04	2·10	2·37
K_2O	n.d.	n.d.	n.d.	n.d.	n.d.	n.d.	0·25	0·24	0·68	0·68	0·72	0·62	n.d.	0·00	n.d.	n.d.	n.d.	n.d.	n.d.
NiO	0·10	0·05	0·04	0·07	0·05	0·02	b.d.	0·00	n.d.	n.d.	n.d.	n.d.	0·11	0·13	0·16	0·10	0·12	0·16	0·17
Total	99·99	93·81	94·22	95·21	94·56	99·21	97·22	97·43	99·29	99·62	99·62	98·65	100·64	100·52	100·29	96·47	96·60	97·16	97·14
Mg#	0·780	0·086	0·084	0·102	0·100	0·823	0·739	0·691	0·766	0·777	0·779	0·802	0·892	0·888	0·903	0·864	0·849	0·896	0·881
Cr#	n.d.	0·007	0·009	0·014	0·011	0·025	0·009	0·003	n.d	n.d	n.d	n.d	n.d.	n.d.	n.d.	0·019	0·000	0·000	0·025

b.d., below detection limit; n.d., no data; cpx, clinopyroxene; amph, amphibole; opx, orthopyroxene; selv, mineral in selvages coating the xenoliths; 2, mineral in Type 2 vein central part; 2′, mineral in Type 2 veinlet.

Type L pockets, amphibole in Type 2 veinlets has relatively low $[U/Th]_N$ (Fig. 17e), $[Zr/Hf]_N > 1$ and a broad range of LREE/MREE and Zr/MREE ratios (Fig. 17f and g). Glass in the selvages has a trace element signature similar to that of typical Avacha andesites (Fig. 18).

DISCUSSION

Melt types and sources

Before discussing the nature and the sources of the initial liquids which intruded the Avacha harzburgite and formed the Type 1A and Type 2 veins, we examine the key observations on the crystallization histories of the veins and the absence of melt–rock interaction.

(1) The straight margins of Type 1A and Type 2 veins (Figs 2, 3a, 7a and SD Fig. 3) suggest that their parental liquids intruded the host harzburgites by hydraulic fracturing. In this regard, the veins can be classified as 'dykes' after Harte *et al.* (1993), which implies little interaction with the host compared with percolation during pervasive metasomatism.

(2) The margins of the veins are made up of fine-grained minerals (mostly opx), which branch inward (Figs 3a, 7 and SD Fig. 3). Similar textures are commonly found at the margins of pegmatitic dykes (referred to as 'fringes'), which contain, as for the Type 1A and Type 2 veins, fine acicular or skeletal crystals. The fringes form almost instantly as a result of 'undercooling' of the intruding liquids and effectively prevent chemical exchange between the remaining liquid and the host (Cerny *et al.*, 2012; London & Morgan, 2012, and references therein).

(3) Zoned mineral assemblages [e.g. pyrrhotite at margins vs pentlandite in the central parts of Type 1A veins (Bénard & Ionov, 2010; Bénard *et al.*, 2011*b*)], inwardly coarsening crystals, crystal orientation (e.g. Fig. 5a) and the near-absence of glass in Type 1A and Type 2 veins imply the complete crystallization of their parental liquids in closed systems, as in pegmatitic dykes (London & Morgan, 2012, and references therein).

(4) Our chemical dataset is consistent with the textural evidence. Ca and Fe zoning in prismatic opx crystals from the central parts of the Type 1A and Type 2 veins (Figs 6a, 9a, 12a and 17b) indicates that their parental liquids crystallized very rapidly. This rapid crystallization, together with the sealing of contacts by the fringes, must have strongly limited the interaction of the solidifying liquids with the host peridotite.

(5) A remarkable feature of the chemical zoning in Type 1A and Type 2 veins is the core to rim LREE and MREE enrichment in opx from their central parts (Figs 13d and 16b). Because LREE and MREE are highly incompatible in opx (e.g. McDade *et al.*, 2003), these elements are enriched in

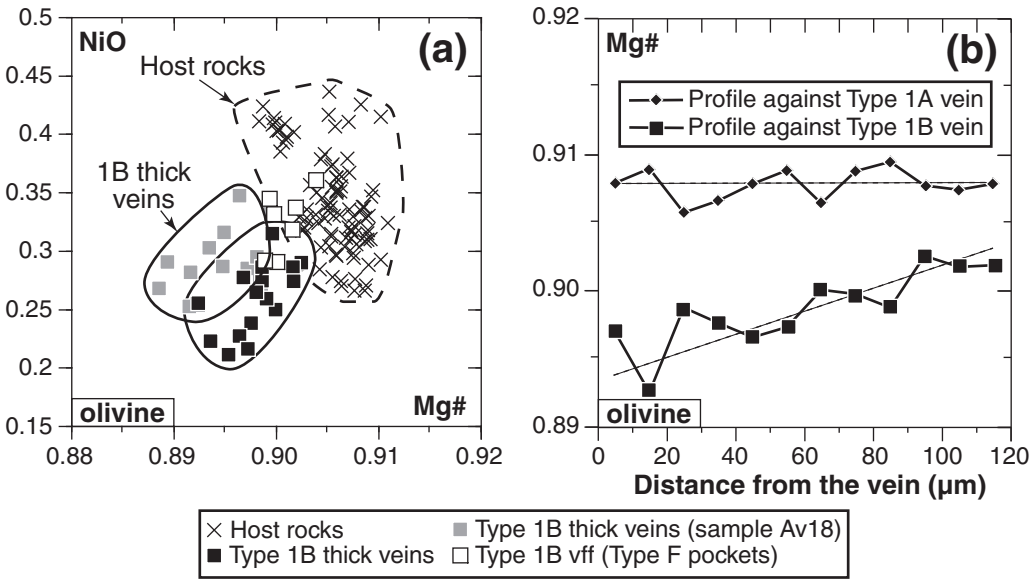

Fig. 8. Olivine compositions. (a) Covariation plot of NiO vs Mg# for host-rock olivine (dashed-outline field) and olivine in Type 1B vein systems. Olivine compositions in the Type 1B veins lie along a Ni–Mg depletion trend relative to the host olivine compositional field. (b) Mg# profiles in host-rock olivine across Type 1A and 1B vein margins. No variation in host olivine composition is observed across Type 1A vein margins whereas they are Fe-enriched along those of Type 1B veins. In this diagram and subsequent ones reporting major element data, typical errors derived from EPMA analyses (3σ) are covered by the symbol size. (See Table 2 for representative analyses.)

narrow boundary layers of liquid at the crystallization front ('constitutional zone refining'; London, 2009), which implies rapid closed-system crystallization.

(6) Major element compositions of opx (Figs 9b and 12b) and amphibole (Figs 11 and 12c–f) in Type 1A and Type 2 veins are distinct from those in the host peridotites and other vein types, suggesting an origin from liquids that preserved their chemical signatures owing to rapid crystallization with little reaction with host peridotites.

Initial melt of Type 1 veins

Recently, Bénard & Ionov (2012) published a major and trace element model supporting the origin of Type 1 veins from a high-temperature (>1300°C) low-Ca boninitic melt with low trace element abundances. In this section, we review new evidence for the origin of the Type 1 veins obtained in this study in relation to the conclusions of Bénard & Ionov (2012).

The textures of Type 1A veins, especially the presence of fine-grained fringes, indicate that they crystallized from a viscous fluid, probably a Si-rich melt experiencing undercooling (London & Morgan, 2012). Because the temperatures calculated from the host xenolith mineral assemblages in this (Table 1) and previous studies (Halama *et al.*, 2009; Ionov, 2010) range between 900 and 1050°C, the initial melt must have intruded at a much higher temperature. Both Type 1A and thick Type 1B veins contain olivine and have opx-rich modal compositions with particularly Mg-rich minerals compared with pyroxenite veins reported from mantle sections in subduction-related settings (e.g. Varfalvy *et al.*, 1996; Garrido *et al.*, 2007). In addition, incompatible major elements (e.g. Al, Ti and Na) are particularly low in all Type 1A vein minerals (Figs 9b, 10b and 11c, d). The abundance of vesicles in Type 1A and thick Type 1B veins suggests that a fluid phase exsolved during crystallization, and the presence of amphibole indicates that the initial melt contained water. Crystallization experiments on refractory, H_2O-rich, Mg-rich silicic melts at 2·5 GPa (Stalder, 2002), in line with other phase equilibrium data on (H_2O)–MgO–SiO_2 systems at 1·5–2 GPa (e.g. Inoue, 1994; Thompson *et al.*, 2007), show that enstatite may be the major phase to crystallize from 1200 to 900°C at mantle wedge pressures; the opx forms after olivine, which is dominant between 1400 and 1200°C. It follows that cpx and amphibole in Type 1A and thick Type 1B veins must have crystallized during late-stage evolution of the residual melt at 1000–900°C. To sum up, our data indicate that Type 1A and thick 1B veins formed from a high-temperature, Mg- and Si-rich mantle melt low in Al, Ca and Na, in line with the low-Ca boninitic composition suggested by Bénard & Ionov (2012). The melt may have formed by fluxed-melting of a harzburgitic source at relatively low pressure (≤1·5 GPa) (Gaetani & Grove, 1998; Falloon & Danyushevsky, 2000; Ulmer, 2001; Parman & Grove, 2004).

The low abundances of moderately incompatible lithophile trace elements in opx, cpx and amphibole in Type 1A and thick Type 1B veins (Figs 13 and 14) relative to those minerals in common magmatic rocks and most mantle xenoliths (e.g. Ionov *et al.*, 2002; Coltorti *et al.*, 2007) indicate that the melt source was highly depleted.

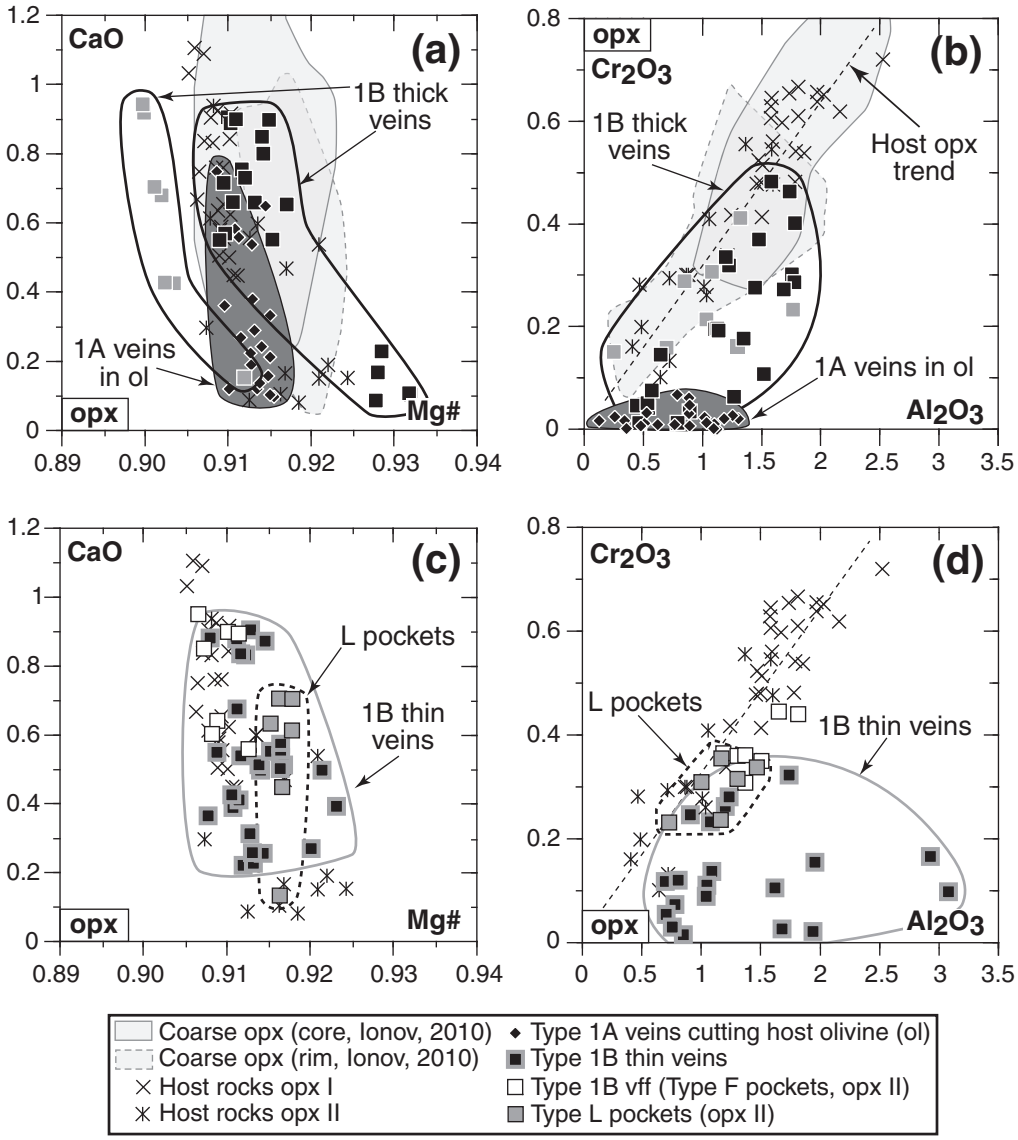

Fig. 9. Orthopyroxene compositions in host-rocks and veins of mantle origin (Types 1A and 1B). (a, b) Covariation plots for opx I and II from host-rocks, Type 1A veins (dark grey field), and thick Type 1B veins (continuous black-outline field) compared with data for opx in Avacha harzburgites from Ionov (2010) (light grey field for opx cores and dashed-outline light grey field for opx rims). Noteworthy features are the Ca zoning in all opx, the Mg# variability in the Type 1B opx from one sample to another, and that these opx tend to lie along the Cr–Al host opx trend. (c, d) Co-variation plots for opx from thin Type 1B veins (grey-outline field), Type F pockets (Type 1B veins filling fractures) and Type L pockets (dashed field). Other fields and symbols are the same as in Figs 2–8. (See Table 2 for representative analyses.)

We estimated the trace element abundances in the parental melt assuming it was in equilibrium with opx cores in Type 1A veins, whereas cpx and amphibole may have crystallized from late-stage, residual melts. The calculated melt is very low in HREE (e.g. ~0·5 × PM for Lu), which supports its generation from a highly depleted mantle source, and has a flat HREE–MREE pattern very similar to the high-Ca boninitic parental melt modelled at 1200°C for Type 1 veins by Bénard & Ionov (2012) (Fig. 18). Minor discrepancies for LREE between our calculations and the modelled melt from Bénard & Ionov (2012) are due to much higher abundances of cpx (which buffers LREE) in the experiments from which the $D^{opx/melt}$ partition coefficients we used were derived (Green *et al.*, 2000; McDade *et al.*, 2003) than in the veins.

Initial melt of Type 2 veins

Because the selvage and Type 2 vein minerals have much lower Mg#, higher Ti and Al (Fig. 12) and higher REE (Fig. 17) than those in Type 1 veins, they must have crystallized from much more evolved, amphibole-saturated melts. The slightly convex upward REE patterns, negative

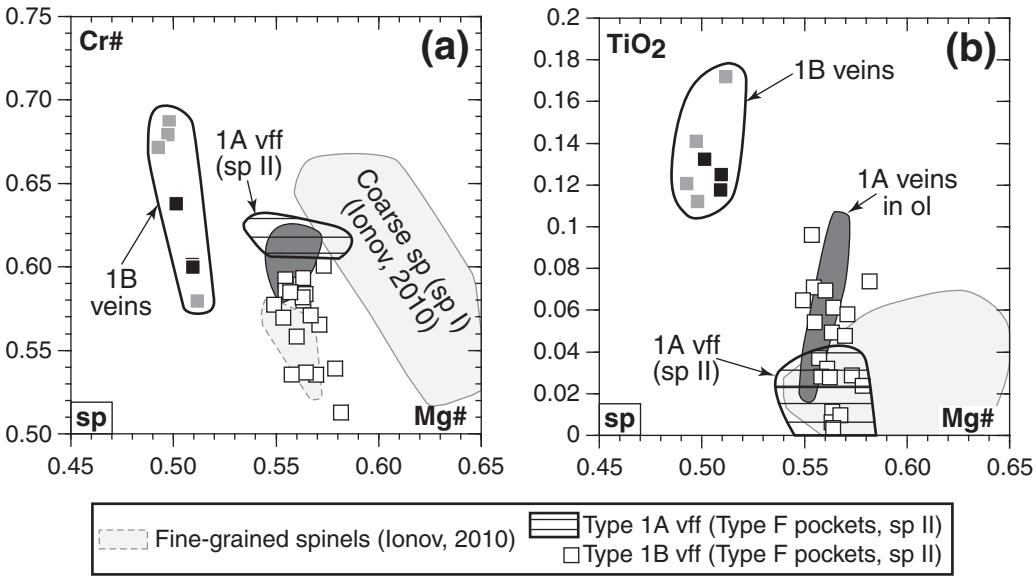

Fig. 10. Spinel compositions in host-rocks and veins of mantle origin (Types 1A and 1B). (a, b) Covariation plots for spinel from Type 1A veins and related veins filling fractures (spinel II, hatched field) and Type 1B veins and related veins filling fractures (spinel II), compared with data for spinel in Avacha harzburgites from Ionov (2010), including fine-grained spinel (dashed light-grey field). No data on relict spinel grains from the host (see Figs 6c and 7c) are reported in this diagram. Other fields and symbols are the same as in Figs 2–9. The spinel II in veins filling fractures have broadly the same compositions as the fine-grained spinels reported by Ionov (2010), whereas those in Types 1A and 1B veins tend to have higher Ti contents. (See Table 2 for representative analyses.)

HFSE anomalies and LILE enrichments in their amphibole (Fig. 17c, d and Table 3) indicate that the selvages are crystal segregates from evolved hydrous arc-type magmas. Pressures and temperatures estimated after Ridolfi *et al.* (2010) from the composition of the amphibole in the selvages yield 0·4–0·6 GPa and 925–1050°C, suggesting their formation in the lower to mid-crust. The glass coexisting with the amphibole in the selvages is similar in major and trace element composition to the Avacha andesite (Fig. 18 and Tables 3 and 7), and partition coefficients between calc-alkaline melt and amphibole determined at high pressure ($D^{amphibole/melt}$, Tiepolo *et al.*, 2007) show that the amphibole and glass in the selvages are in equilibrium. The similarity between the REE patterns and Rb/Ba ratios of the amphiboles in the selvages and in Type 2 veins, the latter with REE abundances 3–4 times higher than the former, lead us to conclude that the parental melt of Type 2 veins is a fractionation product of the andesitic melt that crystallized the selvages. Crystallization of the selvages at depth must have produced residual volatile-rich liquids that filled fractures in the xenoliths during their ascent or storage in crustal magma chambers to form Type 2 veins.

Melt–rock interaction processes ('fractionation–reactive percolation')

In the following section, we examine the key topic of this study—the modifications suffered by percolating melts in sub-arc mantle rocks. To characterize these processes, we use the inferences on the initial liquids from the previous section and from Bénard & Ionov (2012), as well as our new data on Type 1B veins and Type 2 veinlets, to argue that the percolating melts show a combination of (1) differentiation caused by crystal fractionation and (2) reactions to achieve equilibrium with the host-rocks. We show that the overall process, referred to here as 'fractionation–reactive percolation' (see Harte *et al.*, 1993), profoundly transforms the geochemical characteristics of the percolating liquids.

Melt fractionation

Whereas similar mineralogy and mineral chemistry in Type 1A and Type 1B thick veins indicate that these two vein types formed from similar liquids (e.g. Bénard & Ionov, 2012), several lines of evidence suggest that Type 1B veins record higher degrees of fractionation of their parental melt during percolation. Spinel in thick Type 1B veins has much lower Mg# and higher TiO_2 than in Type 1A veins (Fig. 10). Thick Type 1B veins are opx-rich like Type 1A veins but contain more abundant accessory cpx and amphibole; the latter crystallize at lower temperatures than opx and have lower Mg# and higher Na, Ti and Al in Type 1B than in Type 1A veins (Fig. 11a–c). The higher amphibole abundances in Type 1B thick veins are of particular interest as they suggest increasing H_2O activity as the parental melt of the Type 1 veins evolved during percolation. These results are in line with recent experiments, which show that continuous differentiation of a melt in channels at decreasing temperature and high pressure can

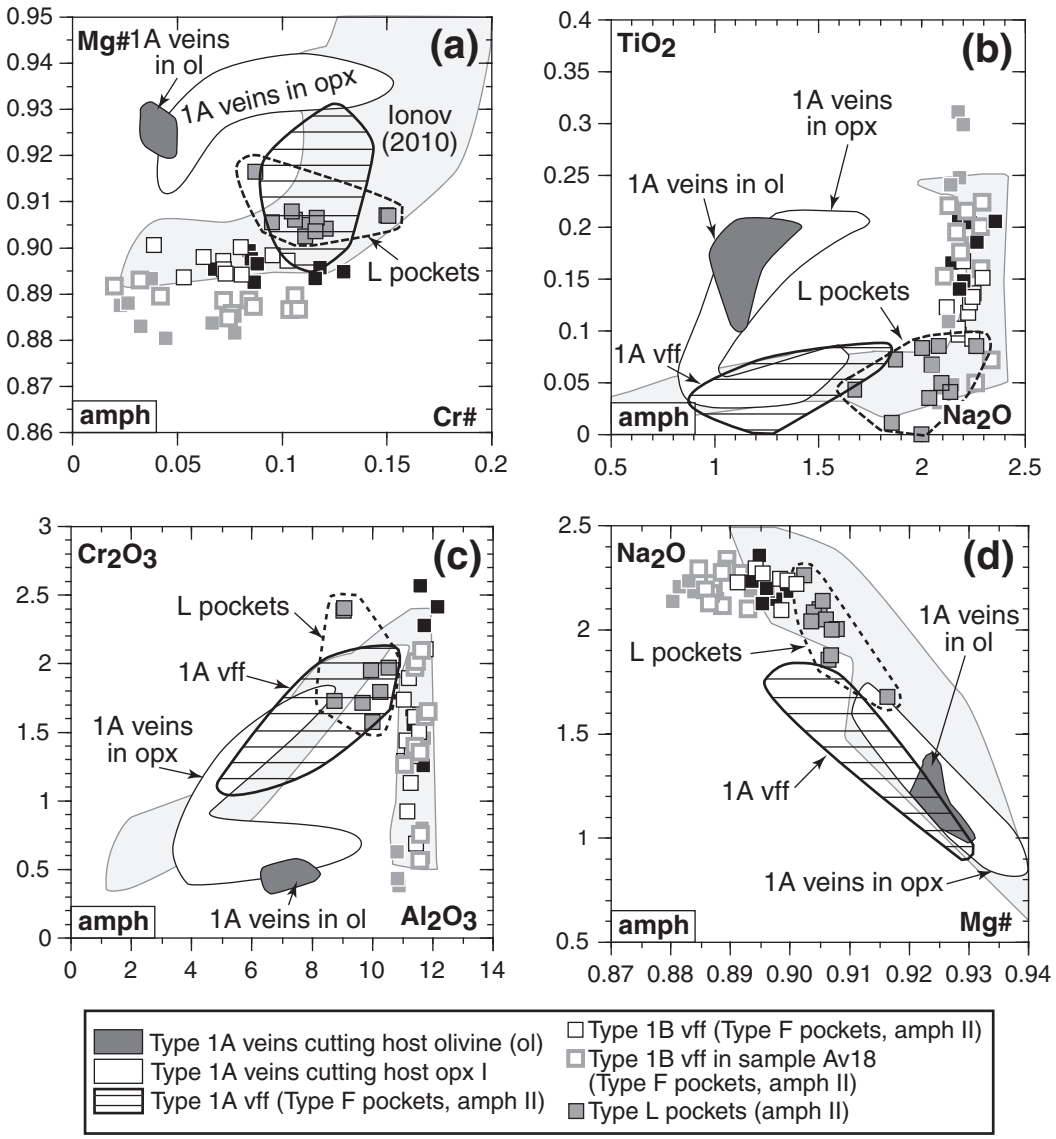

Fig. 11. Amphibole compositions in host-rocks and veins of mantle origin (Types 1A and 1B). (a–d) Covariation plots for amphibole from Type 1A veins, Type 1A veins in host opx (fine black outline field), and related veins filling fractures (amph II), Type 1B veins, thin veins and related veins filling fractures (amph II) and Type L pockets (amph II) compared with data for amphibole in Avacha harzburgites from Ionov (2010). Other fields and symbols are the same as in Figs 2–10. Very distinct compositional fields are observed for each amphibole type. The limited compositional variation for amphibole in Type 1A veins relative to the others should be noted, and that amphibole from Type 1B veins and related veins filling fractures (amph II) are the highest in Fe, Na and Al. (See Table 2 for representative analyses.)

lead to mineral assemblages evolving from almost anhydrous to hydrous (Pilet *et al.*, 2010). Pronounced positive Sr anomalies in Type 1B vein amphibole and cpx (Fig. 14d), together with negative Ti anomalies, are consistent with crystallization of Type 1B amphibole from residual liquids produced by massive fractionation of opx, which has negative Sr anomalies and positive Ti anomalies (Fig. 13). Thus, if the similar trace element patterns of opx in thick Type 1B and Type 1A veins (Fig. 13c and d) are consistent with similar origins of their initial melts, greater REE abundances in Type 1B cpx and amphibole than in Type 1A indicate that the residual liquid from which they crystallized was produced by advanced crystal fractionation (Fig. 14a and c). These distinctive chemical features of Type 1B thick veins are consistent with their textural differences from Type 1A veins and are most probably due to slower cooling and crystallization, with a greater amount of H_2O-rich residual liquid production during melt percolation that proceeds to lower temperatures.

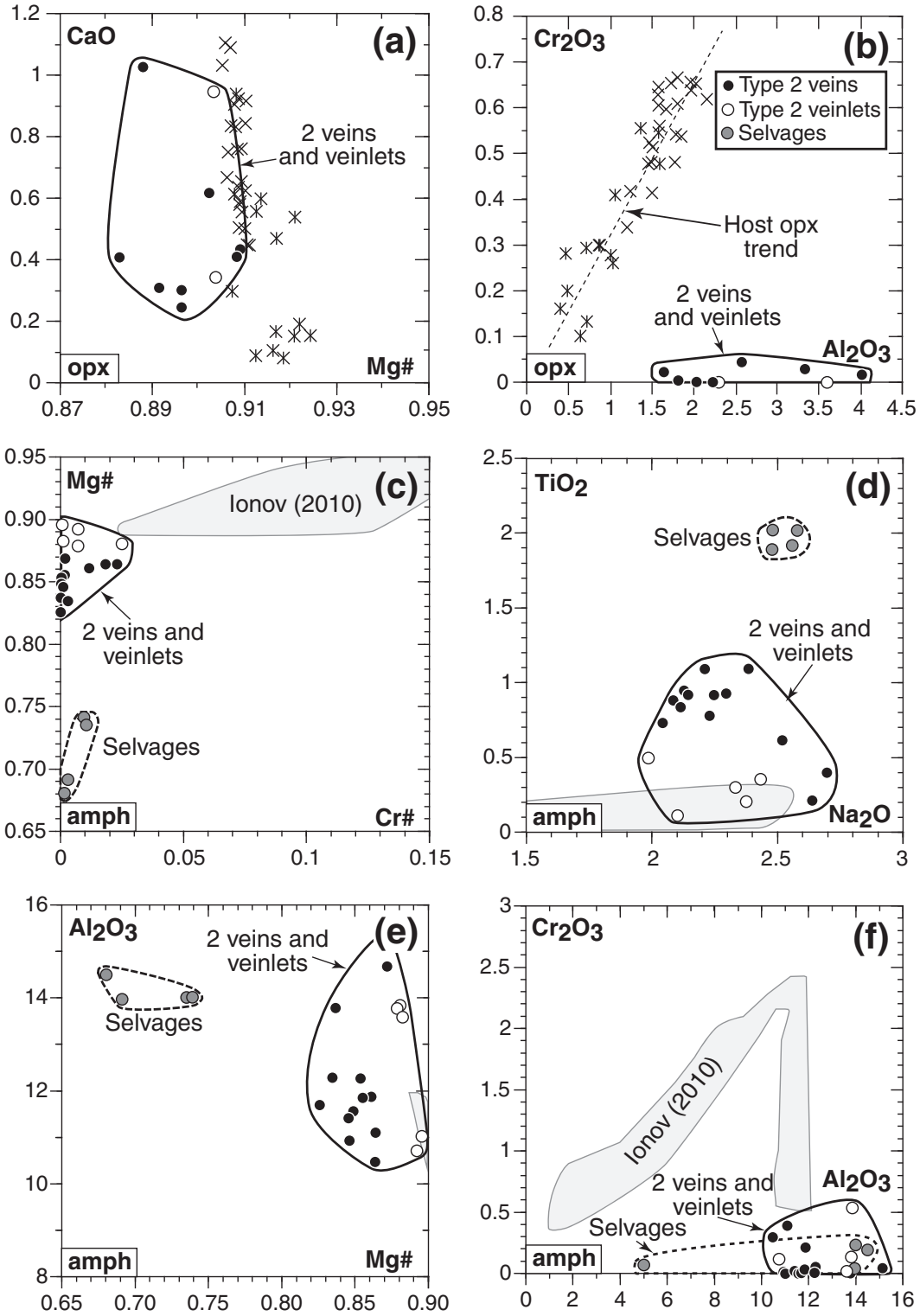

Fig. 12. Selvages and related veins (Type 2) mineral compositions. (a, b) Covariation plots for opx from selvages (dotted field), Type 2 veins and veinlets (black outline field), compared to opx I and II from host-rocks. (c–f) Covariation plots for amphibole from selvages and Type 2 veins and veinlets, compared with data for amphibole in Avacha harzburgites from Ionov (2010). Type 2 vein opx show Ca-zoning and low Cr contents mirroring those in Type 1A veins. Amphiboles in Type 2 veins and veinlets have the highest Fe and Ti content of this study. (See Table 3 for representative analyses.)

Table 4: Representative trace element abundances in orthopyroxene in host-rocks and Type 1 veins determined by LA-ICP-MS, as well as typical errors (1σ) and minimum detection limits for these analyses

	Host-rocks								Type 1 veins							Typical	Minimum
Sample:	Av18	Av18	Av20	Av20	Av19	Av19	Av20	Av20	Av20	Av20	Av19	Av18	Av18	Av9	Av9	errors	d.l.
Position:	core	rim	core	rim	core	rim	core	rim	core	rim	core	core	rim	core	rim	(1σ)	
	I	I	I/1A	I/1A	I/1B	I/1B	I/1B-vff	I/1B-vff	1A	1A	1B	1B	1B	t-1B	t-1B		
CaO	1·21	0·66	1·20	0·60	0·77	0·56	0·63	0·60	0·17	0·15	0·18	0·92	0·35	0·50	0·50	0·003	0·0007
TiO_2	0·010	0·008	0·009	0·011	0·009	0·008	0·008	0·009	0·013	0·014	0·009	0·022	0·005	0·004	0·006	0·0001	0·00003
V	120	83	102	102	101	73	101	93	105	100	64	74	23	61	68	0·160	0·005
Co	55	68	n.d.	n.d.	n.d.	n.d.	n.d.	n.d.	n.d.	n.d.	n.d.	60	169	56	70	1·33	0·009
Ni	580	872	n.d.	n.d.	n.d.	n.d.	n.d.	n.d.	n.d.	n.d.	n.d.	641	3101	622	982	6·65	0·07
Sr	b.d.	0·196	0·904	0·254	0·095	0·067	0·288	0·056	0·007	0·011	0·004	0·095	0·043	0·026	0·112	0·003	0·002
Y	0·093	0·077	0·161	0·318	0·107	0·120	0·085	0·125	0·044	0·077	0·072	0·193	0·079	0·026	0·050	0·002	0·0004
Zr	b.d.	0·102	0·294	0·046	0·019	0·088	0·011	0·055	0·149	0·024	0·055	0·220	0·136	0·499	0·864	0·001	0·002
Nb	b.d.	0·002	0·010	0·008	0·003	0·004	0·005	0·005	b.d.	0·001	0·002	0·004	0·008	0·004	b.d.	0·0004	0·0005
Ba	0·007	0·148	1·44	3·12	0·159	0·059	0·378	0·029	0·010	0·007	0·006	0·009	0·036	0·040	0·137	0·003	0·002
La	0·001	0·005	0·029	0·023	0·009	0·006	0·003	0·003	0·003	0·011	0·002	b.d.	0·003	0·001	0·006	0·0002	0·0002
Ce	b.d.	0·010	0·073	0·082	0·017	0·014	0·017	0·025	0·005	0·032	0·006	0·005	0·015	0·004	0·022	0·0002	0·0001
Pr	b.d.	b.d.	0·015	0·019	0·004	0·006	0·003	0·007	0·037	0·005	0·002	0·001	0·003	0·001	0·003	0·0001	0·00006
Nd	b.d.	0·012	0·029	0·106	0·010	0·018	0·009	0·014	0·004	0·023	0·022	0·006	0·005	0·005	0·023	0·0005	0·0002
Sm	b.d.	b.d.	0·008	0·038	b.d.	0·008	0·009	0·010	0·003	0·007	b.d.	0·007	0·010	0·006	0·006	0·0006	0·001
Eu	b.d.	b.d.	0·005	0·009	b.d.	0·002	0·003	0·002	0·001	0·003	0·002	0·002	0·002	b.d.	b.d.	0·0001	0·0002
Gd	b.d.	0·008	0·014	0·038	0·002	0·009	0·002	0·010	b.d.	0·008	0·008	0·007	0·012	b.d.	0·005	0·0004	0·0005
Tb	b.d.	0·002	0·004	0·008	0·001	0·002	0·001	0·002	b.d.	0·002	0·001	0·002	0·002	0·001	b.d.	0·00008	0·00009
Dy	0·006	0·009	0·021	0·055	0·007	0·023	0·006	0·014	0·004	0·014	0·011	0·021	0·014	0·001	0·009	0·0005	0·0003
Ho	0·004	0·005	0·006	0·014	0·003	0·004	0·004	0·006	0·001	0·004	0·003	0·009	0·003	b.d.	0·003	0·0001	0·00005
Er	0·020	0·016	0·027	0·053	0·022	0·019	0·021	0·024	0·008	0·014	0·014	0·026	0·011	0·004	0·011	0·001	0·0002
Tm	0·006	0·005	0·007	0·009	0·006	0·008	0·006	0·006	0·002	0·003	0·004	0·009	0·003	0·002	0·003	0·0003	0·0001
Yb	0·064	0·054	0·071	0·099	0·078	0·051	0·074	0·057	0·013	0·023	0·029	0·076	0·021	0·024	0·041	0·002	0·0004
Lu	0·014	0·007	0·015	0·018	0·014	0·009	0·015	0·015	0·003	0·005	0·007	0·012	0·007	0·006	0·009	0·0004	0·00006
Hf	b.d.	b.d.	0·003	0·002	b.d.	0·001	b.d.	0·005	0·001	b.d.	0·002	0·008	0·006	0·016	0·018	0·0003	0·0005
Ta	b.d.	b.d.	0·001	0·002	0·001	b.d.	b.d.	0·001	b.d.	0·001	b.d.	b.d.	0·003	b.d.	b.d.	0·0001	0·0002
Pb	0·005	0·017	0·121	0·044	0·035	0·027	0·055	0·035	0·013	0·032	0·056	0·011	0·009	0·006	0·016	0·002	0·0007
Th	b.d.	0·003	0·019	0·005	0·001	0·002	0·0003	0·010	0·014	0·096	0·047	0·0002	0·001	0·004	0·033	0·0001	0·00006
U	b.d.	0·007	0·022	0·007	0·007	0·008	0·005	0·005	0·005	0·050	0·013	b.d.	b.d.	b.d.	0·002	0·0001	0·00004

All values are in ppm (except for CaO and TiO_2, wt %). d.l., detection limits; b.d., below detection limit; n.d., no data; I/1A, first generation ('I') host mineral cut by a Type 1A vein; I/1B, first generation ('I') host mineral cut by a Type 1B vein; I/1B-vff, first generation ('I') host mineral cut by Type 1B veins filling fractures. All other Abbreviations are the same as in Table 2.

Reactive melt percolation

Assimilation and re-equilibration reactions with the host-rock phases played a significant role in the origin of Type 1B veins, unlike for Type 1A veins. Clinopyroxene in the reaction zones of thick 1B veins has U-shaped REE patterns with positive Zr–Hf spikes, with much lower MREE than in cpx from the vein centres (Fig. 14a). REE patterns of opx, cpx and amphibole from thin Type 1B veins and related Type L pockets are also U-shaped and have even lower MREE anomalies with marked positive Zr–Hf spikes (Figs 13e and 14a, c). This systematic chemical evolution of mineral trace element compositions from the central parts of the reactive 1B veins across their contacts to the vein-related metasomatic minerals in the host peridotites is one of the most remarkable findings in this study. We envisage that residual Si- and volatile-rich melts formed in thick Type 1B veins were expelled to the host-rocks through fractures, cracks and possibly grain boundaries at the outer

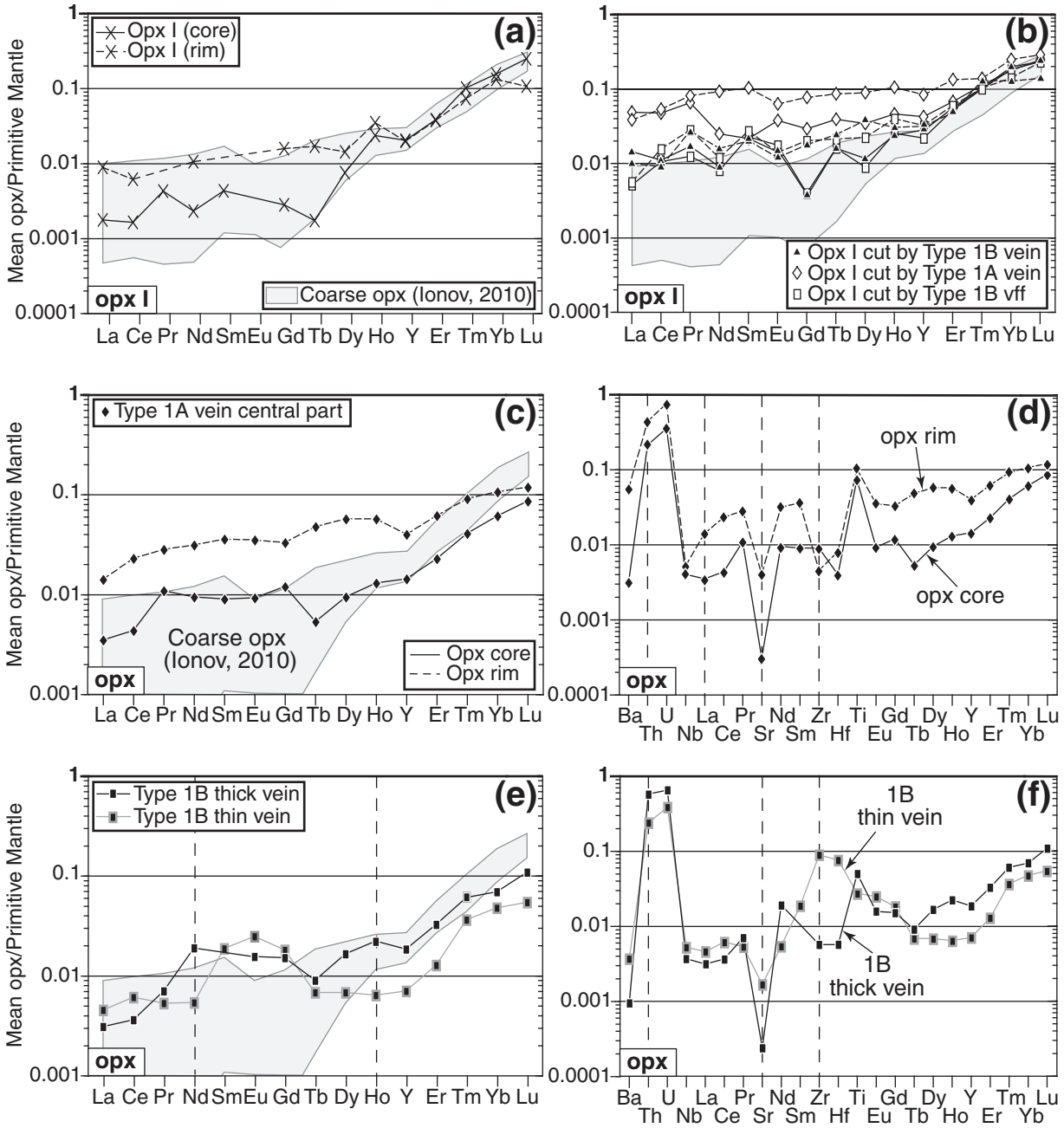

Fig. 13. Primitive mantle-normalized (McDonough & Sun, 1995) trace element abundances in opx from host-rocks (opx I) and veins of mantle origin (Types 1A and 1B). (a, b, c, e) REE plus Y patterns of averaged analyses of opx compared with data for opx in Avacha harzburgites from Ionov (2010) (light grey outline field) and (d, f) extended trace element patterns for mean analyses of opx. (a) Host-rock opx I. (b) Host-rock opx I cut by veins and veins filling fractures, (c, d) opx from Type 1A veins and (e, f) opx from Type 1B thick and thin veins. Noteworthy features are the LREE–MREE enrichment in host-rock opx I cut by veins, the strong REE zoning in opx from Type 1A veins and the Zr–Hf spikes in opx from Type 1B thin veins. In this diagram and the following ones reporting trace element data, typical errors calculated by propagating those derived from LA-ICP-MS analyses (1σ) on averaging are covered by the symbol size. (See Table 4 for representative analyses, their typical errors and minimum detection limits, and SD Fig. 1 for LA-ICP-MS review of zoned opx in Type 1A veins.)

limits of the percolation front (i.e. reaction zone) to produce thin Type 1B veins and disseminated Type L melt pockets.

In the following sub-section we discuss the evidence for assimilation and other re-equilibration reactions and their respective controls on the distinctive REE_N patterns of Type 1B thin veins and Type L melt pockets.

The irregular margins of thick Type 1B veins enclose anhedral olivine and spinel in reaction zones (Fig. 6c) that

Table 5: Representative trace element abundances in clinopyroxene (cpx) in host-rocks and Type 1 veins determined by LA-ICP-MS

	Host-rocks			Type 1 veins				
Sample:	Av18	Av18	Av9	Av20	Av20	Av18	Av18	Av9
Position:	core	core	core	core	core	rim	core	core
	I	1B-vff	L	1A	1A-rz	1B	1B-rz	t-1B
TiO_2	0·017	0·014	0·019	0·019	0·015	0·060	0·065	0·009
V	190	164	251	145	197	263	274	153
Co	n.d.	22	47	n.d.	n.d.	100	113	29
Ni	n.d.	548	998	n.d.	n.d.	2335	2728	520
Sr	11	7·07	34	3·74	4·99	27	25	20
Y	0·671	0·393	0·546	0·809	0·826	1·94	1·62	0·378
Zr	0·419	0·159	5·97	0·607	0·245	3·880	6·92	4·74
Nb	0·004	b.d.	0·063	b.d.	0·013	0·016	0·050	0·002
Ba	1·22	b.d.	11	0·073	4·36	3·93	6·40	0·014
La	0·096	0·042	0·612	0·025	0·093	0·234	0·321	0·416
Ce	0·238	0·099	1·58	0·308	0·308	0·823	1·05	1·13
Pr	0·037	0·0144	0·189	0·026	0·031	0·138	0·153	0·151
Nd	0·163	0·071	0·572	0·141	0·118	0·751	0·718	0·456
Sm	0·063	0·038	0·076	0·062	0·026	0·280	0·159	0·048
Eu	0·019	0·008	0·030	0·024	0·022	0·097	0·062	0·017
Gd	0·033	0·017	0·040	0·077	0·044	0·272	0·195	0·025
Tb	0·011	0·005	0·007	0·023	0·011	0·043	0·027	0·005
Dy	0·081	0·054	0·059	0·140	0·111	0·332	0·244	0·040
Ho	0·020	0·017	0·022	0·037	0·029	0·075	0·061	0·012
Er	0·105	0·062	0·105	0·103	0·098	0·222	0·227	0·068
Tm	0·023	0·013	0·026	0·034	0·024	0·040	0·039	0·016
Yb	0·178	0·142	0·248	0·182	0·193	0·279	0·286	0·128
Lu	0·037	0·020	0·052	0·041	0·032	0·054	0·052	0·031
Hf	0·005	0·005	0·155	0·034	0·017	0·137	0·220	0·148
Ta	b.d.	b.d.	0·003	0·009	0·002	b.d.	b.d.	b.d.
Pb	0·109	0·109	0·164	0·139	0·135	0·128	0·089	0·114
Th	0·009	0·003	0·015	0·029	0·038	0·016	0·028	0·007
U	0·008	0·004	b.d.	0·180	0·030	0·006	0·039	b.d.

All values are in ppm (except for TiO_2, wt %). b.d., below detection limit; n.d., no data; 1B-rz, mineral in Type 1B vein reaction zone. All other Abbreviations are the same as in Table 2.

Table 6: Representative trace element abundances in amphibole in host-rocks and Type 1 veins determined by LA-ICP-MS

	Host-rocks			Type 1 veins			
Sample:	Av18	Av18	Av9	Av20	Av20	Av20	Av18
Position:	core	core	core	core	core	core	core
	I	1B-vff	L	1A	1A	1A-rz	1B
TiO_2	0·169	0·104	0·050	0·154	0·133	0·164	0·208
V	545	434	486	361	323	395	386
Co	43	51	67	46	43	n.d.	44
Ni	1299	1631	1624	568	598	n.d.	1760
Sr	79	114	61	20	17	22	116
Y	3·07	2·66	0·86	2·72	2·60	3·83	4·92
Zr	7·09	8·51	16	1·09	0·96	1·31	16
Nb	0·274	0·393	0·335	0·242	0·225	0·330	0·459
Ba	20	38	52	65	48	118	35
La	0·494	0·779	1·25	0·586	0·502	0·899	0·895
Ce	1·88	2·49	3·16	1·96	1·74	3·09	3·20
Pr	0·358	0·396	0·381	0·290	0·264	0·478	0·553
Nd	1·87	1·73	1·18	1·31	1·17	2·03	2·81
Sm	0·524	0·361	0·149	0·323	0·315	0·588	0·792
Eu	0·229	0·131	0·050	0·192	0·155	0·267	0·296
Gd	0·510	0·282	0·068	0·290	0·260	0·563	0·805
Tb	0·071	0·053	0·0119	0·054	0·058	0·109	0·131
Dy	0·504	0·401	0·087	0·457	0·422	0·831	0·898
Ho	0·116	0·089	0·029	0·104	0·095	0·182	0·196
Er	0·410	0·322	0·146	0·313	0·304	0·532	0·580
Tm	0·068	0·053	0·033	0·058	0·052	0·086	0·092
Yb	0·523	0·457	0·314	0·495	0·426	0·684	0·667
Lu	0·076	0·091	0·063	0·076	0·063	0·098	0·102
Hf	0·246	0·241	0·413	0·052	0·050	0·084	0·611
Ta	0·020	0·016	0·030	0·007	0·006	0·012	0·027
Pb	0·153	0·192	0·284	0·128	0·127	0·330	0·195
Th	0·014	0·011	0·057	0·050	0·075	0·087	0·015
U	0·002	0·005	0·006	0·035	0·037	0·091	0·014

All values are in ppm (except for TiO_2, wt %). n.d., no data. All abbreviations are the same as in Table 2.

are host-rock relics partly assimilated by the melt during percolation. The assimilation rate by a dissolution–precipitation reaction depends on under-saturation of the melt in host-rock components (e.g. olivine in the case of the Avacha peridotite), as well as on the temperature of the melt and its host-rocks, and may be assisted by the build-up of volatile components in the residual melts (Bédard, 1989; Vasseur *et al.*, 1991; Van Den Bleeken *et al.*, 2010). Liquidus phase relationships up to 3 GPa (e.g. Milholland & Presnall, 1998) show that Cr-spinel and olivine are out of equilibrium with SiO_2-rich melts, similar to the initial melt inferred for Type 1A and thick Type 1B veins (see above). In this context, higher Cr in opx and amphibole in Type 1B veins than in Type 1A veins (Figs 9b, 10a and 11c) may be linked to reaction with host Cr-spinel (Fig. 6c). The large Mg# variation range in the Type 1B vein minerals (Figs 8a, 9a, 11a, d and SD Fig. 4) can be due to a greater degree of fractionation of the percolating melt and/or to different degrees of reaction with the host (e.g. olivine and Cr-spinel assimilation).

Olivine and spinel assimilation may have a diluting effect for elements such as the MREE–HREE in the

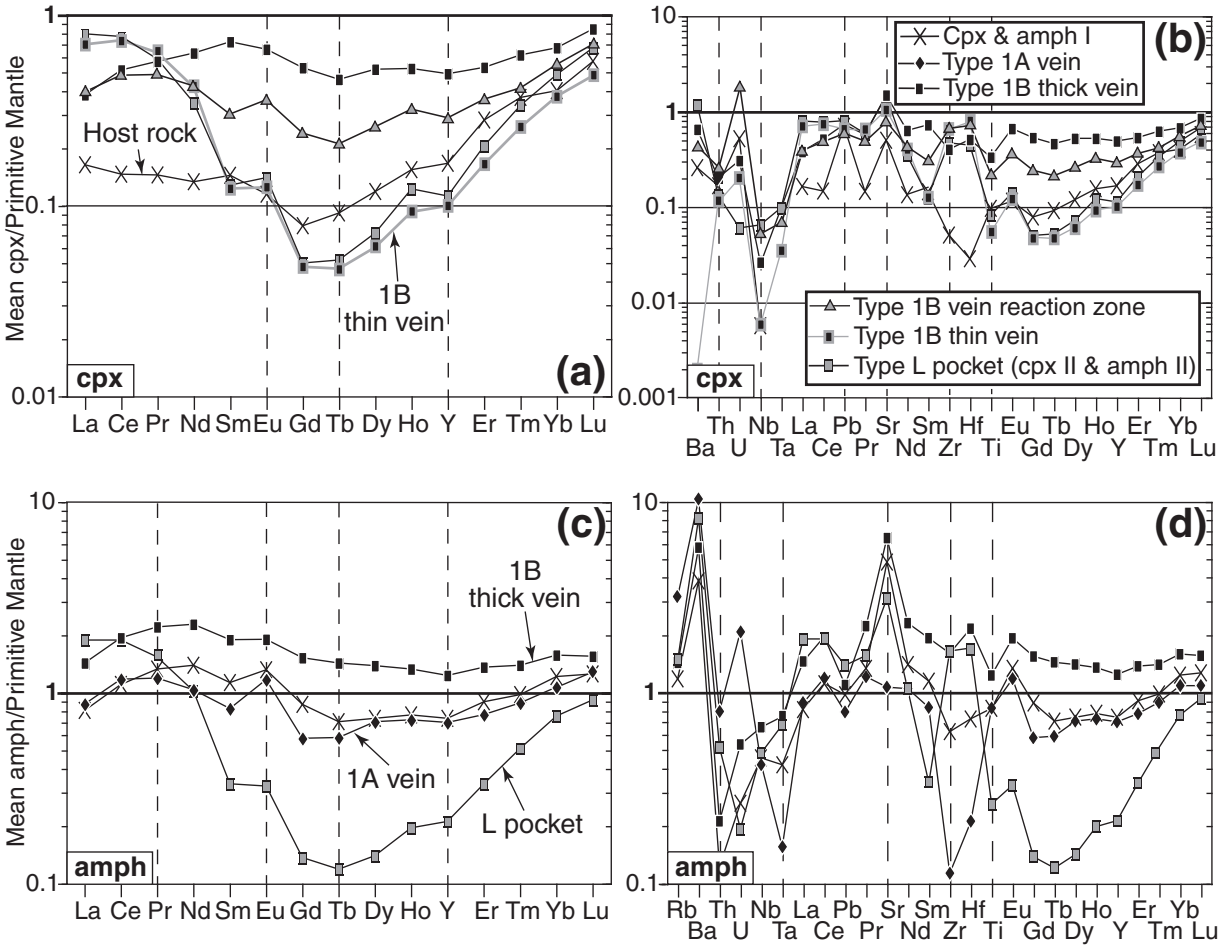

Fig. 14. Primitive mantle-normalized (McDonough & Sun, 1995) trace element abundances in cpx and amphibole from host-rocks and veins of mantle origin (Types 1A and 1B). (a) REE plus Y patterns and (b) extended patterns of mean analyses of cpx. (c) REE plus Y and (d) extended patterns of mean analyses of amphibole. REE and Sr abundances are higher in amphibole from Type 1B thick veins than those in Type 1A veins. It should be noted that the REE patterns in Types 1A and 1B thick vein minerals are nearly flat, whereas those in Type 1B thin veins and Type L pockets (cpx II and amph II) have U-shaped REE patterns with positive Zr–Hf spikes. (See Tables 5 and 6 for representative analyses.)

reacted silicic melt, but the observed large magnitude of the MREE depletion in the reaction end-products (thin Type 1B veins and Type L pockets, Fig. 14a and c) would require unreasonably high proportions of assimilated material. Furthermore, host olivine and spinel assimilation may not produce positive Zr–Hf spikes in the reacted melt, as these two elements, similar to the MREE, are very low (below LA-ICP-MS detection limits) in olivine and spinel from the Avacha harzburgites (Ionov, 2010). Therefore, a combination of assimilation and continuous re-equilibration of the melt with the host minerals is a more likely explanation for the observed variations of lithophile trace elements abundances.

We propose that the Si- and volatile-rich residual melts expelled from thick Type 1B veins first exchanged by diffusion with the olivine–opx peridotite matrix ('diffusive flux'; McPherson *et al.*, 1996) and, second, brought about partial fluid-assisted dissolution of host olivine, opx I and spinel I (and possibly cpx I, Fig. 4a), followed by precipitation of opx and amphibole to form the veins according to reaction (1) or (2):

$$\text{olivine} + (\text{Mg, Si, H}_2\text{O})\text{-rich melt I} \Rightarrow \text{opx} + \text{melt II} \quad (1)$$

$$\text{olivine} + \text{spinel I} + \text{opx I} \pm \text{cpx I} + (\text{Mg, Si, H}_2\text{O})\text{-rich melt I} \Rightarrow \text{opx} + \text{amphibole} + \text{melt II}. \quad (2)$$

The relative role of reactions (1) and (2) depends on the mineral assemblage in the host. Reaction (1) has been reported for various mantle xenoliths suites (e.g. Kelemen *et al.*, 1998), whereas reaction (2) is similar to that observed in melt–peridotite interaction experiments (e.g. Sen & Dunn, 1994). If the MREE–HREE depletion can be explained by host-buffering, the high LREE abundances that are maintained in the reaction zones (Fig. 14a) must result from the continuing ingress of the residual

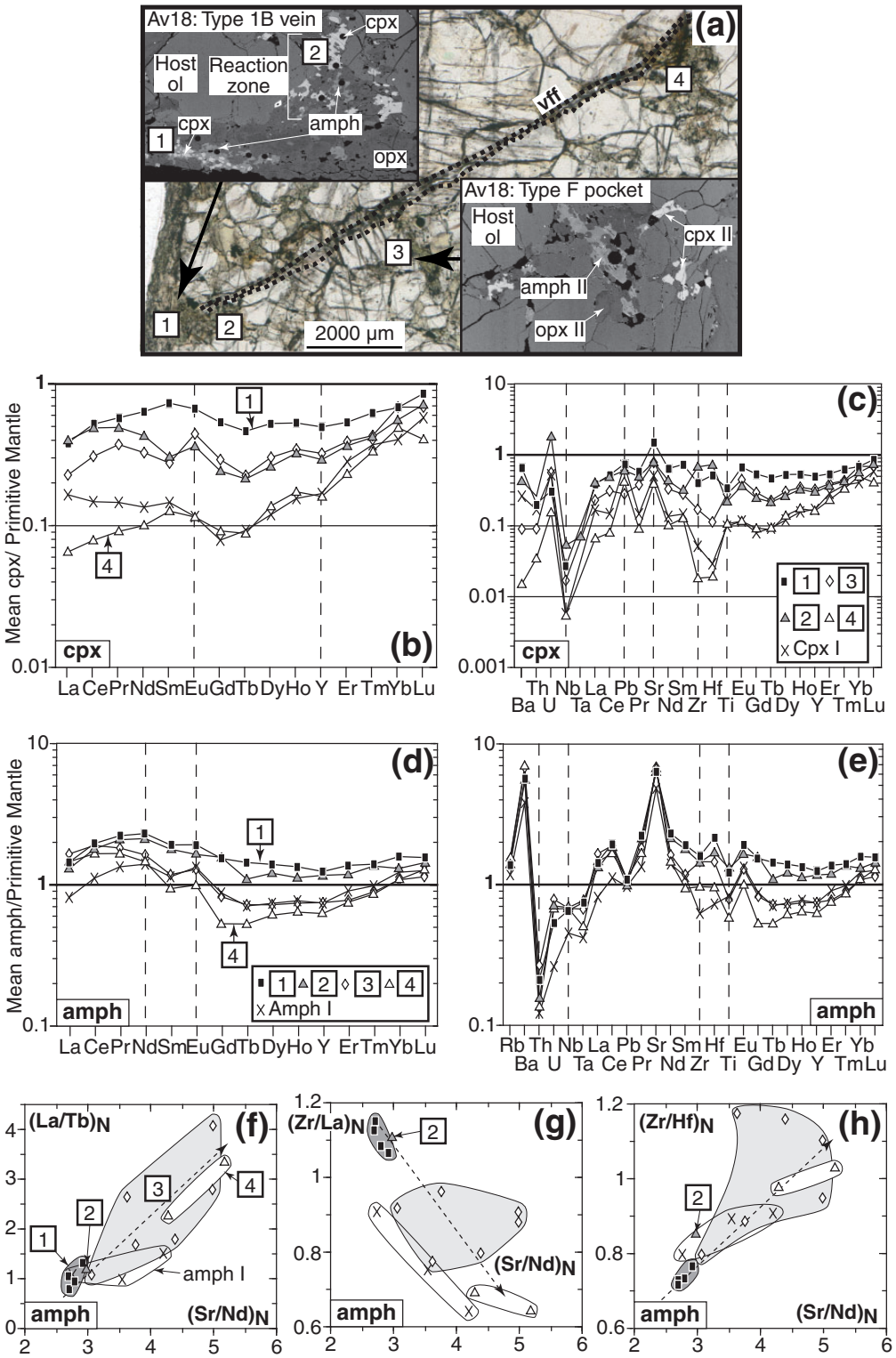

Fig. 15. Trace element abundances in cpx II and amph II from metasomatic pockets (Type F) along fractures filled by material (veins filling fractures) deriving from veins of mantle origin (Type 1B). (a) Photomicrograph in transmitted light of a 120 μm thick polished section of an Avacha harzburgite xenolith (sample Av18) cut by a vein of mantle origin (Type 1B) and a related filled fracture. PM-normalized (McDonough & Sun, 1995) (b) REE plus Y and (c) extended trace element patterns of mean analyses of cpx II in metasomatic Type F pockets along Type 1B veins filling a fracture in sample Av18. (d) REE plus Y and (e) extended patterns of mean analyses of amph II in metasomatic Type F pockets along Type 1B veins filling a fracture in sample Av18. (f–h) Trace element ratio covariation plots for amphibole from the Type 1B vein to the related Type F metasomatic pockets. The LREE–HFSE depletion in cpx II and the MREE–Zr–Hf depletion in amph II in metasomatic pockets from the Type 1B vein towards the host-rock should be noted. (See Tables 5 and 6 for representative analyses.)

Table 7: Representative trace element abundances in selvages and Type 2 vein minerals and glass determined by LA-ICP-MS

Sample:	Av18	Av19	Av18	AV19	Av18	AV19	Av27	Av27	Av27	Av27	Av27	Av27
Phase:	cpx	cpx	amph	amph	glass	glass	opx	opx	amph	amph	amph	amph
Position:	core	core	core	core	n.d.	n.d.	core	rim	core	core	core	core
	selv	selv	selv	selv	selv	selv	2	2	2	2′	2′	2′
CaO	n.d.	n.d.	n.d.	n.d.	n.d.	n.d.	0·52	0·72	n.d.	n.d.	n.d.	n.d.
TiO_2	0·423	0·010	1·49	2·12	n.d.	n.d.	0·566	1·02	0·933	0·505	0·233	0·541
V	263	336	536	683	160	149	488	405	119	128	80	98
Co	n.d.	n.d.	n.d.	n.d.	n.d.	n.d.	n.d.	n.d.	53	n.d.	n.d.	n.d.
Ni	n.d.	n.d.	n.d.	n.d.	29	12	n.d.	n.d.	1813	n.d.	n.d.	n.d.
Sr	19	19	113	169	455	448	12	41	75	255	115	124
Y	7·84	11	11	17	12	12	11	38	70	14	9	12
Zr	4·83	10	7·66	9·36	83	77	36	74	38	121	163	111
Nb	0·008	b.d.	0·103	0·152	1·25	1·08	0·200	0·447	0·749	3·01	2·09	1·61
Ba	0·02	0·026	26	39	288	280	18	23	11	92	33	48
La	0·181	0·266	0·051	0·254	6·54	6·24	0·618	1·64	1·69	6·44	6·56	4·45
Ce	0·87	1·52	1·22	1·54	15	15	4·21	6·18	11	16	24	17
Pr	0·261	0·381	0·373	0·433	1·98	1·97	0·469	1·38	2·84	2·13	3·25	2·96
Nd	1·81	2·82	2·39	3·31	9·25	8·34	2·41	9·26	21	9·04	11	14
Sm	0·925	1·49	1·24	1·81	2·09	2·76	0·654	3·24	8·85	2·14	1·92	2·91
Eu	0·358	0·444	0·504	0·725	0·687	0·540	0·369	1·20	2·69	0·739	0·736	0·902
Gd	1·36	2·10	1·96	2·93	1·97	1·41	0·808	4·01	11	1·84	1·51	2·11
Tb	0·250	0·369	0·326	0·516	0·328	0·270	0·194	0·814	1·78	0·317	0·222	0·316
Dy	1·74	2·50	2·37	3·48	2·31	2·69	1·45	6·03	13	2·25	1·47	1·84
Ho	0·345	0·478	0·480	0·769	0·433	0·394	0·353	1·40	2·65	0·454	0·339	0·360
Er	0·929	1·29	1·29	1·90	1·33	1·83	1·35	4·82	8·02	1·62	0·962	1·05
Tm	0·118	0·197	0·166	0·279	0·179	0·172	0·310	0·911	1·20	0·306	0·164	0·156
Yb	0·739	1·03	1·01	1·48	1·38	1·23	3·20	7·52	8·48	2·00	1·27	1·17
Lu	0·101	0·149	0·132	0·196	0·124	0·295	0·628	1·28	1·20	0·369	0·272	0·189
Hf	0·329	0·681	0·460	0·517	1·94	1·73	1·26	3·54	2·11	2·95	3·62	3·43
Ta	0·007	0·002	0·007	0·015	0·181	0·110	0·028	0·064	0·056	0·241	0·156	0·121
Pb	0·057	0·091	0·202	0·287	n.d.	n.d.	1·46	0·829	0·270	0·962	0·576	0·670
Th	0·059	0·004	0·007	0·051	0·937	1·01	0·235	0·453	0·014	0·542	0·202	0·127
U	0·016	0·001	0·015	0·053	0·470	0·360	0·162	0·427	b.d.	0·238	0·050	0·104

All values are in ppm (except for CaO and TiO_2, wt %). b.d., below detection limit; n.d., no data. All abbreviations are the same as in Table 3.

volatile-rich melt at the percolation front ('advective chemical flux'; McPherson *et al.*, 1996).

A similar record of melt–rock interaction processes in Type 2 veinlets

Comparison of data for Type 1 and Type 2 veins suggests that melts with significantly different initial trace element signatures can follow very similar fractionation trends, probably controlled by the same reaction processes with the host peridotites. The petrographic evidence for a link between the rapidly crystallized Type 2 veins and reactive Type 2 veinlets strongly supports our melt–rock interaction model (Fig. 17b and SD Fig. 3).

We argue, based on textural (Fig. 7c) and chemical evidence, that Type 2 veinlets formed through reaction of an andesitic magma originating from the host selvages with olivine, opx I and spinel I (and possibly cpx I) in the harzburgites to produce amphibole and opx according to reaction (3) or (4):

$$\text{olivine} + (\text{Ca, Si, } H_2O)\text{-rich melt I} \Rightarrow \text{opx} + \text{amphibole} + \text{melt II} \quad (3)$$

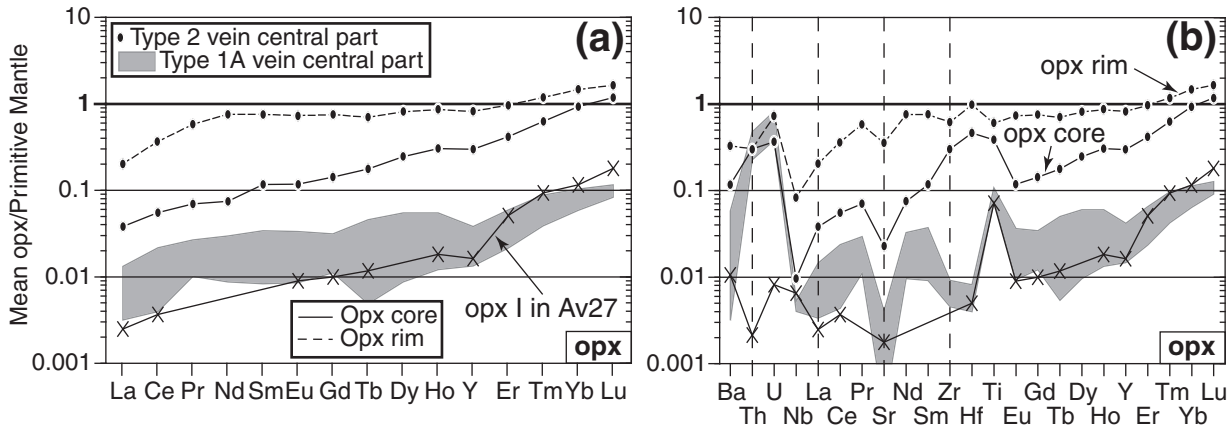

Fig. 16. Primitive mantle-normalized (McDonough & Sun, 1995) (a) REE plus Y patterns and (b) extended trace element patterns for mean analyses of opx in veins related to host selvages (Type 2). REE are nearly 10 times enriched in the core of opx in Type 2 veins than in typical opx I and in the core of opx in Type 1A veins. Mirroring those in Type 1A veins, opx in Type 2 veins show a strong LREE–MREE zoning but much less for HREE and Zr–Hf. (See Table 7 for representative analyses and SD Fig. 1 for LA-ICP-MS signal review of zoned opx in Type 2 veins.)

$$\text{olivine} + \text{spinel I} + \text{opx I} \pm \text{cpx I} + (\text{Ca, Si, H}_2\text{O}) - \text{rich melt I} \Rightarrow \text{opx} + \text{amphibole} + \text{melt II}. \quad (4)$$

Amphiboles in Type 2 veinlets have slightly U-shaped REE patterns, with LREE and HFSE abundances similar to or a little higher than for amphiboles in Type 2 veins (Fig. 17d). We conclude that a process similar to that proposed for Type 1B veins; that is, a combination of fractionation and diffusive re-equilibration with (and partial assimilation of) the host-rock, took place during the formation of Type 2 veinlets. The broad MREE–HREE variation range in adjacent (sub-millimetre scale) amphibole grains in Type 2 veinlets (Fig. 17f) suggests that the inferred melt–rock interaction depends on the local availability of reacted volatile-rich melt and on the local permeabilty of the host-rock. This agrees well with our hypothesis of a diffusive flux process triggered by the ingress of a volatile-rich melt and leading finally to partial dissolution and assimilation of minerals from the host.

In summary, thin Type 1B veins, Type L pockets and Type 2 veinlets appear to be the end-products of a multistage melt–host interaction process characterized by (1) strong fractionation of the initial melt, (2) re-equilibration of the melt with the host and its fluid-assisted assimilation at percolation fronts, (3) injection of residual, H_2O- and Si-rich liquids into the host and (4) continuous re-equilibration of the ejected liquids with the host-rocks (and their partial assimilation) as they percolate and crystallize as thin Type 1B veins or Type 2 veinlets. This process also contributes to the formation of amph II and cpx II disseminated in Type L pockets in the host peridotites. Importantly, the fractionation–reactive percolation of liquids with distinct initial compositions ultimately produces similar inter-element fractionations.

Numerical modelling of REE and Zr–Hf behaviour during reactive melt percolation in harzburgites

To test if the processes we describe in the previous section can produce the trace element signatures observed in the crystallization products of reacted melts (thin Type 1B veins, Type L pockets and Type 2 veinlets), we performed numerical simulation of REE and Zr–Hf distribution during reactive percolation of H_2O- and Si-rich liquids injected into the Avacha harzburgites, inferred above for Type 1 and Type 2 veins. For this purpose, we used the 'plate model' trace element numerical simulation developed by Vernières *et al.* (1997) to reproduce matrix–melt reactions through mineral dissolution and/or precipitation and diffusive re-equilibration with adjustable modal composition.

The principles of the plate model are illustrated in Fig. 19a. We used reactants and products from reactions (1)–(4) in the models to account for dissolution–precipitation of minerals. The plate model assumes instantaneous melt equilibration as it moves from one matrix cell to another. The formation of vein minerals is accounted for in the plate model to simulate the continuous fractionation of the percolating melt. We model a decrease of melt/rock ratios from high values near the melt source (from the vein centre to the reaction front, Fig. 19a) to zero far from the melt source in the host peridotite. Because of this, the modal proportions in the model evolve from that of the vein in the first matrix cells (0–20) to that of the initial peridotite host in the last cells (up to 45).

We used an initial peridotite composition (matrix) that is close in mineral proportions and trace element abundances to sample Av11 from Ionov (2010), representative of the refractory and depleted nature of the mantle lithosphere beneath Avacha. We used the trace element

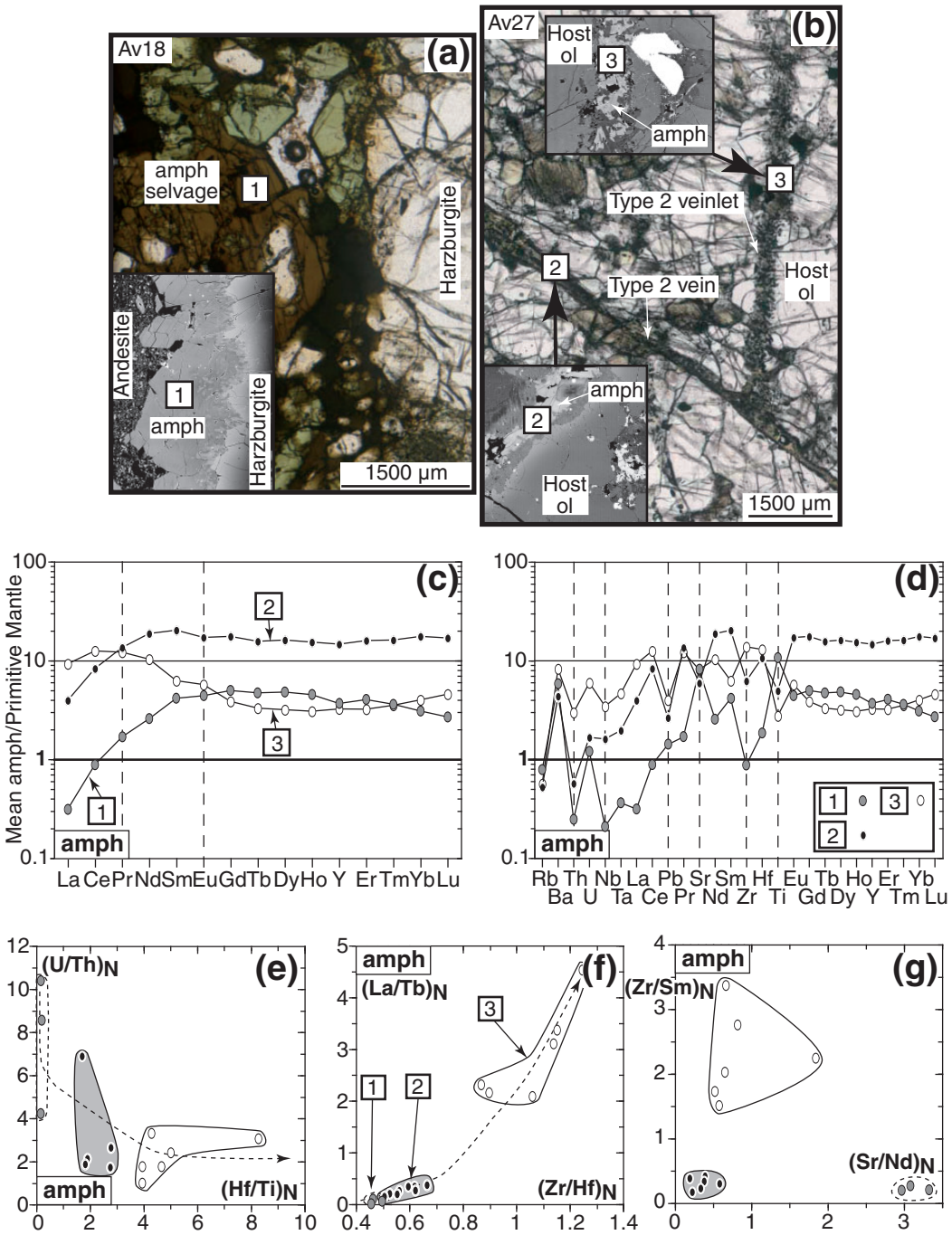

Fig. 17. Trace element abundances in amphibole from selvages and related veins and veinlets (Type 2). Photomicrographs in transmitted light of thick polished section (120 μm) of (a) an Avacha harzburgite xenolith (sample Av18) coated by a millimetre-thick amphibole selvage and (b) an Avacha harzburgite xenolith (sample Av27) cut by Type 2 veins and related veinlets of selvage origin. PM-normalized (McDonough & Sun, 1995) (c) REE plus Y patterns and (d) extended patterns for mean amphibole in selvages and related Type 2 veins and veinlets. (e–g) Trace element ratio covariation plots for amphibole in selvages and related Type 2 veins and veinlets. The U-shaped REE patterns with positive Zr–Hf spikes in Type 2 veinlets should be noted. (See Table 7 for representative analyses.)

abundances in the parental melt produced at 1300°C after Bénard & Ionov (2012) and in the selvage glass, respectively, for Type 1 and Type 2 initial melts (Fig. 18). Constant assimilation rates for host-rock olivine were generally assumed; assimilation of spinel I and cpx I was neglected in most calculations because of their low (<1%) modal abundances in Avacha harzburgites (Ionov, 2010). Modelling parameters and initial melts and matrix compositions

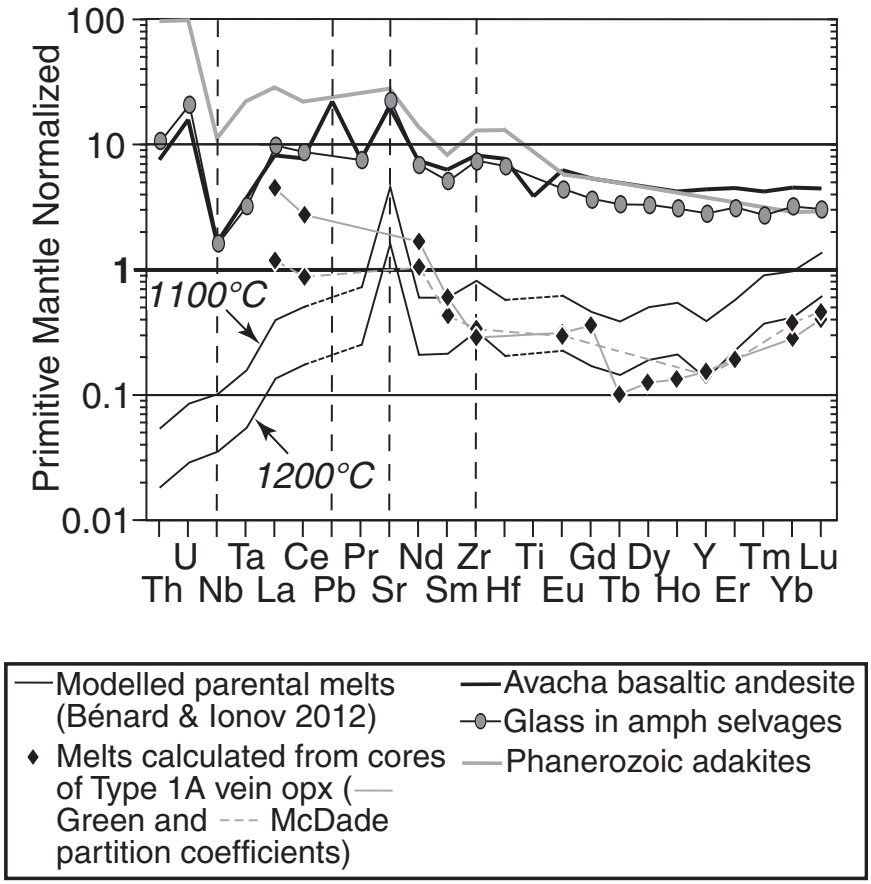

Fig. 18. Primitive mantle-normalized (McDonough & Sun, 1995) extended trace element patterns of theoretical equilibrium liquids calculated from the trace element compositions of cores of opx in Type 1A veins. Partition coefficients used for opx–melt equilibrium are from McDade *et al.* (2003) and run 1802 of Green *et al.* (2000). Calculated liquids are compared with the modelled parental melts formed at 1200°C and 1100°C for Type 1A and thick Type 1B veins from Bénard & Ionov (2012). It should be noted that there is good agreement for HREE–MREE between the modelled parental melt formed at 1200°C from Bénard & Ionov (2012) and our calculations, whereas LREE are not consistent between the two (see text for details). Also shown in this diagram are liquids of interest for the Type 2 vein system, which include representative trace element patterns of Phanerozoic adakites (Condie, 2005), Avacha basaltic andesite (Ishimaru *et al.*, 2007) and the glass in the amphibole selvages in this study. (See Table 7 for representative analyses.)

are given in Table 8. All modelling results are provided in SD Table 2 (Type 1 vein models) and SD Table 3 (Type 2 vein models). They show, in particular, that adjusting the assimilation rate has negligible effects on the modelled trace element patterns of the reaction end-products.

We cannot directly incorporate any major element or thermodynamic data in the plate model and reaction (2) cannot account for the variable olivine and cpx amounts observed in Type 1 veins or at their reactions fronts (Fig. 6b–d). Instead, our observations and the thermodynamic modelling of Bénard & Ionov (2012) suggest that only the Type 1 liquid line of descent [i.e. the degree of evolution of the reacting melt I in reactions (1) and (2)] controls olivine and cpx saturation in the vein. Therefore, we tested different assimilation rates and proportions of vein-forming minerals [reaction products in reactions (1) and (2)] to simulate separately the effects of different degrees of evolution of the percolating melts at the time of their intrusion.

The results for typical models for Type 1 vein initial melt are presented in Fig. 19b–g. Three vein-forming mineral assemblages are modelled (from olivine- to cpx-bearing), respectively in Fig. 19b–c, d–e and f–g, to compare three melt evolution stages consistent with our observations and the thermodynamic model of Bénard & Ionov (2012). The plate modelling for Type 1 vein initial melt produces strongly LREE-enriched, U-shaped REE patterns in the vein to the reaction front (cells 1–20) if opx and olivine precipitate (Fig. 19b and c). Decreasing olivine and increasing cpx fractions in the veins lead to lower MREE abundances in the reacted melts with the appearance of marked positive Zr–Hf anomalies (Fig. 19d–g). Another distinctive feature of the reacted melts is positive Eu anomalies (Figs 14a, c and 17c), which are well reproduced

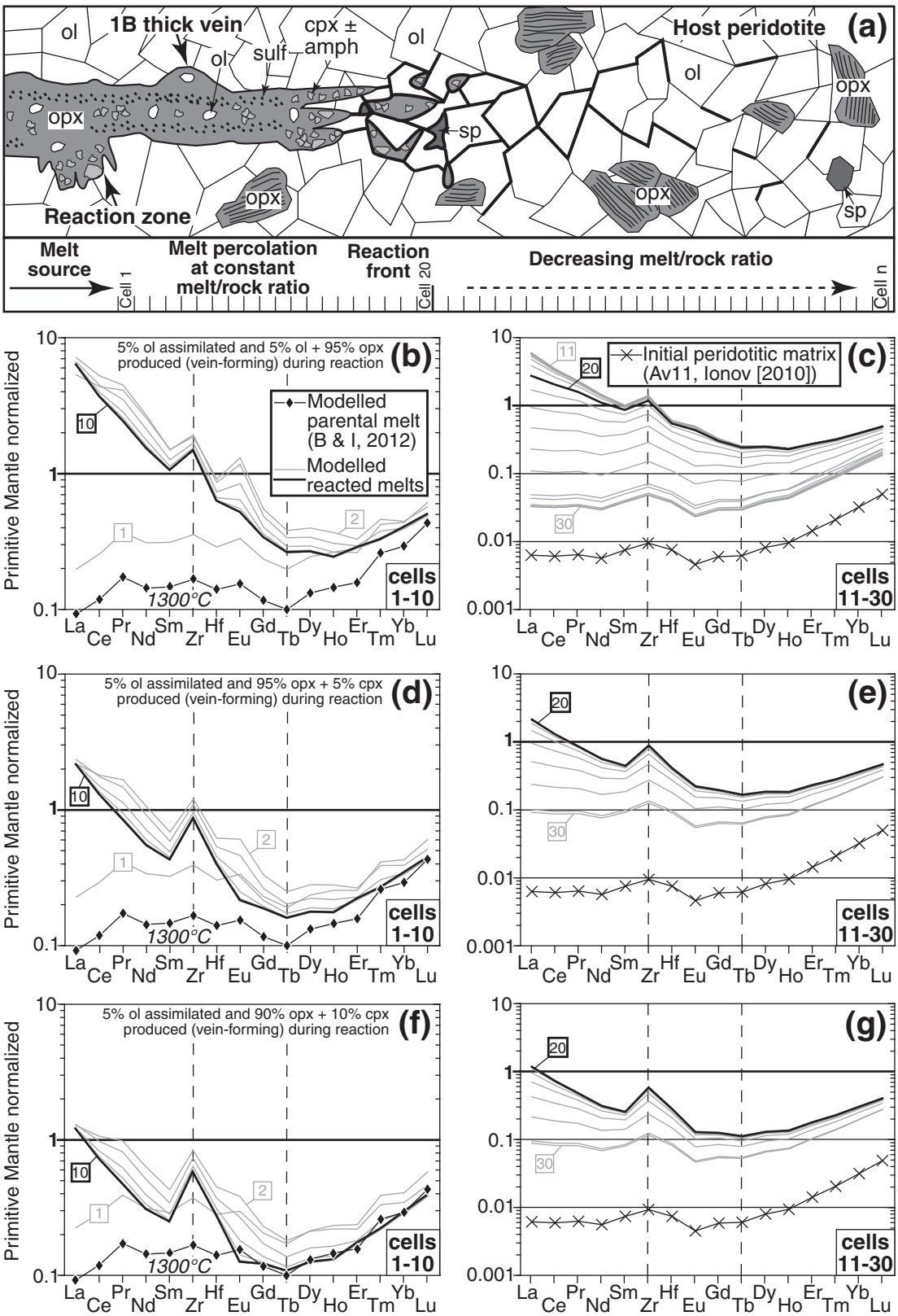

Fig. 19. A schematic illustration and primitive mantle-normalized (McDonough & Sun, 1995) REE plus Zr–Hf patterns of the numerical plate model results of melt percolation, leading to the formation of Type 1B veins in Avacha harzburgites. The trace element composition of the initial

(continued)

by the plate modelling for each set of conditions in Fig. 19b–f. The plate modelling best matches the trace element features of the thin Type 1B veins if 90% opx and 10% cpx crystallize (Fig. 19f and e). Adding minor amphibole to the vein assemblage [1% according to the model in Bénard & Ionov (2012)] does not significantly change the trace element patterns (SD Table 2). These modelling results are consistent with the relatively high cpx abundances in the thick Type 1B vein reaction zones (Fig. 6c and d) and with the complementary roles of melt fractionation and re-equilibration with the matrix in producing U-shaped REE patterns with positive Zr–Hf spikes. The generally smaller Zr–Hf spikes in the model results, compared with those inferred from thin Type 1B veins and Type L pockets (Fig. 19b–f), may result from a kinetic process during rapid melt percolation, leading to incomplete re-equilibration with the matrix by diffusive flux for Zr–Hf in the parental melt of the thin Type 1B veins. This is consistent with recent experimental data at 1300°C, which suggest lower diffusivities for Zr–Hf than for MREE in olivine (Spandler & O'Neill, 2010).

The results of the plate modelling for Type 2 veins are presented in Fig. 20a. The main modelling parameters are identical to those for Type 1 veins but with constant proportions of crystallized opx and amphibole [products in reaction (3)] to form the veins. The plate modelling correctly reproduces the slightly U-shaped REE patterns with slight positive Eu anomalies and marked positive Zr–Hf spikes observed in Type 2 veinlets (Fig. 20a).

The modelling procedure and results above differ significantly from those of previous applications of the plate model. First, our modelling is an attempt to simulate the evolution of both depleted (Type 1) and enriched (Type 2) trace element patterns of arc melts during their reactive percolation through harzburgite, whereas most previous studies have addressed the metasomatic overprint of intraplate basalts on lherzolite or harzburgite bulk-rock and mineral chemistry (e.g. Bodinier *et al.*, 1990; Ionov *et al.*, 2002). Second, we used specific modelling parameters to account for the size (e.g. trace element variations in reactions zones of less than 1 mm in Fig. 6c) and the location (e.g. vein-forming minerals) of our observations, whereas most earlier works used large cell numbers with generally much lower melt/rock ratios and porosity to simulate porous flow producing disseminated modal or cryptic metasomatism in lithospheric columns (e.g. Bedini *et al.*, 1997; Ionov *et al.*, 2002). Third, there is no clear relationship between melt/rock ratios, matrix porosity and the effects of the fractionation–reactive percolation process, because these are observed in both relatively thick veinlets (Type 2 veinlets, Fig. 7c) and disseminated minerals (Type L pockets, Fig. 4d). Furthermore, these relationships may be masked by the contrasting degrees of disequilibrium between the melts and the host harzburgite, inferred respectively from the Type 1 and Type 2 veins in our samples. This is another reason why our modelling should be viewed only as a test for the effects of local fractionation and reaction with the host harzburgite on melt trace element patterns.

To sum up, the plate modelling results strongly support the fractionation and reaction processes we inferred from petrographic and geochemical data for Avacha Type 1 and Type 2 veins.

Vein-related metasomatism and its impact on the host harzburgites

Processes of vein-related metasomatism

We find that if veins cut pre-existing fractures in the host peridotites, these fractures may be filled with metasomatic minerals related to Type 1A or Type 1B veins (cpx II and amph II), usually located in opx-rich metasomatic pockets (Type F, Fig. 15a). In the following sub-section we examine the processes of trace element fractionation occurring during pervasive vein-related metasomatism. We use the range of processes listed below to model the reactive percolation mechanism in fractures and at grain boundaries.

(1) The metasomatic agent intruding the host-rock fractures was probably a volatile-rich fluid or melt. The role of volatiles is shown by abundant fluid-inclusions along the veins filling fractures (SD Fig. 2), the presence of amph II in Type F pockets (Fig. 15a and SD Fig. 2) and lower Ti in spinel II and amph II in Type F pockets related to Type 1 veins than in the veins themselves (Figs 10b and 11b). Furthermore, the abundances of fluid-mobile elements (LILE and Sr) are constantly high in minerals from Type F pockets (e.g. increasing $[U/Th]_N$ in amph II with percolation distance in Fig. 15d and e). This may indicate the

Fig. 19 Continued
melt used is the modelled parental melt formed at 1300°C in the study by Bénard & Ionov (2012), and the initial peridotitic matrix mineral proportions and trace element composition correspond to those of the harzburgitic sample Av11 from Ionov (2010). (a) Within each model cell, the melt is (1) assimilating host olivine at constant rates (5% in this figure), (2) continually evolves owing to vein-forming mineral fractionation (opx ± ol ± cpx) and (3) continually re-equilibrates with the overall peridotitic mineral assemblage (olivine + opx + sp + cpx + amph). The melt volume and melt/rock ratio are decreasing from the melt source (i.e. inside the vein and at the reaction front) to the host peridotite. The relative proportions of minerals produced during vein-forming reactions are kept constant within each modelling run [respectively illustrated in (b)–(c), (d)–(e) and (f)–(g)]. The overall modelling set aims to reproduce the melt reactive percolation processes at the scale of a single xenolith and uses reactions (1) and (2) in the text for Type 1B veins. Framed numbers in diagrams indicate those for model cells. (See Table 8 for a fully referenced list of partition coefficients and the initial melt used in the modelling, SD Table 2 for all modelling results, and text for further details.)

Table 8: Mineral–melt and mineral–fluid partition coefficients and initial peridotite and melt compositions (ppm) used in the modelling

	Partition coefficients ($D^{mineral/melt}$ and $*D^{mineral/fluid}$)					Peridotite matrix	Percolating melts	
	olivine	opx	cpx	spinel	amphibole	Av11 (Ionov, 2010)	Type 1	Type 2
Sr	0·000064*	0·000064*	1·43*	—	1·70*	0·160	22	—
Zr	0·004	0·005	0·13	0·005	0·156	0·098	2·33	77
Nb	0·25*	0·25*	0·172*	—	1·1*	0·010	0·016	—
Ba	0·00002*	0·00002*	0·143*	—	0·51*	0·26	0·693	—
La	0·0001	0·0002	0·054 (1·43*)	0·0004	0·086 (1·43*)	0·004	0·059	6·23
Ce	0·0002	0·0004	0·086 (2*)	0·0005	0·138 (2*)	0·010	0·198	14
Pr	0·0003	0·0006	0·139 (2*)	0·00065	0·222 (2*)	0·002	0·043	1·87
Nd	0·0004	0·001	0·187 (6·67*)	0·00058	0·299 (6·67*)	0·007	0·178	8·43
Sm	0·00044	0·003	0·291 (6·67*)	0·00048	0·466 (6·67*)	0·003	0·059	2·03
Eu	0·00056	0·004	0·35	0·00045	0·56	0·0007	0·024	0·669
Gd	0·00076	0·0128	0·4	0·00042	0·64	0·003	0·063	1·98
Tb	0·00104	0·0186	0·429 (13*)	0·00041	0·686 (13*)	0·0006	0·010	0·325
Dy	0·0014	0·0261	0·442	0·0004	0·707	0·005	0·088	2·18
Ho	0·00184	0·0356	0·439	0·00041	0·702	0·001	0·022	0·452
Er	0·00236	0·0474	0·436	0·00042	0·698	0·006	0·068	1·36
Tm	0·00296	0·0617	0·433	0·00045	0·693	0·001	0·018	0·183
Yb	0·00364	0·0787	0·43 (7·14*)	0·00048	0·688 (7·14*)	0·014	0·128	1·39
Lu	0·0044	0·0986	0·427 (7·14*)	0·00053	0·683 (7·14*)	0·003	0·029	0·203
Hf	0·006	0·01	0·2 (1·43*)	0·01	0·24 (1·43*)	0·002	0·039	1·86
Pb	0·0012*	0·0012*	0·286*	—	0·081*	0·019	0·400	—
Th	0·0072*	0·0072*	1·3*	—	0·93*	0·0004	0·001	—
U	0·0077*	0·0077*	0·081*	—	0·35*	0·0005	0·0004	—

opx, orthopyroxene; cpx, clinopyroxene. $D^{mineral/melt}$ values used in the modelling are those compiled by Ionov *et al.* (2002) which include: (1) $D^{cpx/melt}$ from Hart & Dunn (1993), Hauri *et al.* (1994), Johnson (1998) and Lundstrom *et al.* (1998); (2) $D^{cpx/opx}$, $D^{cpx/ol}$, $D^{cpx/sp}$ from Bedini *et al.* (1997) and Vernières *et al.* (1997); (3) $D^{amph/melt}$ from Ionov *et al.* (2002). Sr, Nb, Ba, Pb, Th and U abundances were solely modelled for fluid-harzburgite reactions (Fig. 21). $D^{olivine/fluid}$ (extrapolated to opx) and $D^{amphibole/fluid}$ are from Brenan *et al.* (1995); $D^{cpx/fluid}$ are from Stalder *et al.* (1998) for Sr, Nb, Ba and Pb, and from Brenan *et al.* (1995) for Th and U. $D^{cpx/fluid}$ (extrapolated to amphibole) for La, Ce (extrapolated to Pr), Sm (extrapolated to Nd), Tb, Yb (extrapolated to Lu) and Hf are from Stalder *et al.* (1998). The initial peridotite matrix composition corresponds to that of sample Av11 studied by Ionov (2010). The Type 1 percolating melt composition is the 1300°C modelled parental melt of Bénard & Ionov (2012) (see also text and Figs 18 and 19). The Type 2 percolating melt composition corresponds to that of the averaged glass in selvages (see also text, Table 7 and Figs 18 and 20).

involvement of a fluid-rich component separated according to $D^{melt/fluid}$ (Keppler, 1996).

(2) The metasomatic cpx II and amph II may overgrow opx I or spinel I in the Type F pockets and coexist with opx II and possibly with olivine neoblasts (Figs 4c, 8a, 15a and SD Fig. 2), which suggests that they form from either of the simplified reactions (5) and (6):

$$\text{olivine} + \text{opx I} + \text{cpx I} + \text{spinel I} + \text{volatile-rich melt} \Rightarrow \text{opx II} + \text{amph II} \pm \text{cpx II} \quad (5)$$

$$\text{opx I} + \text{cpx I} + \text{spinel I} + \text{fluid} \Rightarrow \text{amph II} + \text{olivine} \pm \text{cpx II}. \quad (6)$$

These reactions resemble those observed in mantle metasomatism experiments and inferred for mantle xenoliths or exhumed mantle sections (Sen & Dunn, 1994, and references therein).

(3) Both cpx II and amph II in Type F pockets are progressively depleted in MREE with increasing distance from their vein source (Fig. 15b–e). We attribute this chemical behaviour to the progressive re-equilibration of the vein-derived volatile-rich agent with a MREE-depleted peridotite with increasing percolation distance. This is likely to be due to diffusional exchange between the metasomatic agent and wall-rock minerals during percolation in fractures and at grain boundaries (e.g. Bodinier *et al.*,

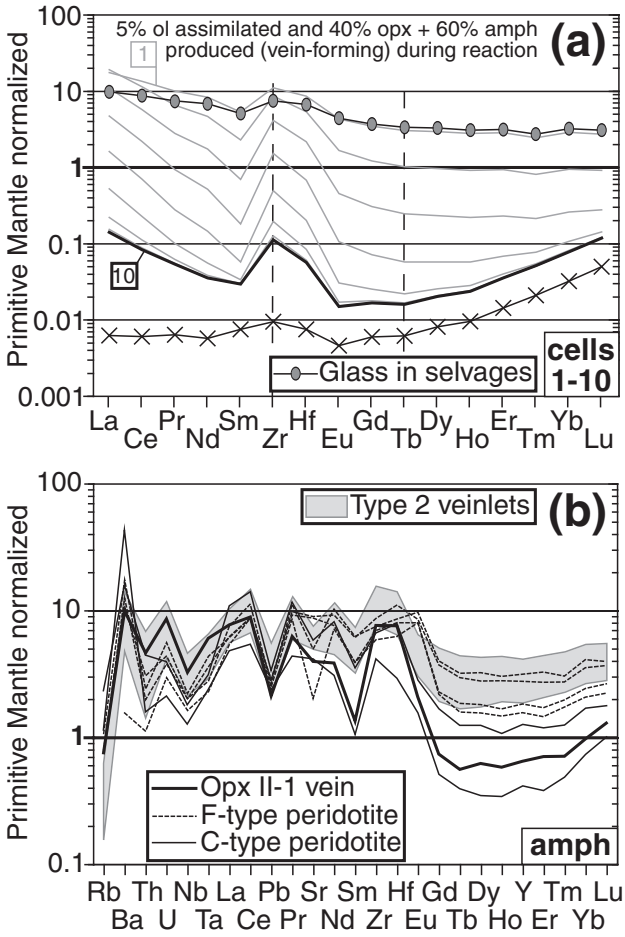

Fig. 20. (a) Primitive mantle-normalized (McDonough & Sun, 1995) REE plus Zr–Hf patterns of the numerical plate model results of melt percolation, leading to the formation of Type 2 veinlets in the Avacha harzburgites. The trace element composition of the initial melt used is that of the analyzed glass in the selvages (line with grey circles; others are the same as in Fig. 19), and the initial peridotitic matrix mineral proportions and trace element composition correspond to those of the harzburgitic sample Av11 from Ionov (2010). The modelling procedure is similar to that used to model Type 1 veins (see Fig. 19), but uses reactions (3) and (4) in the text for Type 2 veinlets. Framed numbers in diagrams indicate those for model cells. (b) Primitive mantle-normalized (McDonough & Sun, 1995) extended patterns for amphibole in Type 2 veinlets (grey field) compared with amphibole reported by Ishimaru *et al.* (2007) in their 'opx II-1' veins (bold black line) and disseminated amphiboles reported by Ishimaru & Arai (2008) in their 'Type F' (dashed black lines) and 'Type C' (fine black lines) Avacha peridotites. (See Table 8 for a fully referenced list of partition coefficients and the initial melt used in the modelling, SD Table 3 for all modelling results, and text for further details.)

1990; Ionov *et al.*, 2002). In particular, Zr and Hf are progressively depleted relative to MREE in cpx II with increasing percolation distance (Fig. 15c and e). Even if the solubility of HFSE in the metasomatic agents is low (e.g. Keppler, 1996), some experimental data suggest no fractionation of HFSE relative to MREE during fluid–melt separation at shallow mantle depths (e.g. Ayers & Eggler, 1995). The marked negative Zr–Hf anomalies in cpx II may then result (together with the MREE depletion) from complete equilibration of cpx II with opx in reactions (5) and (6), in line with experimental $D^{cpx/opx}$ (e.g. Green *et al.*, 2000). This implies that the budget in moderately incompatible elements (HREE–MREE–Zr–Hf) of metasomatizing fluids can be buffered by the harzburgite mineralogy at very short distances (Fig. 15a).

The continuum of processes above results in the production of a wide range of trace element patterns in disseminated metasomatic minerals, at a small distance (typically of the order of the size of a single xenolith) from their original fluid.

Impact of vein-related metasomatism on host harzburgites

To explore how the metasomatic processes examined above may affect the chemical and modal compositions of the Avacha mantle xenoliths, we compare our results with published bulk-rock data on the Avacha harzburgites from Ionov (2010).

The opx I cut by Type 1A or 1B veins show variable LREE enrichments compared with the opx I that are not cut by the veins (Fig. 13a and b). Coarse opx I cut by Type 1B veins filling fractures shows recrystallization at rims, whereas fine-grained opx II forms on coarse olivine (Fig. 4c and SD Fig. 2). REE contents of these opx rims are similar to those in the opx with the highest REE reported by Ionov (2010) (Fig. 13b). It is possible that enrichments in trace elements in some Avacha mantle xenoliths could be traced to vein sources located beyond the xenoliths reported by Ionov (2010). On the other hand, Si and opx enrichment of some Avacha peridotites (Ionov, 2010) cannot be attributed to the processes inferred in this study because they form not only opx, but also minerals with lower SiO_2 contents such as olivine, amphibole and cpx [e.g. reaction (6), Fig. 4c and SD Fig. 2].

Possible links between accessory amphibole and cpx reported by Ionov (2010) and those in Type F pockets related to Type 1 veins in our study are suggested by the similarities of their major element compositions (Fig. 11 and SD Fig. 4). Amphibole II and cpx II formed in reactions (5) and (6) are likely to be the major hosts in the Avacha harzburgites for highly incompatible elements (Rb, Ba, U, Sr and LREE), whose percolation front advances faster (chromatographic fractionation) than for HFSE and MREE (Fig. 15d and e; Bedini *et al.*, 1997; Ionov *et al.*, 2002). Ionov (2010) reported positive anomalies of the fluid-mobile elements Rb, Ba, U and Sr and flat $MREE_N$–$LREE_N$ patterns in some bulk-rock xenoliths, and found a robust positive correlation between modal amphibole and LREE and Sr abundances in bulk-rocks. We speculate that amphibole and cpx in the Avacha mantle xenoliths reported by Ionov (2010) may have precipitated from evolved melts and fluids at the percolation front of the initial liquids supplied by the Type 1 veins.

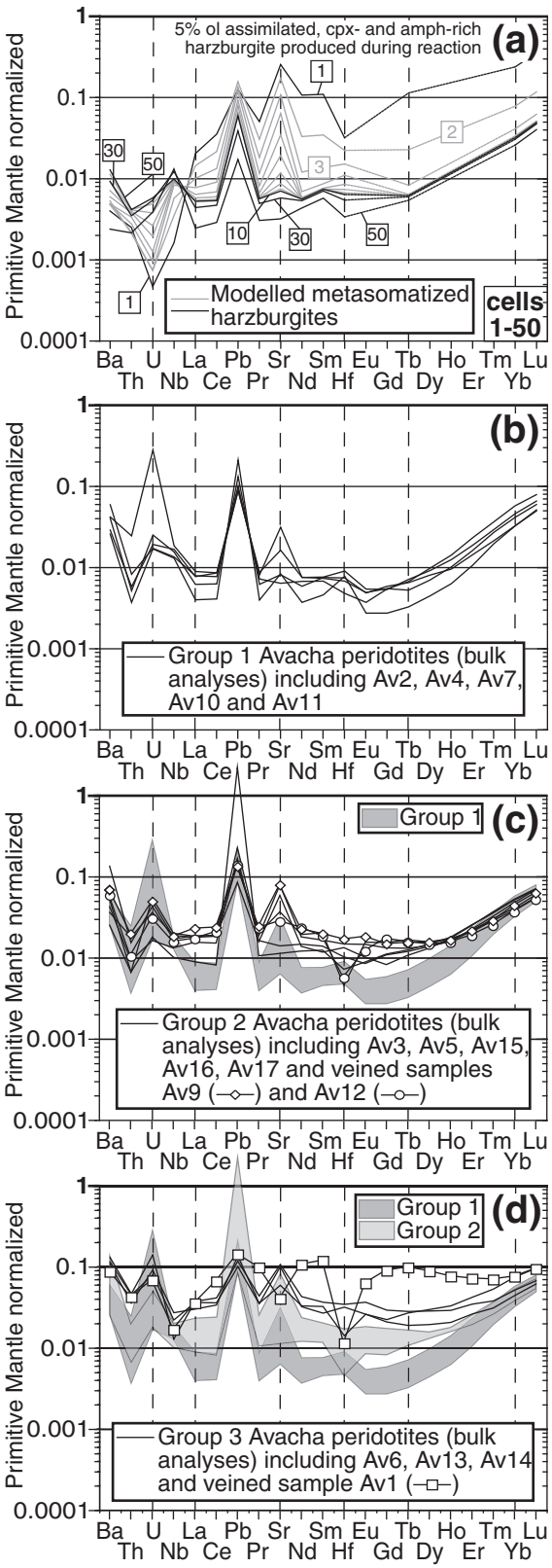

Fig. 21. (a) Primitive mantle-normalized (McDonough & Sun, 1995) extended trace element patterns for the numerical plate model results

We performed reactive porous flow modelling with the plate model (i.e. instantaneous fluid/mineral equilibration at low porosity and fluid/rock ratio) to test if the formation of disseminated amph II and cpx II deriving from Type 1 veins alone could produce the range of trace element concentrations observed in the bulk-rock xenoliths reported by Ionov (2010). In addition to REE and Zr–Hf, we have included Ba, Th, U, Nb, Pb and Sr in this model by using a specific set of $D^{\text{mineral/fluid}}$ values compiled from Brenan *et al.* (1995) and Stalder *et al.* (1998), together with the same initial liquid for Type 1 veins and cpx- and amphibole-poor Av11 initial matrix as in previous models (Fig. 19 and Table 8). The model uses constant assimilation rates and produces the supplementary amount of cpx and amphibole [reactants and products are from reactions (5) and (6)] in the initial matrix to ultimately match the modal composition of the Avacha xenoliths with the highest amount of amphibole (Av13) and cpx (Av15) (Ionov, 2010). Modelling results are shown and compared with the published data in Fig. 21.

The results show enrichments of REE and Sr and negative Hf anomalies in the percolated matrix close to the melt source (cell 1 in Fig. 21a). With increasing percolation distance, the modelled metasomatized harzburgites become progressively depleted in HREE, then MREE and LREE, and show Sr and Pb positive spikes and increasing Ba abundances and $[U/Th]_N$ (cells 2–10 in Fig. 21a). These results are in good agreement with the effects of vein-related pervasive metasomatism documented in this study for Type 1 veins (Fig. 15) and elsewhere (e.g. Bodinier *et al.*, 1990; Ionov *et al.*, 2002); that is, fluid buffering for MREE–HREE through diffusional exchange at the xenolith (centimetre) scale, and greater percolation distances (chromatographic fractionation) for the more incompatible LREE and fluid-mobile Ba, U, Pb and Sr (Fig. 15).

The modelling results encompass the spectrum of whole-rock trace element patterns reported for the Avacha xenoliths by Ionov (2010). We group these xenolith patterns

Fig. 21 Continued
of fluid percolation, leading to the formation of cpx and amphibole in Type F pockets in the Avacha harzburgites. The trace element composition of the initial fluid-rich melt used is the modelled parental melt formed at 1300°C in the study by Bénard & Ionov (2012), and the initial peridotitic matrix mineral proportions and trace element composition correspond to those of the harzburgitic sample Av11 from Ionov (2010). The modelling procedure uses reactions (5) and (6) in the text for Type F pocket formation at low fluid/rock ratio and porosity. Framed numbers in diagrams indicate those for the model cells. (b–d) Primitive mantle-normalized (McDonough & Sun, 1995) extended trace element patterns for bulk xenoliths from Ionov (2010), classified into three groups, based on enrichment in incompatible elements from group 1 (b) to group 2 (c) and group 3 (d). (See Table 8 for a fully referenced list of partition coefficients and the initial melt used in the modelling, and text for further details.)

based on increasing REE abundances (from group 1 to 3, respectively in Fig. 21b–d); all three groups have positive U, Pb and Sr anomalies. The group 1 patterns (with lowest REE) are similar to those modelled in cells 10–50 in Fig. 21a, consistent with limited host-buffered enrichment (Fig. 21b). The group 2 and 3 patterns are similar to those modelled in cells 2–10 and 1–2, respectively (Fig. 21a); that is, close to the melt source (Fig. 21c and d). We argue that the group 2 and 3 Avacha xenoliths may have experienced vein-related metasomatism similar to that documented in the vicinity of the Type 1 veins in this study. This inference is consistent with the presence of Type 1 veins in xenoliths Av1, Av9 and Av12 from these two groups (Fig. 21c and d). We conclude that the distribution of accessory metasomatic phases and related trace element enrichments in the Avacha xenoliths reported by Ionov (2010) could be largely produced by the percolation of Type 1 mantle-derived melts and related fluids in the shallow mantle.

Comparison with previous studies of metasomatism in the Avacha peridotites

Recent studies (Ishimaru *et al.*, 2007; Ishimaru & Arai, 2008; Halama *et al.*, 2009) reported opx-rich veins and trace element data for metasomatic minerals in other collections of Avacha peridotite xenoliths. Halama *et al.* (2009) focused on coarse-grained websteritic veins, which are not considered here. Ishimaru *et al.* (2007) reported sulfide- and hornblende-bearing, opx-rich veins ('opx II-1') and disseminated metasomatic minerals in peridotites with abundant fine-grained opx, and Ishimaru & Arai (2008) discussed the origin of opx-rich veins and the chemistry of disseminated amphiboles in their 'Type F' (fine-grained) and 'Type C' (coarse-grained) peridotites. Representative trace element data for amphibole in opx II-1 veins from Ishimaru *et al.* (2007) and disseminated amphiboles from Ishimaru & Arai (2008) are shown in comparison with Type 2 veinlet amphibole in Fig. 20b.

Ishimaru & Arai (2008) inferred that a sulfide-bearing opx-rich vein in their sample '#530' was produced by a 'sulphur-bearing silicic melt derived from a slab'. The high Mg# and very low alkalis, Al and trace element abundances in the vein minerals reported by Ishimaru & Arai (2008) are not consistent with a slab-melt affinity (e.g. Defant & Drummond, 1990; Kepezhinskas *et al.*, 1995, 1996; Rapp *et al.*, 1999; Prouteau *et al.*, 2001). By comparison, this vein appears to be similar to the Type 1B veins in our study and rather shows a low-Ca boninitic affinity (Bénard & Ionov, 2012).

The low Cr content in the opx II-1 vein minerals of Ishimaru *et al.* (2007) is characteristic of minerals in selvages and Type 2 veins and veinlets (Fig. 12). The pronounced positive Zr–Hf spikes and MREE–HREE depletion relative to LREE (U-shaped REE patterns), as well as trace element abundances in most hornblendes in the opx II-1 veins from Ishimaru *et al.* (2007) or disseminated in Type F and Type C peridotites from Ishimaru & Arai (2008), are all very similar to those in amphibole from Type 2 veinlets in this study (Fig. 20b). Furthermore, some amphiboles reported by those researchers are lower in MREE–HREE–Zr–Hf than those in Type 2 veinlets, which look very much like andesite–peridotite interaction products far from the melt source (i.e. possibly disseminated in pockets recording low melt/rock ratios and porosity) obtained by modelling in this study (Fig. 20a). This leads us to conclude that the minerals reported by Ishimaru *et al.* (2007) and Ishimaru & Arai (2008) were formed by reaction of selvage-derived andesitic melts with their host peridotites at crustal depths. Ishimaru *et al.* (2007) also interpreted the apparent replacement of olivine by fine-grained opx in some Avacha xenoliths as reaction with a 'SiO_2-rich hydrous fluid from the slab'. Based on our observation that this type of modal metasomatism is common in xenoliths hosting Type 2 veins and veinlets (SD Fig. 3), we argue that it was probably produced by hydrous fluid-rich derivates of melts crystallizing in Type 2 veins and veinlets or directly from the amphibole selvages; that is, it is due to interaction of the mantle xenoliths with their host magmas rather than to mantle processes.

Ishimaru *et al.* (2007) interpreted opx II-1 veins and some disseminated metasomatic minerals as resulting from the infiltration of 'a hydrous melt of adakitic affinity derived from the subducted slab' because minerals have 'high Sr/Y and LREE/HREE'. Recent work suggests that a variety of petrological processes can generate high Sr/Y and La/Y in magmatic rocks (Moyen, 2009). Here we argue that fractionation–reactive percolation is an efficient way to produce high Sr/Y and LREE/MREE on a small spatial scale (Figs 17 and 20). Importantly, the trace element signature of the initial liquid that formed the Type 2 veins and veinlets, which is similar to the andesitic glass in the selvages, cannot be reconciled with typical adakitic signatures (Fig. 18). From a more general point of view, adakite formation is attributed to melting of subducted oceanic crust, which is restricted to young or torn subducted oceanic plates (Peacock *et al.*, 1994; Yogodzinski *et al.*, 2001). This is unlikely to occur beneath Avacha according to geophysical data [e.g. 120 km depth of the Pacific slab (Gorbatov *et al.*, 1999)] or thermal modelling, which infers a 600–700°C slab temperature (Davaille & Lees, 2004; Manea *et al.*, 2005).

To sum up, many petrographic and chemical features of the enriched Avacha mantle xenoliths reported by Ishimaru *et al.* (2007) and Ishimaru & Arai (2008) (fine-grained opx, opx–amphibole veins, and disseminated metasomatic minerals) are not related to original arc mantle melt or fluid signatures, but rather reflect late-stage interaction between the xenoliths and their host andesitic magma. The confusion may be partly due to the

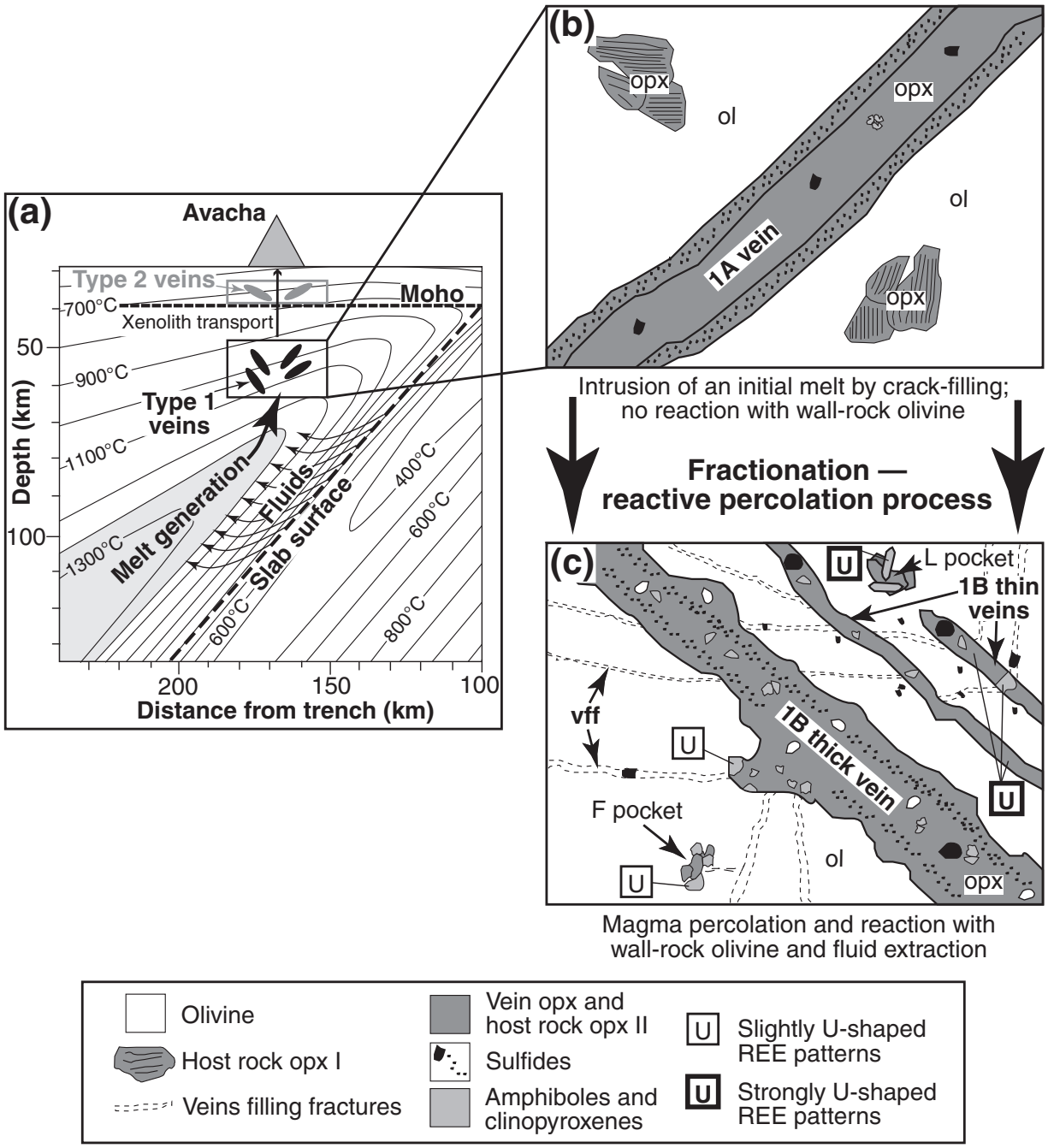

Fig. 22. Schematic illustration of the evolution ('fractionation–reactive percolation' process) of the mantle-derived melt crystallizing Type 1 veins that cut the Avacha harzburgite xenoliths. (a) Melts generated at high temperature in the asthenospheric mantle wedge form veins in the sub-arc lithosphere during their ascent. (b) A high-temperature hydrous, silica-rich melt (Type 1A veins) with a flat REE–HFSE pattern cuts the host-rock olivine by hydraulic fracturing without reaction. (c) The initial melt crystallizing Type 1A veins fractionates leading to REE and Sr enrichment while reacting with the wall-rock peridotite through diffusive flux with the host olivine and dissolution–precipitation reactions involving host olivine and spinel I, leading to U-shaped REE patterns with positive Zr–Hf spikes in all minerals from Type 1B thick vein reaction zones (slightly U-shaped REE patterns) and Type 1B thin veins (strongly U-shaped REE patterns). The 'modified' melt signature is disseminated in the host peridotite through Type L melt pockets (strongly U-shaped REE patterns) originating from last melt percolating in Type 1B thin vein conduits (melt–rock interaction end-products). Residual fluid extraction occurs during Type 1B veins crystallization through fractures (veins filling fractures). The fluids are progressively modified with increasing distance from their source in Type 1B veins towards the host peridotites, and produce metasomatic minerals (cpx II and amph II) growing upon opx I or spinel I in disseminated pockets. The metasomatic pockets commonly contain amph II with slightly U-shaped REE patterns and negative HFSE anomalies. During their transport to the surface and/or their storage in deep crustal magma chambers, the Avacha xenoliths experience further fracturing and veining triggered by the host magma. These late-stage interactions produced the Type 2 veins and veinlets identified in this study, as well as abundant fine-grained recrystallization in some samples (SD Fig. 3).

effects of the fractionation–reactive percolation experienced by the intruding melt in the xenoliths, which can produce chemical signatures similar to those attributed to slab melts.

In general, both this and previous studies demonstrate the importance of melt–rock and fluid–rock interaction processes in the sub-arc lithospheric mantle. These processes, identified in the veined Avacha harzburgites, are summarized in Fig. 22. We argue that a single liquid (e.g. of low-Ca boninitic affinity; Bénard & Ionov, 2012) percolating through the sub-arc mantle lithosphere (Fig. 22a and b) can generate disseminated melt pockets (Type L) with highly evolved major and trace element abundances through fractionation and melt–rock interaction (fractionation–reactive percolation, Figs 14 and 22c). Furthermore, the process of metasomatic fluid extraction from the vein conduits inferred in our study may produce both disseminated accessory minerals and metasomatic pockets (Type F) in the host xenoliths, with a broad range of compositions ultimately related to a single initial melt (Figs 10, 11, 15, 22 and SD Fig. 4). These metasomatic products may control the budgets of incompatible trace elements in the bulk xenoliths.

A corollary of this major inference of our study is that, when taken out of their genetic context, the major and trace element compositions of metasomatic minerals in xenoliths should not be used to infer the chemical signature of the initial metasomatic agent because the latter may experience strong local fractionation during percolation in the peridotite host. Finally, because many Avacha xenoliths (see, for instance, SD Fig. 3), and most probably arc xenoliths in general, can be contaminated during their ascent and intermittent storage in the arc crust (Fig. 22), the fractionation–reactive percolation process may lead to confusion between mantle metasomatism and late-stage interaction between the xenoliths and their host magma.

CONCLUSIONS

(1) Harzburgite xenoliths from Avacha contain opx-rich, amphibole-bearing veins resulting from recent intrusion of mantle-derived magmas in the sub-arc lithospheric mantle. Some veins (Type 1A) show no reaction with the host peridotite, whereas others (Type 1B) show evidence for re-equilibration with, and partial assimilation of host peridotite minerals.

(2) Petrographic and major element data, as well as low REE and HFSE contents, suggest an origin from magmas generated by fluxed-melting of a harzburgitic source. Minerals in the Type 1B veins have higher Al, Ti, Na and REE, and formed from fractionated hydrous derivatives of the melts forming the Type 1A veins. Interaction of these fractionated liquids with depleted host harzburgites produced U-shaped REE patterns with positive Zr–Hf anomalies in thin veins and melt pockets associated with Type 1B veins.

(3) This type of magma–host-rock interaction is referred to here as 'fractionation–reactive percolation' and includes the following processes: (a) diffusion of elements from the percolating melt ('diffusive flux'); (b) fluid-assisted dissolution–precipitation reactions with the host peridotite at the percolation front; (c) extraction of evolved hydrous fluids from the veins into the host harzburgites. Numerical modelling demonstrates that these processes can produce U-shaped REE patterns with positive Zr–Hf anomalies from an initial melt with a flat REE–HFSE pattern.

(4) Metasomatizing fluids escaping from the veins enriched the host harzburgites in LREE, MREE and LILE, and precipitated accessory cpx and amphibole; the trace element signatures in these minerals are distinct from those in cpx and amphibole in the parental veins only a few millimetres to centimetres away. Thus, a broad range of major and trace element compositions in disseminated metasomatic minerals in the vicinity of a melt conduit may be produced from a single initial liquid. If this is the case, the compositions of the initial metasomatic agents cannot be directly assessed from those of accessory minerals in peridotites because the primary melt signatures in the latter are overprinted by fractionation effects.

(5) Thin amphibole-bearing veins formed in some Avacha harzburgites by the intrusion of the host andesitic magma into fractures. Their trace element abundances are higher than in veins of mantle origin but some features are similar (e.g. U-shaped REE patterns with positive Zr–Hf spikes) because both were affected by fractionation–reactive percolation processes. Crystallization products of the andesite-related veins have been mistaken for those of mantle origin in previous studies on Avacha mantle xenoliths.

SUPPLEMENTARY DATA

Supplementary data for this paper are available at *Journal of Petrology* online.

ACKNOWLEDGEMENTS

C. Alboussière made thick sections. C. Merlet and J. L. Devidal provided analytical assistance for EPMA, and O. Bruguier for ICP-MS measurements. M. Godard provided the 'plate model' software used for melt percolation and porous flow modelling. Comments and advice from S. Arai, C.-T. Lee, I. J. Parkinson and two anonymous reviewers helped to considerably improve the clarity and quality of the paper. Editorial handling by S. P. Turner is much appreciated.

FUNDING

The research was supported by funding from Centre National de la Recherche Scientifique (CNRS) and

Institut National des Sciences de l'Univers (INSU) (France) including a PNP project in 2010 (theme SEDITPS) entitled: 'The role of subduction in the origin of the cratonic mantle'.

REFERENCES

Ackerman, L., Jelinek, E., Medaris, G., Jezek, J., Siebel, W. & Strnad, L. (2008). Geochemistry of Fe-rich peridotites and associated pyroxenites from Horní Bory, Bohemian Massif: Insights into subduction-related melt–rock reactions. *Chemical Geology* **259**, 152–167.

Arai, S., Takada, S., Michibayashi, K. & Kida, M. (2004). Petrology of peridotite xenoliths from Iraya volcano, Philippines, and its implication for dynamic mantle-wedge processes. *Journal of Petrology* **45**, 369–389.

Arai, S., Shimizu, Y., Morishita, T. & Ishida, Y. (2006). A new type of orthopyroxenite xenolith from Takashima, Southwest Japan: silica enrichment of the mantle by evolved alkali basalt. *Contributions to Mineralogy and Petrology* **152**, 387–398.

Ayers, J. C. & Eggler, D. H. (1995). Partitioning of elements between silicate melt and H_2O–NaCl fluids at 1·5 and 2·0 GPa: Implications for mantle metasomatism. *Geochimica et Cosmochimica Acta* **59**, 4237–4246.

Bali, E., Falus, G., Szabó, C., Peate, D. W., Hidas, K., Török, K. & Ntaflos, T. (2007). Remnants of boninitic melts in the upper mantle beneath the central Pannonian Basin? *Mineralogy and Petrology* **90**, 51–72.

Ballhaus, C., Berry, R. F. & Green, D. H. (1991). High pressure experimental calibration of the olivine–orthopyroxene–spinel oxygen geobarometer: implications for the oxidation state of the upper mantle. *Contributions to Mineralogy and Petrology* **107**, 27–40.

Bédard, J. H. (1989). Disequilibrium mantle melting. *Earth and Planetary Science Letters* **91**, 359–366.

Bédard, J. H. (1999). Petrogenesis of boninites from the Betts Cove Ophiolite, Newfoundland, Canada: Identification of subducted source components. *Journal of Petrology* **40**, 1853–1889.

Bedini, R. M., Bodinier, J.-L., Dautria, J.-M. & Morten, L. (1997). Evolution of LILE-enriched small melt fractions in the lithospheric mantle: a case study from the East African Rift. *Earth and Planetary Science Letters* **153**, 67–83.

Bénard, A. & Ionov, D. A. (2010). PGE and trace elements in veined sub-arc mantle xenoliths, Avachinsky volcano, Kamchatka. *Geochimica et Cosmochimica Acta* **74**, A76.

Bénard, A. & Ionov, D. A. (2012). A new petrogenetic model for low-Ca boninites: Evidence from veined sub-arc xenoliths on melt–mantle interaction and melt fractionation. *Geochemistry, Geophysics, Geosystems* **13**, Q0AF05, doi:10.1029/2012GC004145.

Bénard, A., Ionov, D. A., Shimizu, N. & Plechov, P. Y. (2011*a*). The volatile content of subduction zone melts and fluids. *Mineralogical Magazine* **75**, A513.

Bénard, A., Palle, S., Doucet, L.-S. & Ionov, D. A. (2011*b*). Three-dimensional imaging of sulfides in silicate rocks at sub-micron resolution with multi-photon microscopy. *Microscopy and Microanalysis* **17**, 937–943.

Berly, T. J., Hermann, J., Arculus, R. J. & Lapierre, H. (2006). Supra-subduction zone pyroxenites from San Jorge and Santa Isabel (Solomon Islands). *Journal of Petrology* **47**, 1531–1555.

Bodinier, J.-L., Vasseur, G., Vernieres, J., Dupuy, C. & Fabries, J. (1990). Mechanisms of mantle metasomatism: Geochemical evidence from the Lherz orogenic peridotite. *Journal of Petrology* **31**, 597–628.

Braitseva, O. A., Bazanova, L. I., Melekestsev, I. V. & Sulerzhitskiy, L. D. (1998). Large Holocene eruptions of Avacha volcano, Kamchatka (7250–3700 ^{14}C years B.P.). *Volcanology and Seismology* **20**, 1–27.

Brenan, J. M., Shaw, H. F., Ryerson, F. J. & Phinney, D. L. (1995). Mineral–aqueous fluid partitioning of trace elements at 900°C and 2·0 GPa: Constraints on the trace element chemistry of mantle and deep crustal fluids. *Geochimica et Cosmochimica Acta* **59**, 3331–3350.

Brey, G. P. & Köhler, T. (1990). Geothermobarometry in four-phase lherzolites II. New thermobarometers, and practical assessment of existing thermobarometers. *Journal of Petrology* **31**, 1353–1378.

Bryant, J. A., Yogodzinski, G. M. & Churikova, T. G. (2007). Melt–mantle interactions beneath the Kamchatka arc: Evidence from ultramafic xenoliths from Shiveluch volcano. *Geochemistry, Geophysics, Geosystems* **8**, Q04007.

Cerny, P., London, D. & Novak, M. (2012). Granitic pegmatites as reflections of their sources. *Elements* **8**, 289–294.

Chin, E. J., Lee, C.-T., Luffi, P. & Tice, M. (2012). Deep lithospheric thickening and refertilization beneath continental arcs: Case study of the *P*, *T* and compositional evolution of peridotite xenoliths from the Sierra Nevada, California. *Journal of Petrology* **53**, 477–511.

Coltorti, M., Bonadiman, C., Faccini, B., Grégoire, M., O'Reilly, S. Y. & Powell, W. (2007). Amphiboles from suprasubduction and intraplate lithospheric mantle. *Lithos* **99**, 68–84.

Condie, K. (2005). TTGs and adakites: are they both slab melts? *Lithos* **80**, 33–44.

Davaille, A. & Lees, J. M. (2004). Thermal modeling of subducted plates: tear and hotspot at the Kamchatka corner. *Earth and Planetary Science Letters* **226**, 293–304.

Defant, M. J. & Drummond, M. S. (1990). Derivation of some modern arc magmas by melting of young subducted oceanic lithosphere. *Nature* **347**, 662–665.

Dhuime, B., Bosch, D., Bodinier, J. L., Garrido, C. J., Bruguier, O., Hussain, S. S. & Dawood, H. (2007). Multistage evolution of the Jijal ultramafic–mafic complex (Kohistan, N Pakistan): Implications for building the roots of island arcs. *Earth and Planetary Science Letters* **261**, 179–200.

Falloon, T. J. & Danyushevsky, L. V. (2000). Melting of refractory mantle at 1·5, 2 and 2·5 GPa under anhydrous and H_2O-understaturated conditions: Implications for the petrogenesis of high-Ca boninites and the influence of subduction components on mantle melting. *Journal of Petrology* **41**, 257–283.

Fourcade, S., Maury, R. C., Defant, M. J. & McDermott, F. (1994). Mantle metasomatic enrichment versus arc crust contamination in the Philippines: Oxygen isotope study of Batan ultramafic nodules and northern Luzon arc lavas. *Chemical Geology* **114**, 199–215.

Franz, L., Becker, K.-P., Kramer, W. & Herzig, P. M. (2002). Metasomatic mantle xenoliths from the Bismarck Microplate (Papua New Guinea)—thermal evolution, geochemistry and extent of slab-induced metasomatism. *Journal of Petrology* **43**, 315–343.

Gaetani, G. A. & Grove, T. L. (1998). The influence of water on melting of mantle peridotite. *Contributions to Mineralogy and Petrology* **131**, 323–346.

Garrido, C. J., Bodinier, J.-L., Dhuime, B., Bosch, D., Chanefo, I., Bruguier, O., Hussain, S. S., Dawood, H. & Burg, J.-P. (2007). Origin of the island arc Moho transition zone via melt–rock reaction and its implications for intracrustal differentiation of island arcs: Evidence from the Jijal complex (Kohistan complex, northern Pakistan). *Geology* **35**, 683–686.

Gorbatov, A., Kostoglodov, V., Suárez, G. & Gordeev, E. (1997). Seismicity and structure of the Kamchatka subduction zone. *Journal of Geophysical Research* **102**, 17883–17898.

Gorbatov, A., Dominguez, J., Suarez, G., Kostoglodov, V., Zhao, D. & Gordeev, E. (1999). Tomographic imaging of the P-wave velocity structure beneath the Kamchatka peninsula. *Geophysical Journal International* **137**, 269–279.

Green, T. H., Blundy, J. D., Adam, J. & Yaxley, G. M. (2000). SIMS determination of trace element partition coefficients between garnet, clinopyroxene and hydrous basaltic liquids at 2–7·7 GPa and 1080–1200°C. *Lithos* **53**, 165–187.

Grégoire, M., McInnes, B. I. A. & O'Reilly, S. Y. (2001). Hydrous metasomatism of oceanic sub-arc mantle, Lihir, Papua New Guinea—Part 2. Trace element characteristics of slab-derived fluids. *Lithos* **59**, 91–108.

Halama, R., Savov, I., Rudnick, R. & McDonough, W. (2009). Insights into Li and Li isotope cycling and sub-arc metasomatism from veined mantle xenoliths, Kamchatka. *Contributions to Mineralogy and Petrology* **158**, 197–222.

Hart, S. R. & Dunn, T. (1993). Experimental cpx/melt partitioning of 24 trace elements. *Contributions to Mineralogy and Petrology* **113**, 1–8.

Harte, B., Hunter, R. H. & Kinny, P. D. (1993). Melt geometry, movement and crystallization, in relation to mantle dykes, veins and metasomatism. *Philosophical Transactions of the Royal Society of London, Series A* **342**, 1–21.

Hauri, E. H., Wagner, T. P. & Grove, T. L. (1994). Experimental and natural partitioning of Th, U, Pb and other trace elements between garnet, clinopyroxene and basaltic melts. *Chemical Geology* **117**, 149–166.

Hawkesworth, C. J., Gallagher, K., Hergt, J. M. & McDermott, F. (1993). Mantle and slab contributions in arc magmas. *Annual Review of Earth and Planetary Sciences* **21**, 175–204.

Hopp, J. & Ionov, D. A. (2011). Tracing partial melting and subduction-related metasomatism in the Kamchatkan mantle wedge using noble gas compositions. *Earth and Planetary Science Letters* **302**, 121–131.

Inoue, T. (1994). Effect of water on melting phase relations and melt composition in the system Mg_2SiO_4–$MgSiO_3$–H_2O up to 15 GPa. *Physics of the Earth and Planetary Interiors* **85**, 237–263.

Ionov, D. A. (2010). Petrology of mantle wedge lithosphere: New data on supra-subduction zone peridotite xenoliths from the andesitic Avacha volcano, Kamchatka. *Journal of Petrology* **51**, 327–361.

Ionov, D. A., Bodinier, J.-L., Mukasa, S. B. & Zanetti, A. (2002). Mechanisms and sources of mantle metasomatism: major and trace element compositions of peridotite xenoliths from Spitsbergen in the context of numerical modeling. *Journal of Petrology* **43**, 2219–2259.

Ionov, D. A., Bénard, A. & Plechov, P. Yu. (2011). Melt evolution in subarc mantle: evidence from heating experiments on spinel-hosted melt inclusions in peridotite xenoliths from the andesitic Avacha volcano (Kamchatka, Russia). *Contributions to Mineralogy and Petrology* **162**, 1159–1174.

Ionov, D. A., Bénard, A., Plechov, P. Yu. & Scherbakov, V. D. (2013). Along-arc variations in lithospheric mantle compositions in Kamchatka, Russia: first trace element data on mantle xenoliths from the Klyuchevskoy Group volcanoes. *Journal of Volcanology and Geothermal Research* (in press), doi:10.1016/j.jvolgeores.2012.12.022.

Ishikawa, T. & Nakamura, E. (1994). Origin of the slab component in arc lavas from across-arc variation of B and Pb isotopes. *Nature* **370**, 205–208.

Ishimaru, S. & Arai, S. (2008). Calcic amphiboles in peridotite xenoliths from Avacha volcano, Kamchatka, and their implications for metasomatic conditions in the mantle wedge. In: Coltorti, M. & Grégoire, M. (eds) *Metasomatism in Oceanic and Continental Lithospheric Mantle. Geological Society, London, Special Publications* **293**, 35–55.

Ishimaru, S., Arai, S., Ishida, Y., Shirasaka, M. & Okrugin, V. M. (2007). Melting and multi-stage metasomatism in the mantle wedge beneath a frontal arc inferred from highly depleted peridotite xenoliths from the Avacha volcano, southern Kamchatka. *Journal of Petrology* **48**, 395–433.

Jiang, G., Zhao, D. & Zhang, G. (2009). Seismic tomography of the Pacific slab edge under Kamchatka. *Tectonophysics* **465**, 190–203.

Johnson, K. T. M. (1998). Experimental determination of partition coefficients for rare earth and high-field-strength elements between clinopyroxene, garnet, and basaltic melt at high pressures. *Contributions to Mineralogy and Petrology* **133**, 60–68.

Kelemen, P. B., Johnson, K. T. M., Kinzler, R. J. & Irving, A. J. (1990). High-field-strength element depletions in arc basalts due to mantle-magma interaction. *Nature* **345**, 521–524.

Kelemen, P. B., Shimizu, N. & Dunn, T. (1993). Relative depletion of niobium in some arc magmas and the continental crust: partitioning of K, Nb, La and Ce during melt/rock reaction in the upper mantle. *Earth and Planetary Science Letters* **120**, 111–134.

Kelemen, P. B., Hart, S. R. & Bernstein, S. (1998). Silica enrichment in the continental upper mantle via melt/rock reaction. *Earth and Planetary Science Letters* **164**, 387–406.

Kepezhinskas, P. K. & Defant, M. J. (1996). Contrasting styles of mantle metasomatism above subduction zones: Constraints from ultramafic xenoliths in Kamchatka. In: Bebout, G. E., Scholl, D. W., Kirby, S. H. & Platt, J. P. (eds) *Subduction Top to Bottom. American Geophysical Union, Geophysical Monograph* **96**, 307–314.

Kepezhinskas, P. K., Defant, M. J. & Drummond, M. S. (1995). Na metasomatism in the island-arc mantle by slab melt–peridotite interaction: evidence from mantle xenoliths in the North Kamchatka arc. *Journal of Petrology* **36**, 1505–1527.

Kepezhinskas, P. K., Defant, M. J. & Drummond, M. S. (1996). Progressive enrichment of island arc mantle by melt–peridotite interaction inferred from Kamchatka xenoliths. *Geochimica et Cosmochimica Acta* **60**, 1217–1229.

Keppler, H. (1996). Constraints from partitioning experiments on the composition of subduction-zone fluids. *Nature* **380**, 237–240.

Lee, C.-T., Rudnick, R. L. & Brimhall, G. H., Jr (2001). Deep lithospheric dynamics beneath the Sierra Nevada during the Mesozoic and Cenozoic as inferred from xenolith petrology. *Geochemistry, Geophysics, Geosystems* **2**, doi:10.1029/2001GC000152.

Levin, V., Park, J., Brandon, M., Lees, J., Peyton, V., Gordeev, E. & Ozerov, A. (2002). Crust and upper mantle of Kamchatka from teleseismic receiver functions. *Tectonophysics* **358**, 233–265.

London, D. (2009). The origin of primary textures in granitic pegmatites. *Canadian Mineralogist* **47**, 697–724.

London, D. & Morgan, G. B., VI (2012). The pegmatite puzzle. *Elements* **8**, 263–268.

Lundstrom, C. C., Shaw, H. F., Ryerson, F. J., Williams, Q. & Gill, J. (1998). Crystal chemical control of clinopyroxene–melt partitioning in the Di–Ab–An system: implications for elemental fractionations in the depleted mantle. *Geochimica et Cosmochimica Acta* **62**, 2849–2862.

Manea, V. C., Manea, M., Kostoglodov, V. & Sewell, G. (2005). Thermal models, magma transport and velocity anomaly estimation beneath southern Kamchatka. In: Foulger, G. R., Natland, J. H. & Presnall, D. C. *et al.* (eds) *Plates, Plumes, and Paradigms. Geological Society of America, Special Papers* **388**, 517–536.

Maury, R. C., Defant, M. J. & Joron, J.-L. (1992). Metasomatism of the sub-arc mantle inferred from trace elements in Philippine xenoliths. *Nature* **360**, 661–663.

McDade, P., Blundy, J. D. & Wood, B. J. (2003). Trace element partitioning between mantle wedge peridotite and hydrous MgO-rich melt. *American Mineralogist* **88**, 1825–1831.

McDonough, W. F. & Sun, S.-s. (1995). The composition of the Earth. *Chemical Geology* **120**, 223–253.

McInnes, B. I. A., Gregoire, M., Binns, R. A., Herzig, P.M. & Hannington, M. D. (2001). Hydrous metasomatism of oceanic sub-arc mantle, Lihir, Papua New Guinea: petrology and geochemistry of fluid-metasomatised mantle wedge xenoliths. *Earth and Planetary Science Letters* **188**, 169–183.

McPherson, E., Thirlwall, M. F., Parkinson, I. J., Menzies, M. A., Bodinier, J. L., Woodland, A. & Bussod, G. (1996). Geochemistry of metasomatism adjacent to amphibole-bearing veins in the Lherz peridotite massif. *Chemical Geology* **134**, 135–157.

Merlet, C. (1994). An accurate computer correction program for quantitative electron probe microanalysis. *Mikrochimica Acta* **114–115**, 363–376.

Milholland, C. S. & Presnall, D. C. (1998). Liquidus phase relations in the $CaO–MgO–Al_2O_3–SiO_2$ system at 3·0 GPa: the aluminous pyroxene thermal divide and high-pressure fractionation of picritic and komatiitic magmas. *Journal of Petrology* **39**, 3–27.

Moyen, J.-F. (2009). High Sr/Y and La/Yb ratios: The meaning of the 'adakitic signature'. *Lithos* **112**, 556–574.

Mukasa, S. B., Blatter, D. L. & Andronikov, A. V. (2007). Mantle peridotite xenoliths in andesite lava at El Penon, central Mexican Volcanic Belt: Isotopic and trace element evidence for melting and metasomatism in the mantle wedge beneath an active arc. *Earth and Planetary Science Letters* **260**, 37.

Nakamura, E., Campbell, I. H. & Sun, S.-S. (1985). The influence of subduction processes on the geochemistry of Japanese alkaline basalts. *Nature* **316**, 55–58.

Nielson, J. E. & Wilshire, H. G. (1993). Magma transport and metasomatism in the mantle: A critical review of current geochemical models. *American Mineralogist* **78**, 1117–1134.

Parkinson, I. J. & Pearce, J. A. (1998). Peridotites from the Izu–Bonin–Mariana forearc (ODP Leg 125): evidence for mantle melting and melt–mantle interaction in a supra-subduction zone setting. *Journal of Petrology* **39**, 1577–1618.

Parkinson, I. J., Arculus, R. J. & Eggins, S. M. (2003). Peridotite xenoliths from Grenada, Lesser Antilles Island Arc. *Contributions to Mineralogy and Petrology* **146**, 241–262.

Parman, S. W. & Grove, T. L. (2004). Harzburgite melting with and without H_2O: Experimental data and predictive modeling. *Journal of Geophysical Research* **109**, B02201.

Peacock, S. M., Rushmer, T. & Thompson, A. B. (1994). Partial melting of subducting oceanic crust. *Earth and Planetary Science Letters* **121**, 227–244.

Peslier, A. H., Francis, D. & Ludden, J. (2002). The lithospheric mantle beneath continental margins: melting and melt–rock reaction in Canadian Cordillera xenoliths. *Journal of Petrology* **43**, 2013–2047.

Pilet, S., Ulmer, P. & Villiger, S. (2010). Liquid line of descent of a basanitic liquid at 1·5 GPa: constraints on the formation of metasomatic veins. *Contributions to Mineralogy and Petrology* **159**, 621–643.

Portnyagin, M., Hoernle, K., Plechov, P., Mironov, N. & Khubunaya, S. (2007). Constraints on mantle melting and composition and nature of slab components in volcanic arcs from volatiles (H_2O, S, Cl, F) and trace elements in melt inclusions from the Kamchatka Arc. *Earth and Planetary Science Letters* **255**, 53–69.

Prouteau, G., Scaillet, B., Pichavant, M. & Maury, R. (2001). Evidence for mantle metasomatism by hydrous silicic melts derived from subducted oceanic crust. *Nature* **410**, 197–200.

Rapp, R. P., Shimizu, N., Norman, M. D. & Applegate, G. S. (1999). Reaction between slab-derived melts and peridotite in the mantle wedge: experimental constraints at 3·8 GPa. *Chemical Geology* **160**, 335–356.

Ridolfi, F., Renzulli, A. & Puerini, M. (2010). Stability and chemical equilibrium of amphibole in calc-alkaline magmas: an overview, new thermobarometric formulations and applications to subduction-related volcanoes. *Contributions to Mineralogy and Petrology* **160**, 45–66.

Santos, J. F., Scharer, U., Gil Ibarguchi, J. I. & Girardeau, J. (2002). Genesis of pyroxenite-rich peridotite at Cabo Ortegal (NW Spain): geochemical and Pb–Sr–Nd isotope data. *Journal of Petrology* **43**, 17–43.

Schiano, P., Clocchiatti, R., Ottolini, L. & Busi, T. (2001). Transition of Mount Etna lavas from a mantle-plume to an island-arc magmatic source. *Nature* **412**, 900–904.

Sen, C. & Dunn, T. (1994). Experimental modal metasomatism of a spinel lherzolite and the production of amphibole-bearing peridotite. *Contributions to Mineralogy and Petrology* **119**, 422–432.

Soustelle, V., Tommasi, A., Demouchy, S. & Ionov, D.A. (2010). Deformation and fluid–rock interaction in the supra-subduction mantle: microstructures and water contents in peridotite xenoliths from the Avacha volcano, Kamchatka. *Journal of Petrology* **51**, 363–394.

Spandler, C. & O'Neill, H. St. C. (2010). Diffusion and partition coefficients of minor and trace elements in San Carlos olivine at 1300°C with some geochemical implications. *Contributions to Mineralogy and Petrology* **159**, 791–818.

Stalder, R. (2002). Synthesis of enstatite single crystals at high pressure. *European Journal of Mineralogy* **14**, 637–640.

Stalder, R., Foley, S. F., Brey, G. P. & Horn, I. (1998). Mineral–aqueous fluid partitioning of trace elements at 900–1200°C and 3·0–5·7 GPa: New experimental data for garnet, clinopyroxene, and rutile, and implications for mantle metasomatism. *Geochimica et Cosmochimica Acta* **62**, 1781–1801.

Takahashi, E. (1980). Thermal history of lherzolite xenoliths—I. Petrology of lherzolite xenoliths from the Ichinomegata crater, Oga Peninsula, northeast Japan. *Geochimica et Cosmochimica Acta* **44**, 1643–1658.

Takahashi, E. (1986). Genesis of calc-alkali andesite magma in a hydrous mantle–crust boundary: Petrology of lherzolite xenoliths from the Ichinomegata Crater, Oga Peninsula, northeast Japan, part II. *Journal of Volcanology and Geothermal Research* **29**, 355–395.

Tatsumi, Y., Furukawa, Y., Kogiso, T., Yamanaka, Y., Yokoyama, T. & Fedetov, S. A. (1994). A third volcanic chain in Kamchatka: thermal anomaly at transform/convergence plate boundary. *Geophysical Research Letters* **21**, 537–540.

Thompson, A. B., Aerts, M. & Hack, A. C. (2007). Liquid immiscibility in silicate melts and related systems. In: Liebscher, A. & Heinrich, C. A. (eds) *Fluid–Fluid Interactions. Mineralogical Society of America and Geochemical Society, Reviews in Mineralogy and Geochemistry* **65**, 99–127.

Tiepolo, M., Oberti, R., Zanetti, A., Vannucci, R. & Foley, S. F. (2007). Trace-element partitioning between amphibole and silicate melt. In: Hawthorne, F. C., Oberti, R., Della, Ventura, G. & Mottana, A. (eds) *Amphiboles: Crystal Chemistry, Occurrence and Health Issues. Mineralogical Society of America and Geochemical Society, Reviews in Mineralogy and Geochemistry* **67**, 417–452.

Ulmer, P. (2001). Partial melting in the mantle wedge—The role of H_2O on the genesis of mantle-derived 'arc-related' magmas. *Physics of the Earth and Planetary Interiors* **127**, 215–232.

Van Den Bleeken, G., Müntener, O. & Ulmer, P. (2010). Reaction processes between tholeiitic melt and residual peridotite in the uppermost mantle: an experimental study at 0·8 GPa. *Journal of Petrology* **151**, 153–183.

Varfalvy, V., Hebert, R. & Bedard, J. H. (1996). Interactions between melt and upper-mantle peridotites in the North Arm Mountain

massif, Bay of Islands ophiolite, Newfoundland, Canada: Implications for the genesis of boninitic and related magmas. *Chemical Geology* **129**, 71–90.

Vasseur, G., Vernières, J. & Bodinier, J.-L. (1991). Modeling of trace element transfer between mantle melt and heterogranular peridotite matrix. *Orogenic Lherzolites and Mantle Processes. Journal of Petrology Special Volume*, 41–54.

Vernières, J., Godard, M. & Bodinier, J.-L. (1997). A plate model for the simulation of trace element fractionation during partial melting and magma transport in the Earth's upper mantle. *Journal of Geophysical Research* **102**, 24771–24784.

Vidal, P., Dupuy, C., Maury, R. & Richard, M. (1989). Mantle metasomatism above subduction zones: Trace-element and radiogenic isotope characteristics of peridotite xenoliths from Batan Island (Philippines). *Geology* **17**, 1115–1118.

Wang, J., Hattori, K. & Stern, C. (2008). Metasomatic origin of garnet orthopyroxenites in the subcontinental lithospheric mantle underlying Pali Aike volcanic field, southern South America. *Mineralogy and Petrology* **94**, 243–258.

Wood, B. J. (1991). Oxygen barometry of spinel peridotites. In: Lindsley, D. H. (ed.) *Oxide Minerals. Mineralogical Society of America, Reviews in Mineralogy* **25**, 417–431.

Yogodzinski, G. M., Lees, J. M., Churikova, T. G., Dorendorf, F., Woerner, G. & Volynets, O.N. (2001). Geochemical evidence for the melting of subducting oceanic lithosphere at plate edges. *Nature* **409**, 500–504.